Electronic Supporting Information

Chemically interlocked bipolar membrane achieving stable water dissociation for high output ammonia electrosynthesis

Ziang Xu,[a] Yiwen Liao,[a] Maobin Pang,[a] Lei Wan,[a] Qin Xu,[a] Yihan Zhen[a] and Baoguo Wang*[a]

[a]The State Key Laboratory of Chemical Engineering, Department of Chemical Engineering, Tsinghua University, No. 30 Shuang-Qing Road, Hai-Dian District, Beijing 100084, P. R. China.

E-mail: bgwang@tsinghua.edu.cn

Contents

1. Materials and methods

2. Synthesis procedure (Scheme S1 to S6 and Figures S1 to S7)

3. Supporting characterization (Figures S8 to S46)

4. Supporting comparation data (Table S1 and S2)

5. Supporting discussions (Note 1 to 4, containing Scheme S7 and Figures S47 to S48 and Table S3 to S5)

6. Reference

Materials and methods

Materials. P-Terphenyl (98%), 1-Methyl-4-piperidone (98%), trifluoroacetic acid (98%), trifluoroacetic acid (99%) and 1,6-dibromohexane (99%), 4-vinylbenzyl chloride (98%，stabilized with TBC), dimethylamine (AR, 40 wt. % in H_2O), tetrabutylphosphonium bromide (98%), benzoin ethyl ether (97%) and sodium 4-vinylbenzenesulfonate (90%) were purchased from MERYER CO.(China) and used without further purification. Dichloromethane (99.9%, Extra Dry, with molecular sieves, Water≤50 ppm), N-(1-naphthyl) ethyldiamine dihydrochloride (99%), ethylenediamine dihydrochloride (99%), acrylonitrile (99%), divinylbenzene (80% mixture of isomers), p-(dimethylamino) benzaldehyde (99%), urea (99%), dimethyl sulfoxide (99%), iodomethane (99.5%) and dimethyl sulfoxide-d6 ((D,99.8%) TMS(0.03%)) for NMR were received from Energy CO. (China). Inorganic chemicals, including sodium sulfate (Na_2SO_4, anhydrous,99%), H_3PO_4 (85%), potassium iodide (99%) potassium hydroxide (KOH, 85%) and potassium carbonate (K_2CO_3, 99%) were obtained from Adamas-beta CO. (China). Neosepta BP1 (Tokuyama Co., Japan) was used as a high-performance representative of commercial bipolar membrane for comparison purposes. Deionized (DI) water (18.2 MΩ cm) were applied throughout all experiments in this research.

Preparation of CIBM and NIBM

The C-C covalently interlocked bipolar membrane (CIBM) was fabricated through two steps: Firstly, ionomer 60 mg of VBQ2PPT (synthesized as described in **Section 2**) was dissolved in 3 mL DMSO to form a homogeneous solution. After filtrated with 0.45 μm micro-filtration membrane, the anion exchange layer (AEL) solution was casted onto a 5×5 cm of clean glass. The AEL was fabricated via volatilization of the solvent at room temperature and heat source should be kept away during membrane formation to avoid the possible C=C double bonds crosslinking. During the process, a nitrogen flow is recommended to introduced in order to accelerate volatilization process, and an VBQ2PPT AEL in halide form can be obtained at the end. The catalytic layer was conducted by spraying SnO_2 dispersion on to the surface of AEL (0.04 mg cm^{-2}). Secondly, CIBM can be obtained via in-situ polymerization of cation exchange layer (CEL) monomers. A solution of pre-polymerization solution containing 0.5 g of tetrabutylphosphonium 4-vinylbenzenesulfonate, 0.36 g of acrylonitrile, 0.06 g of divinylbenzene and 0.04

g of benzoin ethyl ether was prepared and casted onto the surface of AEL. A glass plate with same size was cover to the solution with a 25 μm polyethylene spacer to control the CEL thickness. Excess of CEL solution was wiped and the sandwiched glass plate was carefully transferred to 254 nm UV-light. The polymerization process took four hours for fully curing of CEL and cooled to room temperature. After separating the glass plates and soaking in DI water, CIBM with interlocked interface can be obtained.

The non-interlocked bipolar membrane (NIBM) was fabricated through similar procedures, except for the QPPT (synthesized as described in **Section 2**) without seeded C=C sites were adopted as AEL instead of VBQ2PPT.

Preparation of monomer ion exchange layer

The monomer layer preparation of AEL (QPPT or VBQ2PPT) was similar to the casting method of AEL for bipolar membranes. After evaporating of solvents, the membrane was immersed into DI water and AEL can be individually peeled off. For ion exchange of the cation polymers into OH^- form, AEL was immersed in N_2 degassed 1 M KOH solutions at 60 °C for 24 hours, and this step was repeated for twice for thoroughly exchanging. Note that the whole process was completed in a glove bag charging with N_2 to avoid the influence of CO_2.

The preparation of CEL was directly conducted on a glass plate, keeping other polymerization conditions same as for bipolar membrane fabrication. For ion exchange of $C_4H_9P^+$ into H^+, CEL was immersed into 2 M H_2SO_4 solution at 100 °C for 48 hours. All the membrane layers should be repeatedly washed with DI water to move free ions before further testing.

Basic properties determination

Conductivity. In-plane conductivity measurements were conducted for CEL in H^+ and for AEL in OH^- form, which were prepared as described as before. Both AEL and CEL samples were cut into 1 cm × 4 cm and equipped into a four-electrode (Pt) cell for a.c. impedance tests. The cell was placed into a DI water bubbled with N_2 flow and the membrane samples were immersed. The impedance measurements were carried out at galvanostatic mode from 100 kHz – 1 Hz on PARSTAT 3000A potentiostat (AMETEK, USA) to obtain in-plane Ohmic resistance (R). Ionic conductivity (σ) can be obtained via following equation (1):

$$\sigma = \frac{L}{R \times T \times W}\#(1)$$

Where L, T, and W represents for length, thickness and width of the measured samples.

Swelling ratio & Water uptake. Measurements were applied for CEL in H^+ form and AEL in OH^- form cut into 1cm × 4cm, achieving by soaking in corresponding degassed acid and alkaline solution at 60 °C for 24h in order to change counter ions into H^+ or OH^- form. After thoroughly washed with DI water, both samples were drastically dried and the weight (W_{dry}) as well as length (L_{dry}) of sample in dried state were obtained. Then the samples were wiped into DI water till fully infiltrated from 30 °C to 80 °C with an interval of 10 °C. Weight (W_{wet}) and length (L_{wet}) in wet state of each temperature were recorded to calculate WU and SR of AEL and CEL by following equations (2-3):

$$WU(T)(\%) = \frac{W_{wet}(T) - W_{dry}}{W_{dry}} \times 100\%\#(2)$$

$$SR(T)(\%) = \frac{L_{wet}(T) - L_{dry}}{L_{dry}} \times 100\%\#(3)$$

Contact angle. Samples of original VBQ2PPT AEL or UV crosslinked were cut into ~2 cm × 2 cm and kept in vacuum to reach dry state before water contact angle measurement (Dataphysics OCAH200). A setting of 10 μL volume drop DI water was used at room temperature and the contact angel was recorded and fitted via Dataphysics software.

Mechanical and Thermal stability

Mechanical stability was measured using electronic universal material testing machine (HZ-1004B, Hengzhun, China). Samples of AEL and CEL (4 cm*4 cm) was further cut into spindle shape and kept in DI water reach wet state before tensile strength measurement.

Morphology and Chemical stability

Nuclear magnetic resonance (NMR). The ^{1}H NMR (liquid) spectrum were obtained from Bruker AVANCE III (US), and the detected chemicals were dissolved in $CDCl_3$, DMSO-d6 or D_2O, respectively.

Flourier transformed infrared spectroscopy (FTIR) and mapping. Completely dried AEM samples were detected using attenuated total reflection flourier transformed infrared spectroscopy (ATR-FTIR, Nicolet 6700FTIR) for chemical bonds and functional group information collection. Detections were conducted under room temperature and wave number range of 4000 cm^{-1}~600 cm^{-1} are covered.

FTIR-mapping of membrane surfaces were collected for dried samples fixed between two KBr optical plates at room temperature using Shimadzu AIM-9000. Surface scanning mode is selected for the experiments.

X-ray photoelectron spectroscopy (XPS). All-range survey, N 1s, C 1s, O 1s and S 2p (for CEL) information of dried samples were detected by XPS (Asylum MFP-3D-SA)

Field-emission scanning electron microscope (FE-SEM) analysis. The FE-SEM analysis was conducted for cross section of samples including CIBM and NIBM as well as surface morphology of anode/cathode catalysts using Merlin Compact (ZEISS, Germany). Among cross section samples, bipolar membranes were prepared by a scratch of lancet and membrane were snapped in liquid nitrogen. Energy dispersive spectroscopy detector accessory (EDS, X-max 80, OXFORD) was applied to analysis element distribution of cross section of membrane samples.

Computed micro-X-ray tomography (micro-CT, Zeiss Xradia Versa 520, Germany) analysis. Projection images of two dimension and three-dimensional interlayer structures of both CIBM and NICM were collected by micro-CT and reconstructed with a resolution of 0.5 μm per voxel.

Stripping strain measurements

Stripping strain has been measured to evaluate the adhesion strength of AEL and CEL using Universal Material Testing System (HZ-1004B, Hengzhun, China) at room temperature. Samples of bipolar membrane in wet state with size of 1 cm × 4 cm were prepared and strong sticky tape were put onto each side of the membrane layers (AEL and CEL), followed by clamped into upper and lower part of testing fixture and tested with a strain rate of 1 mm/min.

Electrochemical measurements for BMs

Four-electrode setup. As shown in Fig. S26, bipolar membranes were stuck in the middle of two symmetrical compartment with an effective area of 1 cm^2. Two Platinum electrodes placed outboard act as working electrode and counter electrode. Two reference electrodes were respectively placed inside Luggin capillary that contact the surface of bipolar membranes.

Electrochemical impedance spectroscopy. The EIS experiments were conducted with a self-made four-electrode cell equipped with CIBM, NIBM as well as Neosepta BP1. The cell was charged with 0.5 M Na_2SO_4 solution and should stand for 24 hours to reach steady state before EIS data collection. The data was obtained by PARSTAT 3000A potentiostat (AMETEK, USA) in galvanostatic mode with a frequency from 100 kHz to 0.1 Hz. An appropriate amplitude should be set to minimize the signal noise and keep data accuracy as well. The acquired Nyquist plot was fit by Z-view software based on equivalent circuit (Inset of Fig. 2g). Five parameters to describe ionic transportation and reaction kinetics at the interface of bipolar membrane, including ohmic resistance, ionic transportation, water dissociation constant, capacitance of depletion layer can be derived based on protonation-deprotonation mechanism according to previously reported[1, 2].

Determination of bipolar membrane water dissociation performance at low current density (0-100 mA cm^{-2}). Bipolar membranes were equipped in four-electrode cell with Luggin capillary design (Fig. S26). Membranes with 1 cm^2 effective area was let stood in cell for 24 hours before data recorded. Two platinum plate electrodes were connected to the working and counter electrodes and two Ag/AgCl electrodes in Luggin capillary were connected to sensor and reference electrodes. Current-voltage (I-V) curves were recorded as a performance indicator, which were obtained using PARSTAT 3000A potentiostat (AMETEK, USA) under galvanodynamic setup with a current range from 0-100 mA and a rate of current change of 2 mA/s and I-V relationships were collected. All tests were conducted in 0.5 M Na_2SO_4 at room temperature, and experiments were cut off when scanning to 100 mA or reaching upper limit of potentialstat applied voltage.

Determination of bipolar membrane water dissociation ability at high current density (0-1000 mA cm^{-2}). Same four-electrode cell as described were adopted to collect I-V data at a high current density, and pre-treatment are kept same as adopted in low current density experiments with 0.5 M Na_2SO_4. Here a programmable current plant SS-L605SPD (A-BF, China) was connected to working and counter electrode (Platinum) of the cell to avoid the applied voltage limitation, and two reference Ag/AgCl electrodes were connect to the potentialstat. The current plant was programmed to keep current across the bipolar membrane increasing by 2 mA/s from 0 mA to 1000 mA, and the transmembrane voltage drop were recorded by potentialstat at open current voltage mode. I-V curve of large current range can be obtained by simple transformation of recorded voltage versus time and linear relationship between current and time. During the experiments, the electrolytes in both the compartments were continuously refreshed with peristaltic pumps at a flow rate of 72 mL min^{-1} to minimize the concentration polarization effects.

pH-dependent water dissociation performance evaluation. The same equipment and similar procedures were adopted as above mentioned (Fig. S26) for I-V relationships obtaining. Electrolytes of different pH (0, 7, 14) were used in the study. Specifically, H_2SO_4 and KOH were adopted for preparing acidic and alkaline electrolytes, respectively.

Determination of bipolar membrane ionic balance maintaining ability. The ability of bipolar membranes to maintain the ionic balance of asymmetrical electrolytes (cathode 1M H^+/1M OH^- anode) of both sides was indicated by H^+ concentration variation of cathode side. Bipolar membranes were cramped in a H-cell to separate 100 mL of acid/base. Meanwhile, a constant 100 mA cm^{-2} was applied in a reverse bias mode during the study to mimic a practical situation, and the H^+ concentration was determined by titration method. Thus, the cathode H^+ concentration vs. time could be obtained when equipped with CIBM or NIBM.

Water dissociation stability assessments. Water dissociation stability of both CIBM and NICM were evaluated under a galvanostatic mode with same four electrode cell as described before. A current of 200 mA was kept to the cell by a current plant DP 3020 (MESTEK, China) through two platinum electrodes and transmembrane voltage drop versus time was recorded by a battery testing system CT3002A (LANHE, China) under pending mode. During stability tests, electrolytes of both sides were fully circulated and refreshed to minimize the effects of polarization.

Determination of bipolar membrane selectivity. Selectivity of CIBM, NIBM and commercial Neosepta BP1 were indicated by 1st limiting current density of water dissociation, which can be derived through first-order derivative of I-V relationship versus current, which the value of X when dependent variable (dV/dI) reaches its maximum value.

BM NH_3 electrosynthesis

Flow cell setup. A flow cell for NH_3 electrosynthesis was composed of endplates, current collectors, flow fields, gaskets, electrodes and bipolar membranes, with electrolytes circulation powered by a double channel peristaltic pump as shown in Fig. S28-S29. Commercial Co foam and the as prepared NiFe LDH foam were adopted to be cathode and anode electrodes. The effective working area for both anode and cathode electrodes are 1.0 cm^2, sandwiching a bipolar membrane a slightly larger to avoid electrolytes convection of both sides. The cell was assembled in sequence and then fastening by screws with a torque wrench at 5 N m. 2000 ppm KNO_3/1.0 M KOH solutions and 1.0 M KOH were flowed into cathode and anode respectively at a speed of 72 mL/min for 1 hour before testing. A certain current was applied by current plant DP 3020 and kept for 1min to reach steady state, and overall voltage applied to flow cell was collected.

Electrodes catalytic performance determination

Catalytic performance measurements of electrodes. NiFe LDH on Nickel foam was selected to act as anode electrode for oxygen evolution reaction (OER), which was prepared as our previously reported[3]. The catalytic performance was evaluated by three electrode methods, including a 1 cm^2 NiFe LDH working electrode, a graphite counter electrode and a Hg/HgO reference electrode. The testing was conducted in 1.0 M KOH electrolyte by linear sweep voltammetry method using PARSTAT 3000A potentiostat (AMETEK, USA) at a scan rate of 5 mV/s. All the potentials were converted into potential vs. RHE according to Nernst equation. EIS experiment for catalytic electrode was conducted under same condition by potentialstatic EIS mode with the frequency from 100 kHz to 1 mHz and fitted by Z-view software.

As our recently reported, Co nanoarray was elected to perform as high-performance cathode electrode for NO_3^- reduction reaction (NO_3^-RR). The 3D Nanoarray of Co was fabricated as a self-supported catalyst via electrodeposition strategy. The commercial Co foam was selected as the substrate, which is pre-cleaned by ultra-sonification in 6 M HCl for 10 minutes. The 1st step is to construct a Co 3D framework via a rapid H_2 template-electrodeposition method on the substrate, which is conducted using two-electrode setup in electrolytes containing 0.1 M $CoCl_2$ and 1 M NH_4Cl at 2 A cm^{-2} for 600 s. After rinse in DI water for several times, the 2nd step is to construct Co nanoarray on the framework. A three-electrode setup was used with electrolyte containing 0.05 M $Co(NO_3)_2$. The electrodeposition was firstly at -1.0 V vs. saturated calomel electrode (SCE) for 1200 seconds and then reduced in 1 M KOH at -1.4 V vs. Hg/HgO for 600s before washed with DI water.

The I-V curves of Co based catalysts for NO_3^-RR and hydrogen reduction reaction (HER) were conducted using PARSTAT 3000A potentiostat (AMETEK, USA) in 1M KOH alkaline electrolytes and the ones containing 2000 ppm. A 1 cm × 1 cm of self-supported catalysts was equipped to the working electrode of three-electrode measurement, and the Hg/HgO was selected as the reference electrode. The EIS measurements were conducted from 100 kHz to 1 mHz at -1 V vs. reference electrode. The faradaic efficiency and yield rate of main product NH_3 and side products NO_2^- or N_2H_4 were determined by colorimetric method as discussed below. The samples were taken from the electrolytes after constant potential electrolysis for 30 minutes.

Polarization curve. The polarization curve of bipolar membrane NH_3 synthesis flow cell system was tested at room temperature. When 50 mL of the electrolytes was flowed with peristaltic pumps and reached a steady state, the electrolytic current was set at 50 to 1000 mA cm^{-2} (50 to 650 mA cm^{-2} for CIBM) with the current plant to reach a steady state for around 30 seconds. Then, the applied voltage for maintaining each current was recorded and I-V curves for each BMs were acquired.

Faradaic efficiency, yield rate and energy consumption. Determination of NH_3 Faradaic efficiency, yield rate and energy consumption at different current density. The flow cell was working at galvanostatic mode using current plant DP 3020 for tens of minutes and the electrolyte samples at each current was collected for NH_3 detection. The total volume of both cathode and anode electrolyte circulated are 75 mL for experiments at every current density. The electrolytes at each side were refreshed between every individual testing. NH_3 Faradic efficiency, yield rate and energy consumption can be calculated based on the following equations (4-6):

$$\mathrm{NH_3\ Faradaic\ efficiency} = \frac{\left(8 \times F \times C_{NH_3} \times V\right)}{I \times t} \#(4)$$

$$\mathrm{NH_3\ Yield\ rate} = \frac{C_{NH_3} \times V \times 17}{t \times S} \#(5)$$

$$\mathrm{Energy\ consumption} = \frac{I \times U \times t}{C_{NH_3} \times V \times 17} \#(6)$$

Where F is the Faraday constant (96,485 C mo^{l-1}), C_{NH_3} is the measured NH_3 concentration, V is the volume of the cathodic electrolyte, I is the electrolysis current applied, t is the electrolysis duration, S is the effective surface area of electrodes and U is the corresponding applied voltage to the flow cell, which can be found in polarization curve.

Determination of Faradaic efficiency, yield rate at different current density of possible side products in catholyte: As discussed in **Note 3**, NO_2^- and N_2H_4 are main products accompanied with NO_3^-RR. The samples to be measured are taken the same way as mentioned above. Faradic efficiency, yield rate and energy consumption of NO_2^- and N_2N_4 can be calculated based on the following equations(7-10)：

$$\mathrm{NO_2}^{-} = \mathrm{Faradaic\ efficiency} = \frac{\left(F \times C_{NO_2^-} \times V\right)}{I \times t} \#(7)$$

$$\mathrm{KNO_2\ Yield\ rate} = \frac{C_{NO_2^-} \times V \times 85}{t \times S} \#(8)$$

$$N_2H_4 \text{ Faradaic efficiency} = \frac{\left(14 \times F \times C_{N_2H_4} \times V\right)}{I \times t} \#(9)$$

$$N_2H_4 \text{ Yield rate} = \frac{C_{N_2H_4} \times V \times 32}{t \times S} \#(10)$$

Where F is the Faraday constant (96,485 C mol^{-1}), $C_{NO_2^-}$ and $C_{N_2H_4}$ are the concentration of NO_2^- and N_2H_4, V is the volume of the cathodic electrolyte, I is the electrolysis current applied, t is the electrolysis duration, S is the effective surface area of electrodes.

Stability test

The stability of bipolar membrane NH_3 synthesis flow cell system was tested through an intermittent mode with both cathode and anode electrolytes renewed for every several hours (~12 hours for most cycles). Excess amount pf electrolytes was circulated in each step with circulating speed of 72 mL/min, and a small portion of cathodic electrolytes are taken as samples to be measured for figuring out Faradic efficiency, yield rate and energy consumption change of NH_3 and other side products versus operation time.

Products determination (NH_3, NO_2^-, N_2H_4)

The concentration of produced NH_3 was determined by spectrophotometrically method using indophenol blue method. The cathodic samples should be diluted to 10 (100-200 mA cm^{-2}) or 100 (300-1000 mA cm^{-2}) times before detection for their high concentrations. In a typical way, 2 ml of diluted samples were added with 2 ml of a 1 M NaOH solution that contained salicylic acid and sodium citrate, followed by instilled 1 ml of 0.05 M NaClO and 0.2 ml of 1 wt% $C_5FeN_6Na_2O$ (sodium nitroferric cyanide). After placed for 2 hours, the color of the mixed sample was detected under Ultraviolet-visible Spectrophotometer and from 500-800 nm and the concentration of NH_3 was determined using the absorbance at a wavelength of 652 nm according to the calibrated line obtained beforehand.

A typical Griess test was adopted for NO_2^- concentration determination[4]. To prepare Griess reagent, 4g of N-(1-naphthyl) ethyldiamine dihydrochloride, 0.2 g of ethylenediamine dihydrochloride and 5 mL of H_3PO_4 was dissolved in 25 ml of deionized water. 5 ml of catholyte samples were diluted to proper concentration and adjusted to neutral pH for colorimetric detection and 0.1 mL of prepared Griess reagent was added. After 30 min of shaking, 400-700 nm absorbance of samples were measured by UV spectroscopy and 540 nm was used for concentration determination according to calibration line.

The concentration of N_2H_4 was detected by Watt and Chrisp's method as reported[5]. P-(dimethylamino) benzaldehyde (4 g), HCl (concentrated, 30 ml) and ethanol (300 ml) were mixed to prepare chromogenic reagent and 0.1 mL was added into 5 mL diluted catholyte samples (adjusted to pH=3 with H_3PO_4) to be detected. 400-550 nm absorbance were collected and N_2H_4 concentration was calculated with absorbance at 460 nm according to calibration line.

Product collection and affirming.

The main product NH_3 was partly distilled from the cathodic electrolyte and absorbed in 1.0 M HCl aq. The solvent and excess of hydrochloric acid in absorption liquid were removed under vacuum to obtained NH_4Cl white powder. The crystal structure of product was affirmed by X-ray diffraction (XRD, Bruker D8 Advance).

Isotope labelling experiments.

We selectively conducted an isotope labelling experiments under NMR measurements to verify the reliability of obtained NH_3 Faradaic efficiency. Firstly, we conducted NH_3 electrosynthesis with same materials and conditions but replace the $^{14}N\text{-}KNO_3$ by 99% (atom) 15N-NO_3. 500 μL of electrolytes was taken out and neutralized to weak acid by 2 M HCl as sample and mixed with D_2O to achieve a total amount of 600 μL. The mixed electrolyte sample of ^{14}N and ^{15}N was qualitatively detected by ^1H NMR (Bruker, 400 MHz), and different peak splitting of H can be distinguished. Secondly, a $^{15}N\text{-}NH_4Cl$ calibration line was obtained for further determination of NH_3 Faradaic efficiency. We prepared several concentrations of $^{15}N\text{-}NH_4Cl$ solutions (~90% H_2O & 10% D_2O, adding 2 M HCl till weak acid) with precise amount of maleic acid as external standard. The samples were detected under NMR and the concentration of ^{15}N could be indicated by the peak area ration between $^{15}NH_4^+$ and external standard, so that a calibration line can be obtained. Thirdly, the NH_3 electrosynthesis at different current density (200, 400, 600, 800, 1000 mA cm^{-2}) were conducted with 2000 ppm $^{15}N\text{-}KNO_3$, and the NMR samples were prepared with same method. The concentration of NH_3 could be quantitatively determined according to the calibration line, and the Faradaic efficiency could be calculated and compared with the UV-Vis method.

Synthesis procedure (Scheme S1 to S6 and Figures S1 to S7)

Synthesis of quaternary ammonia poly (N-methyl-piperidine-co-p-terphenyl) QPPT

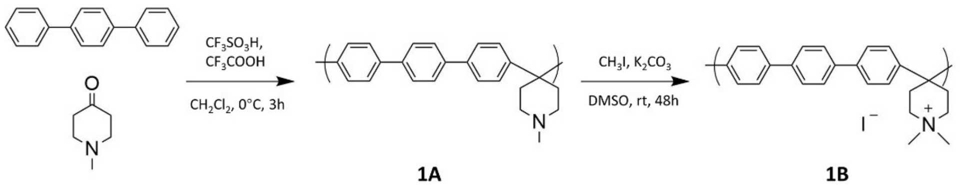

Scheme S1. Synthesis of quaternary ammonia poly (N-methyl-piperidine-co-p-terphenyl) (QPPT).

Poly (N-methyl-piperidine-co-p-terphenyl) (1A). The synthesis procedure was adapted from the previously works[6, 7]. 14.88 g of p-terphenyl, 8.3 mL of N-Methyl-4-piperidone and 24 mL of dichloromethane were charged into a 250 mL round-bottom flask and stirred in an ice bath (0 °C) for 5 minutes. Then 4.8 mL of trifluoroacetic acid was transferred into the bottle. The mixture was further cooled in 0 °C for 20 minutes, followed by adding with 60 mL of trifluoromethanesulfonic acid dropwise and the reaction was initiated kept in 0 °C. A mechanical agitation was adopted during reaction until becoming highly viscous after ~3 hours. The off-white fibriform solid was obtained by precipitating the viscous solution into DI water to quench the reaction and was washed repeatedly in DI water until neutral. After drying in 80 °C vacuum, polymer products **1A** of 21.50 g (93% yield) with high molecular weight can be obtained.

Quaternary ammonia poly (N-methyl-piperidine-co-p-terphenyl) (QPPT, 1B). 21 g of **1A** was dissolved in 420 mL dimethyl sulfoxide (DMSO) to form a 5 wt% solution in flask, and 10 g K_2CO_3 was added into the solution and stirred for 30 minutes. After that, 12 mL of CH_3I was added and the reaction mixture was kept in dark at room temperature for 48 hours. After filtered, the transparent and brown solution was dropped into 5 L ethyl acetate and yellow-white solid can be obtained via filtration. The obtained solid was washed with DI water to remove excess salts and final product **1B** QPPT in I^- form (1B) of 20 g (67 % yield) can be received after vacuum drying at 80 °C.

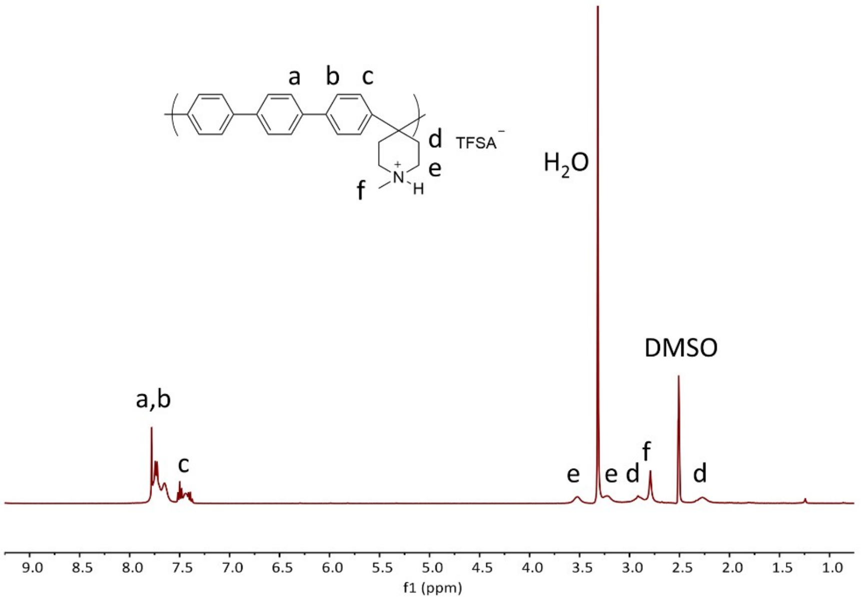

Fig. S1. ^{1}H NMR spectrum of poly (N-methyl-piperidine-co-p-terphenyl) (**1A**).

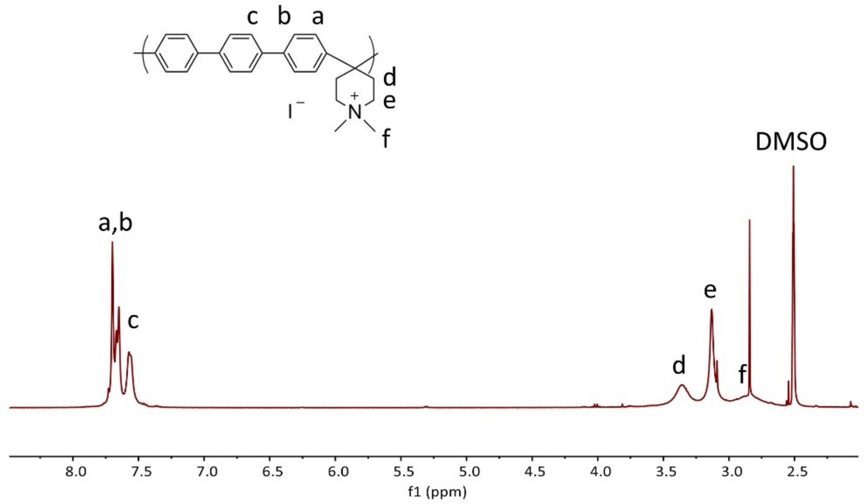

Fig. S2. ^{1}H NMR spectrum of quaternary ammonia poly (N-methyl-piperidine-co-p-terphenyl) (QPPT, **1B**).

Synthesis of (vinyl benzene quaternized hexane)-grafted poly (N-methyl-piperidine-co-p-terphenyl) (VBQ2PPT)

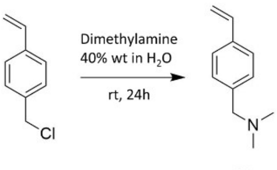

2A

Scheme S2. Synthesis of 4-N,N-Dimethyl- vinyl benzene.

4-N,N-Dimethyl- vinyl benzene (2A). The synthesis procedure was followed by previous work[8]. 9.3 g of 4-Vinylbenzyl chloride was added dropwise into a 30 mL of aqueous dimethylamine solution (40% wt) and the mixture was vigorous stirred at room temperature for 24 h. Them the product was extracted into chloroform (3 × 50 mL) washed with deionized water (3 × 50 mL) followed by drying with Na_2SO_4. The solvent was removed by evaporation, and the product **2A** (8.5 g, 87% yield) was obtained as a bright yellow liquid. 1H NMR (DMSO-d6, 400 MHz): δ 2.12 (s, 6H), 3.35 (s, 2H), 5.21-5.24 (d, 1H), 5.77-5.81 (d, 1H), 6.68-6.75 (q, 1H), 7.24-7.26 (d, 2H), 7.39-7.42 (d, 2H) ppm.

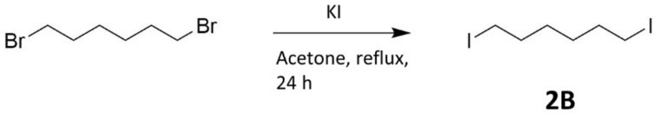

2B

Scheme S3. Synthesis of 1,6-diiodohexane.

1,6-diiodohexane (2B). The synthesis route was according to previous reported works[9]. 12.6 g of 1, 6-dibromohexane was dissolved into 500 mL acetone in round-bottom flask and 65.7 g of potassium iodide. The mixture was stirred and reflux for 24 hours, then the solvent was removed under reduced pressure. Next, The solid was resuspend in $CHCl_3$ and filtered to obtain the solution, followed by washing with DI water (3×100 mL). After drying with Na_2SO_4 and evaporation of solvent, the product **2B** (13.5 g, 77% yield) was obtained as a faint yellow liquid. 1H NMR (DMSO-d6, 400 MHz): δ 1.41-1.45 (m, 4H), 1.80-1.87 (m, 4H), 3.18-3.21 (t, 4H) ppm.

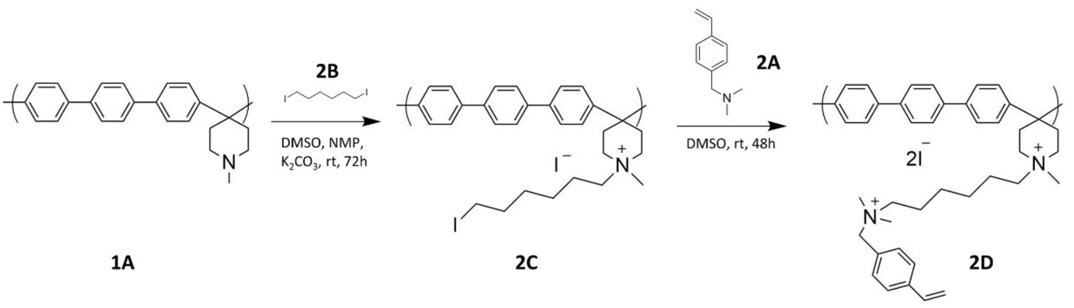

Scheme S4. Synthesis of (Vinyl benzene quaternized hexane)-grafted poly (N-methyl-piperidine-co-p-terphenyl) (VBQ2PPT).

1,6-diiodohexane -grafted poly (N-methyl-piperidine-co-p-terphenyl) (2C). 0.5 g of **1A** was dissolved into 15 mL of DMSO and 15 mL of N-Methylpyrrolidone (NMP) in flask and 7.5 mL of **2B** was poured into the solution under argon. After adequately stirred at room temperature for 30 minutes, 5 g of K_2CO_3 was added into the system and allowed to react under dark for 72 hours. Next, the solution was precipitated in 300 mL ethyl acetate and solid was obtained through centrifugation. The white solid product in I- form (0.45 g, 45% yield) was received after washing the solid with ethyl acetate and DI water for several times and dried in vacuum for 48 hours. A ~100% percent grafting of **2C** can be proved by 1H NMR.

(Vinyl benzene quaternized hexane)-grafted poly (N-methyl-piperidine-co-p-terphenyl) (VBQ2PPT, 2D). 0.3 g of **2C** was dissolved into 6 ml DMSO in flask under argon to form a 5% solution, and 0.3 g of **2A** was added into the solution to start the reaction. The reaction was stirred at room temperature for 48 hours under dark to achieve a complete quaternization. Finally, the solution was dropped into 100 mL of ethyl acetate to precipitate and obtain white solid by filtration. After washing by ethyl acetate and DI water for several times and dried in room temperature, the product (0.3 g, 81% yield) in I^- form was obtained.

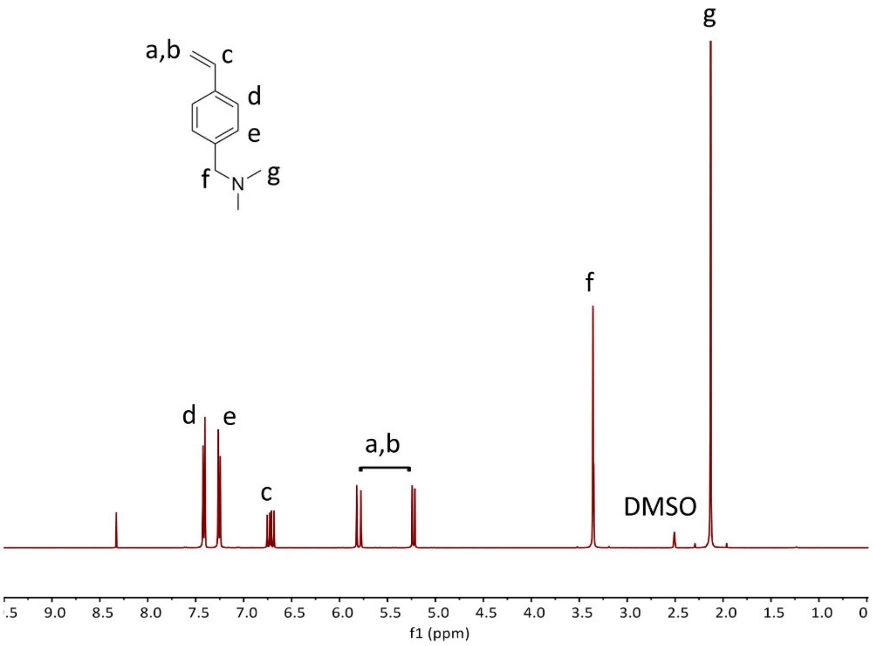

Fig. S3. ^{1}H NMR spectrum of 4-N,N-Dimethyl- vinyl benzene (**2A**).

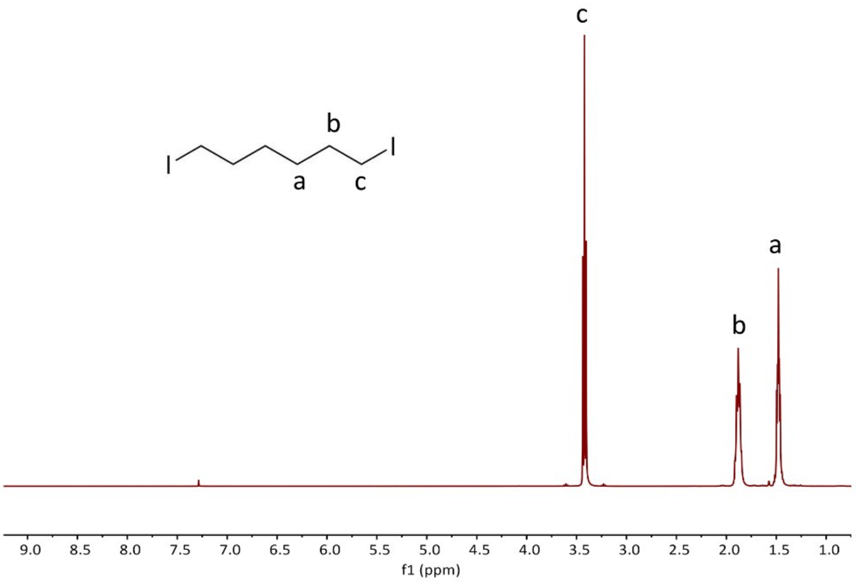

Fig. S4. ^{1}H NMR spectrum of 1,6-diiodohexane (**2B**).

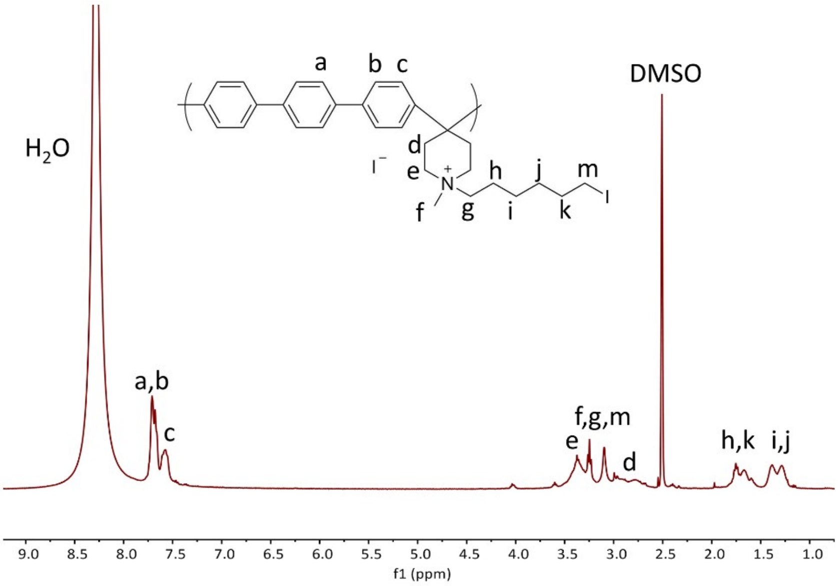

Fig. S5. ^{1}H NMR spectrum of 1,6-diiodohexane -grafted poly (N-methyl-piperidine-co-p-terphenyl) (**2C**).

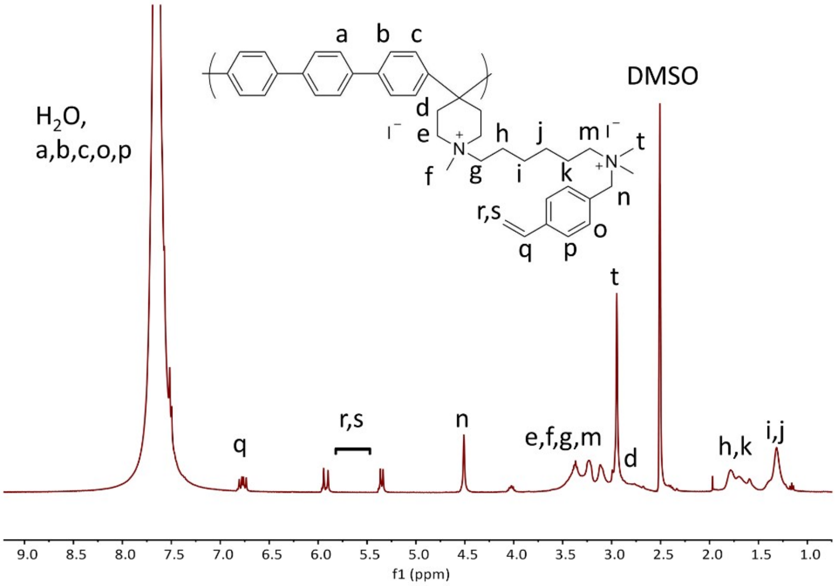

Fig. S6. ^{1}H NMR spectrum of (Vinyl benzene quaternized hexane)-grafted poly (N-methyl-piperidine-co-p-terphenyl) (VBQ2PPT, **2D**).

Synthesis of Poly (sulfonated-styrene-co-acrylonitrile) (PSSA)

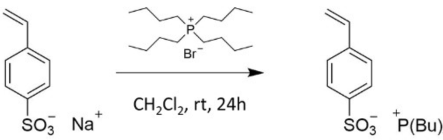

3A

Scheme S5. Synthesis of tetrabutylphosphonium styrene sulfonate.

Tetrabutylphosphonium styrene sulfonate (3A). An equimolar of Tetrabutylphosphonium bromide (10.17 g) and sodium styrene sulfonate (6.81 g) was dissolved in 20 mL of DI water and stirred for 24 hours at room temperature. Then the transparent solution was extracted with CH_2Cl_2 (2×20 mL) and washed with DI water (2×10 mL), followed by drying with Na_2SO_4. The solvent was evaporated under vacuum and the product **3A** was obtained as a colorless liquid (11.9 g, 85% yield). 1H NMR (DMSO-d6, 400 MHz): δ 0.88-0.91 (t, 12H), 1.33-1.49 (m, 16H), 2.14-2.22 (m, 8H), 5.24-5.27 (d, 1H), 5.80-5.85 (d, 1H), 6.69-6.76 (q, 1H), 7.41-7.43 (d, 2H), 7.58-7.60 (d, 2H) ppm.

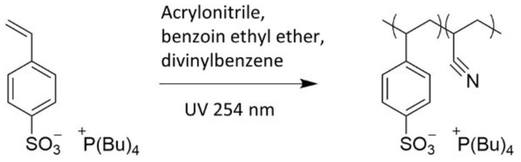

3B

Scheme S6. Synthesis of poly (sulfonated-styrene-co-acrylonitrile) (PSSA).

Poly (sulfonated-styrene-co-acrylonitrile) (PSSA, 3B). A solution of 0.5 g of **3A**, 0.36 g of acrylonitrile, 0.06 g of divinylbenzene and 0.04 g of benzoin ethyl ether was prepared. The polymerization was conducted under 254 nm UV for 4 hours and a transparent crosslinked anionic polymer film can be obtained in PBu4+ form. Ion exchange of Pbu4+ into H+ can be complete by soaking the film into 2 M H_2SO_4 at 80°C for 48 hours.

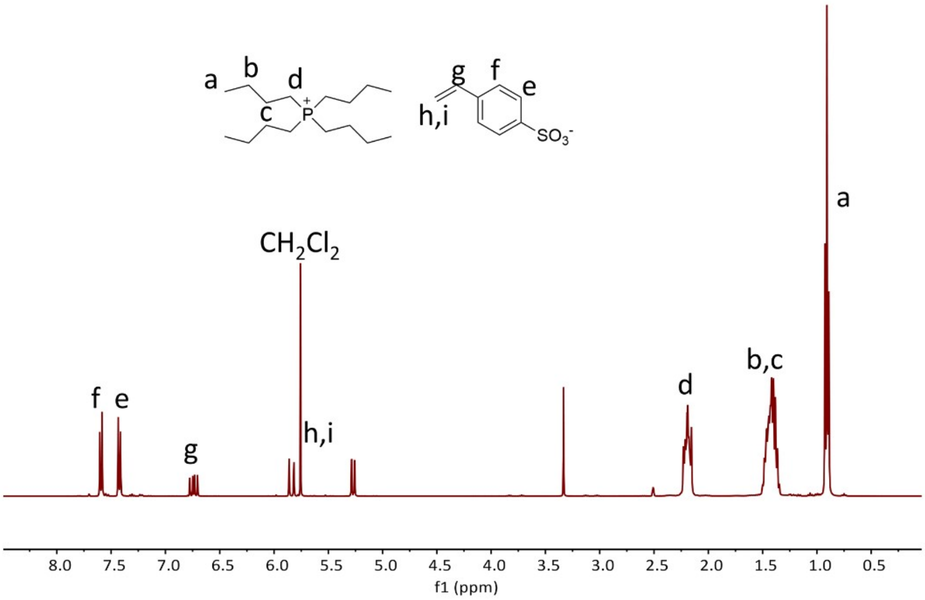

Fig. S7. ^{1}H NMR spectrum of tetrabutylphosphonium styrene sulfonate (**3A**).

Supporting characterization (Figures S8 to S46)

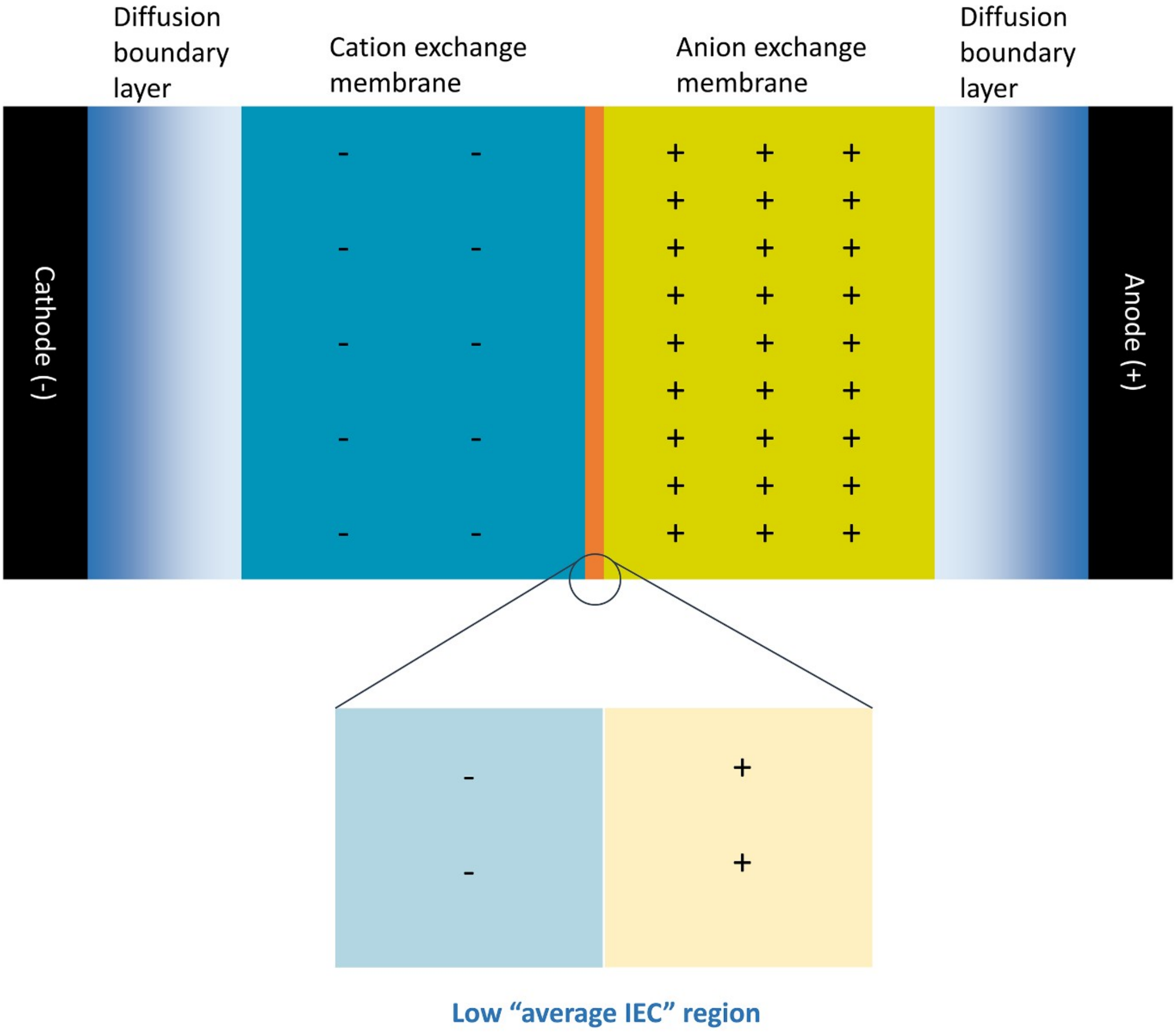

Fig. S8. Schematic illustration of one-dimensional bipolar membrane model for numerical simulation. Both the cation exchange layer and anion exchange layer are set to 50 μm with a 10 μm thickness of diffusion layer and a 0.1 μm of low “average IEC” region. The operating mode were set in reverse bias of bipolar membranes.

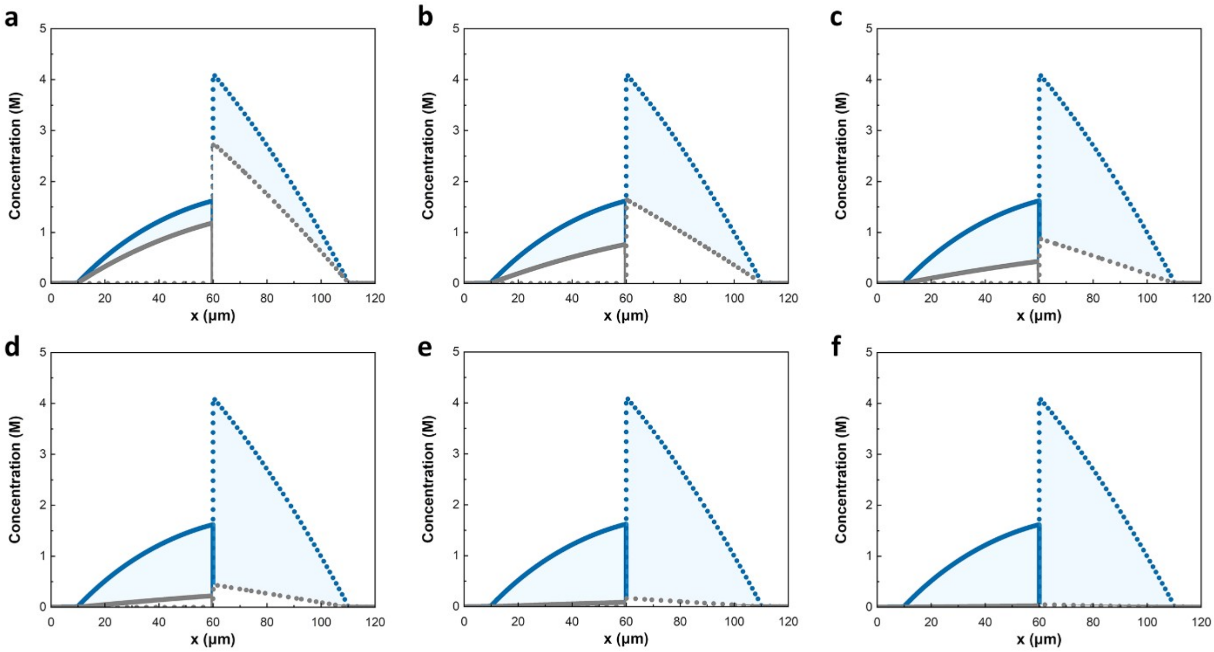

Fig. S9. All-range distribution of H$^+$ and OH$^-$ concentration of original bipolar membrane (marazine) and delaminated bipolar membrane with low "average IEC" region (gray line) based on numerical simulation under reverse bias of 1 V. The solid line and short dots represent for H$^+$ and OH$^-$, respectively. The ratio of IEC value between low "average IEC" region and main membrane are **a,** 0.875; **b,** 0.750; **c,** 0.625; **d,** 0.500; **e,** 0.375; **f,** 0.250.

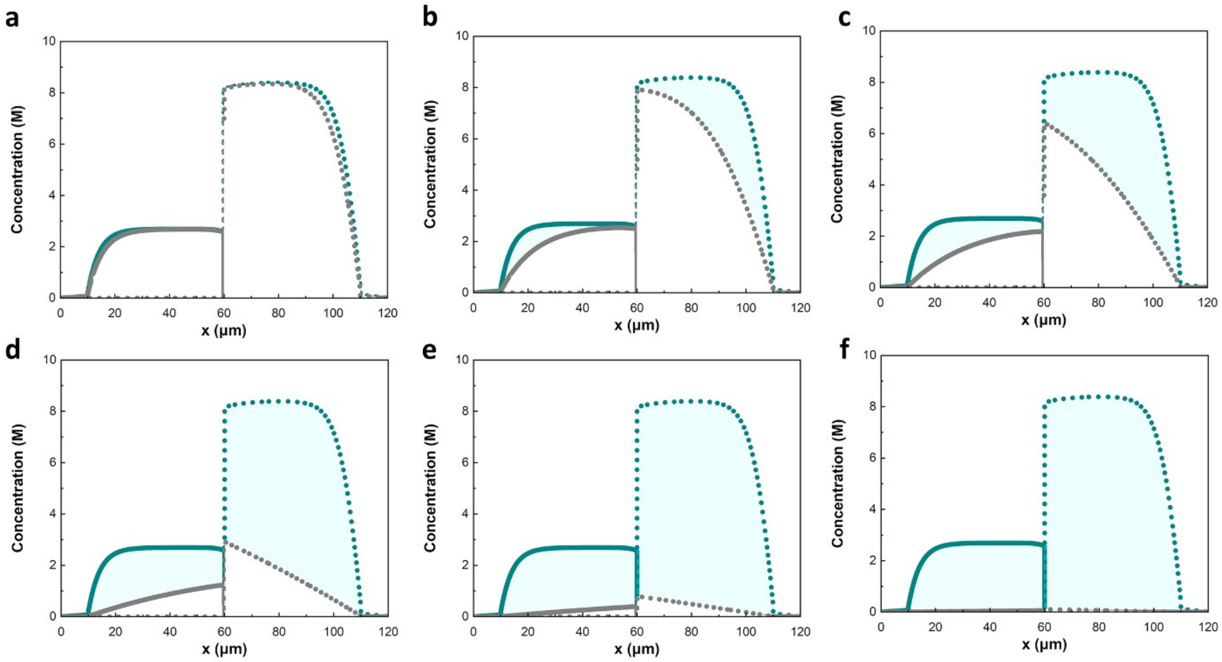

Fig. S10. All-range distribution of H$^+$ and OH$^-$ concentration of original bipolar membrane (emerald) and delaminated bipolar membrane with low “average IEC” region (gray line) based on numerical simulation under reverse bias of 2 V. The solid line and short dots represent for H$^+$ and OH$^-$, respectively. The ratio of IEC value between low “average IEC” region and main membrane are **a,** 0.875; **b,** 0.750; **c,** 0.625; **d,** 0.500; **e,** 0.375; **f,** 0.250.

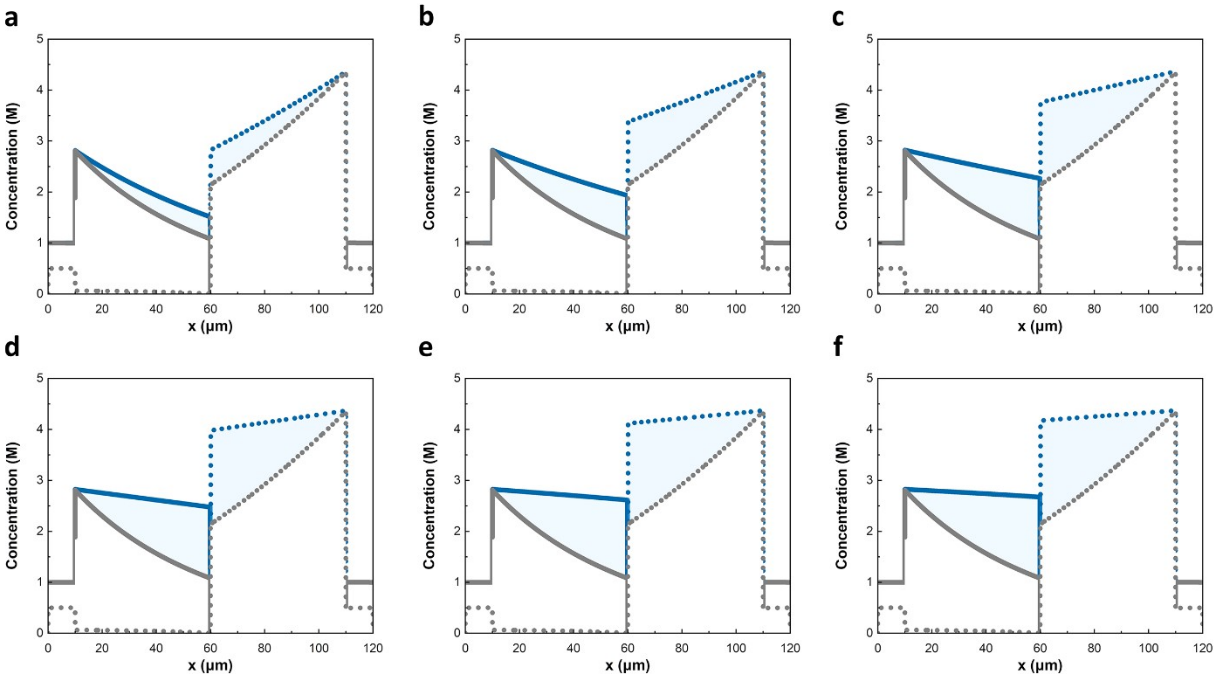

Fig. S11. All-range distribution of Na^+ and SO_4^{2-} concentration of original bipolar membrane (gray line) and delaminated bipolar membrane with low "average IEC" region (mazarine) based on numerical simulation under reverse bias of 1 V. The solid line and short dots represent for Na^+ and SO_4^{2-}, respectively. The ratio of IEC value between low "average IEC" region and main membrane are **a,** 0.875; **b,** 0.750; **c,** 0.625; **d,** 0.500; **e,** 0.375; **f,** 0.250.

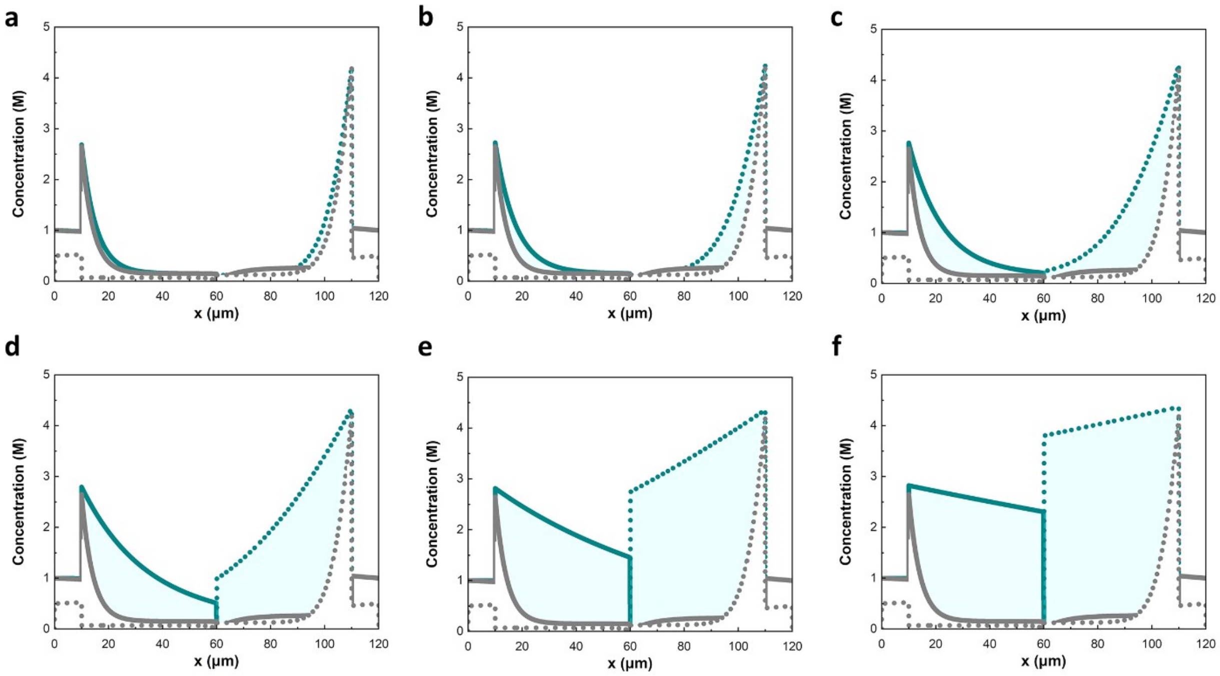

Fig. S12. All-range distribution of Na^+ and SO_4^{2-} concentration of original bipolar membrane (gray) and delaminated bipolar membrane with low “average IEC” region (emerald) based on numerical simulation under reverse bias of 2 V. The solid line and short dots represent for Na^+ and SO_4^{2-}, respectively. The ratio of IEC value between low “average IEC” region and main membrane are **a,** 0.875; **b,** 0.750; **c,** 0.625; **d,** 0.500; **e,** 0.375; **f,** 0.250.

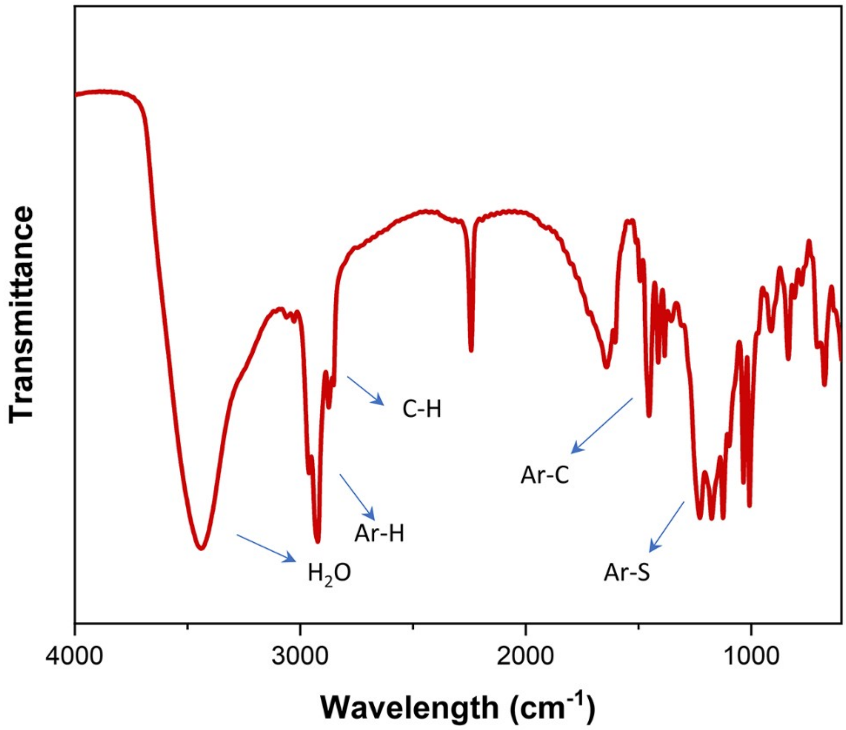

Fig. S13. FTIR spectrum of PSSA. Strong H_2O adsorption of the sample drying showed a hydrophilic nature of the polymer.

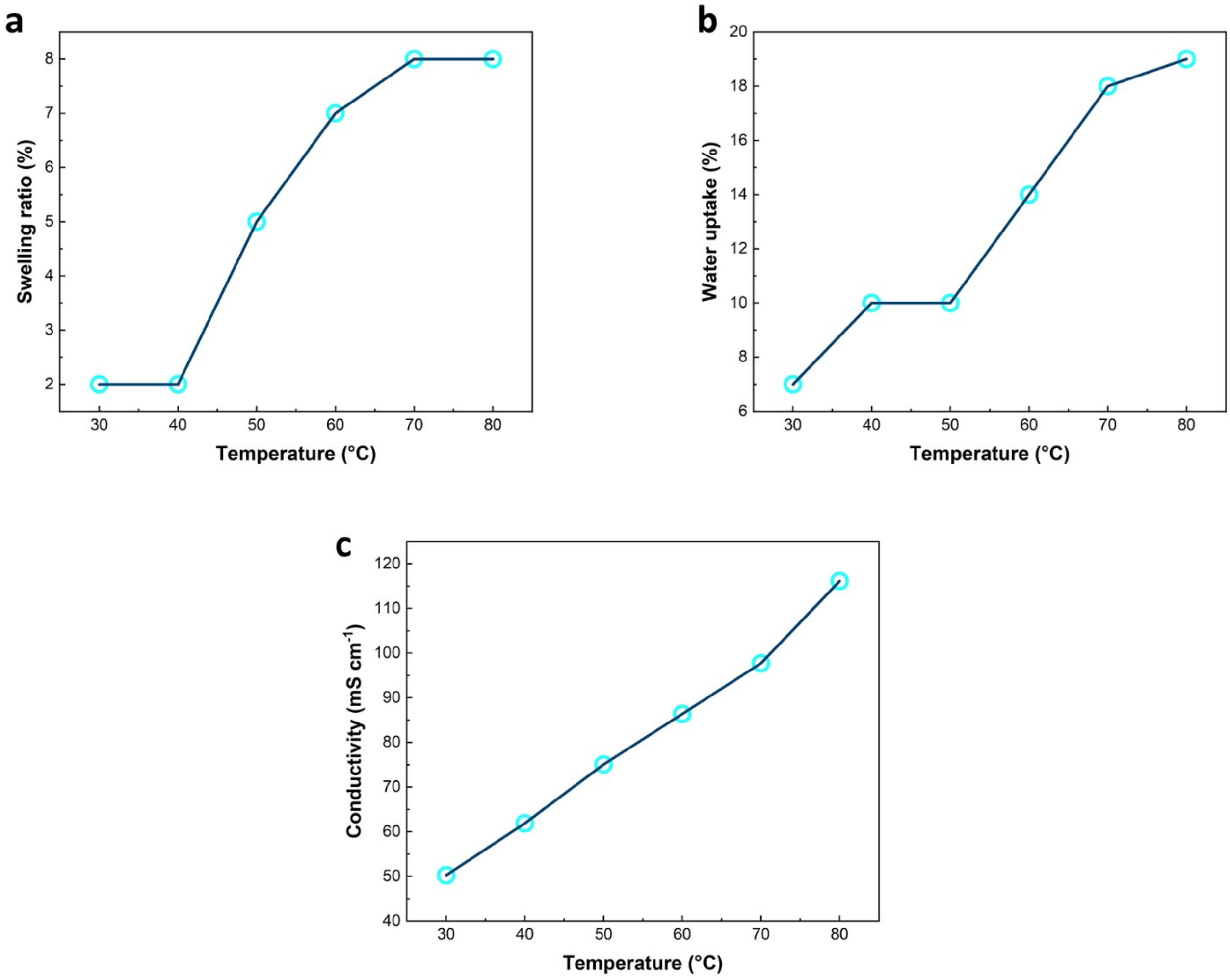

Fig. S14. Basic properties of PSSA as cation exchange layer vs. temperature. **a,** swelling ration (SR); **b,** water uptake (WU); **c,** proton conductivity.

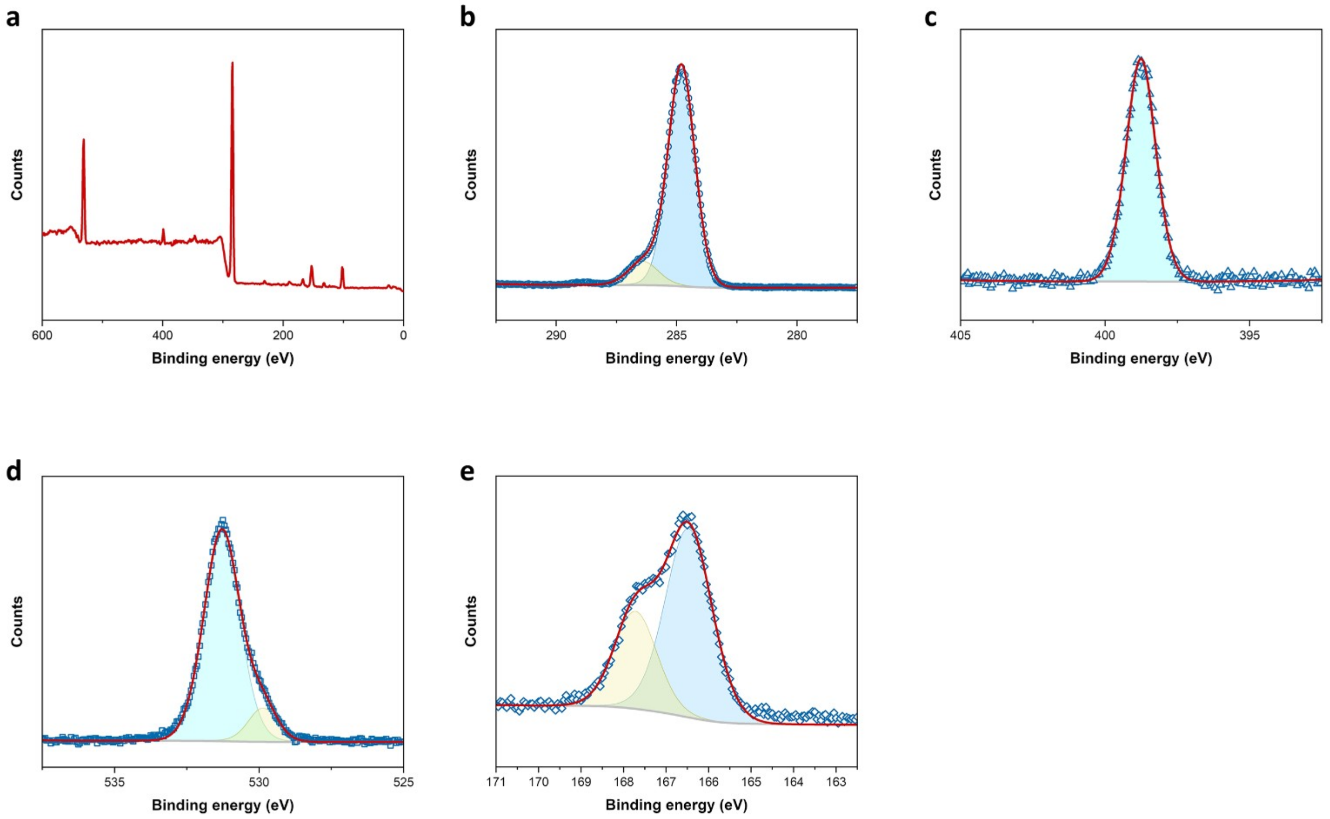

Fig. S15. XPS spectrum of PSSA. **a,** all-range survey; **b,** C 1s; **c,** N 1s; **d,** O 1s; **e,** S 2p.

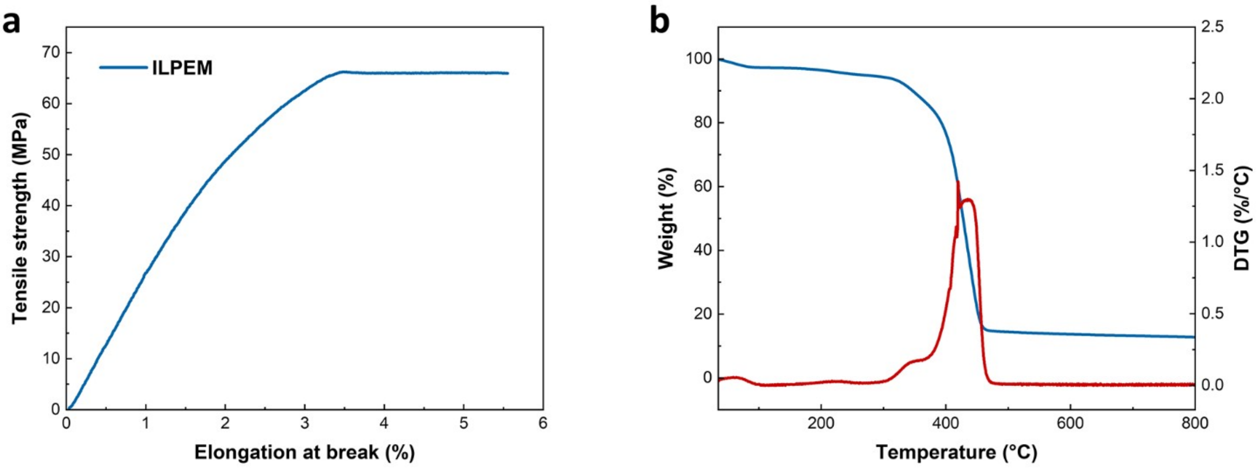

Fig. S16. a, Dimensional stability of PSSA membrane; **b,** TG and differential TG curves of PSSA membrane at nitrogen atmosphere and the heating rate of 10 °C min^{-1}.

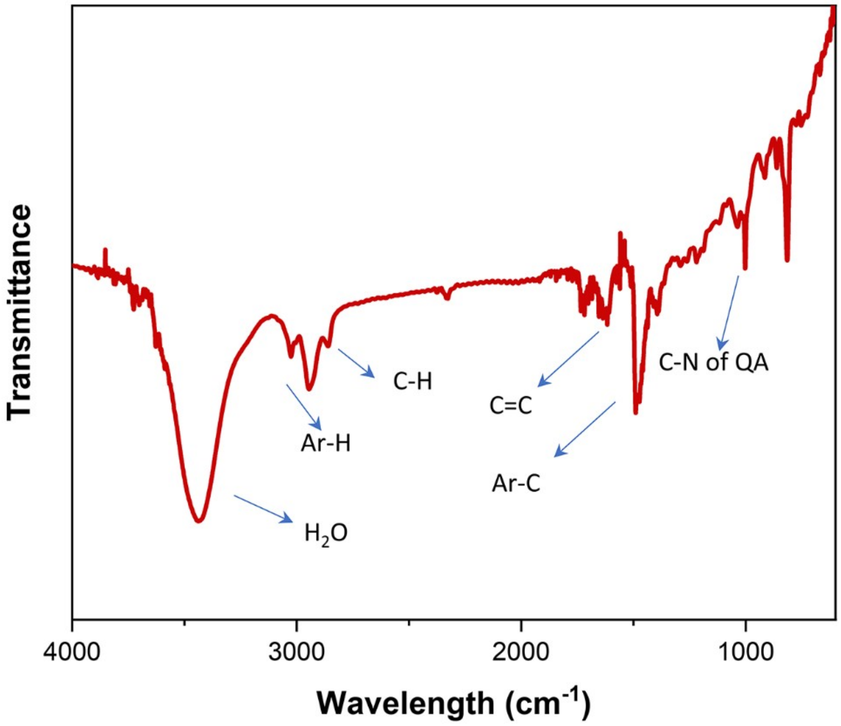

Fig. S17. FTIR spectrum of VBQ2PPT. Strong H_2O adsorption of the sample drying showed a hydrophilic nature of the polymer.

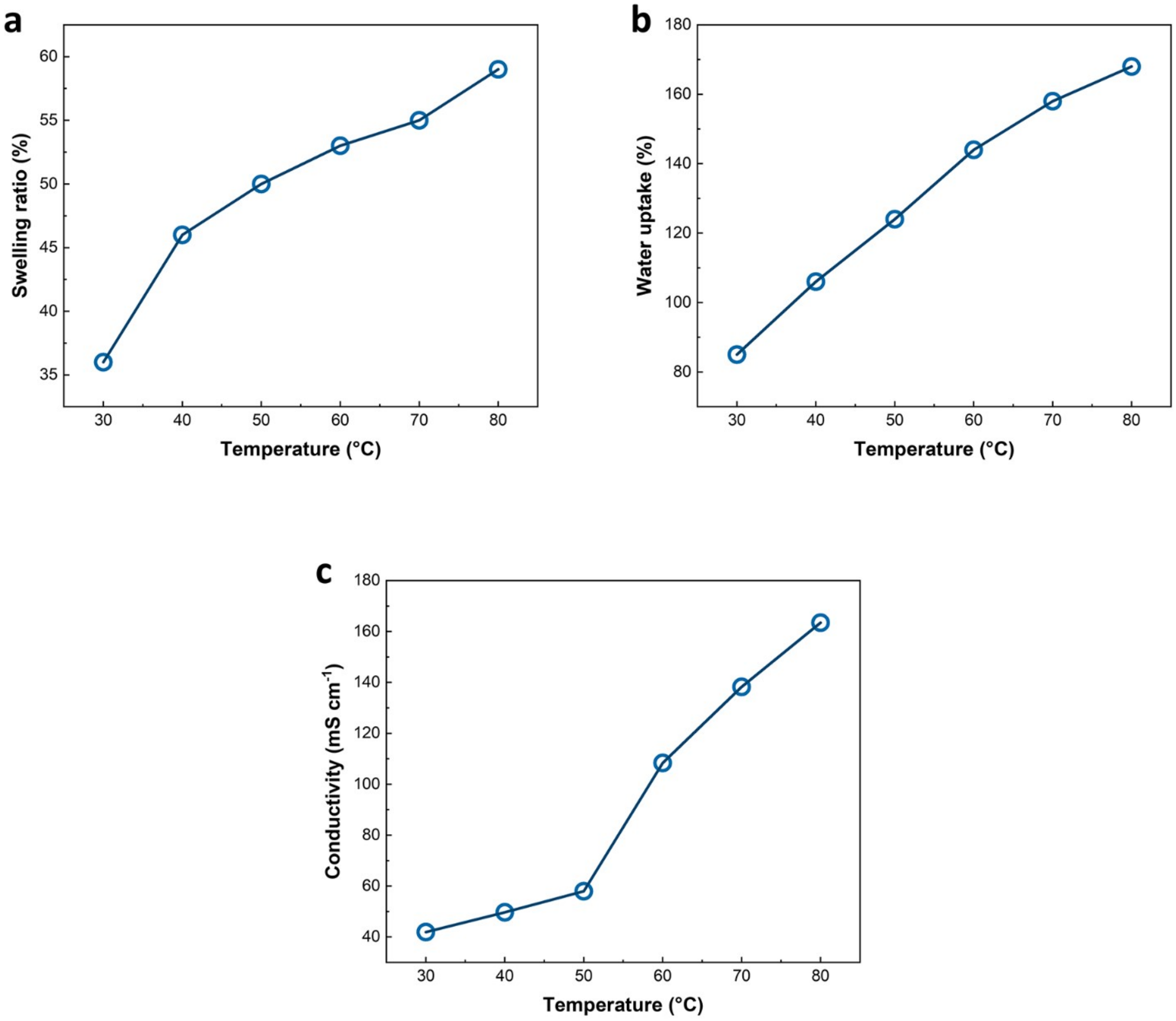

Fig. S18. Basic properties of VBQ2PPT as cation exchange layer vs. temperature. **a,** swelling ration (SR); **b,** water uptake (WU); **c,** hydroxide conductivity.

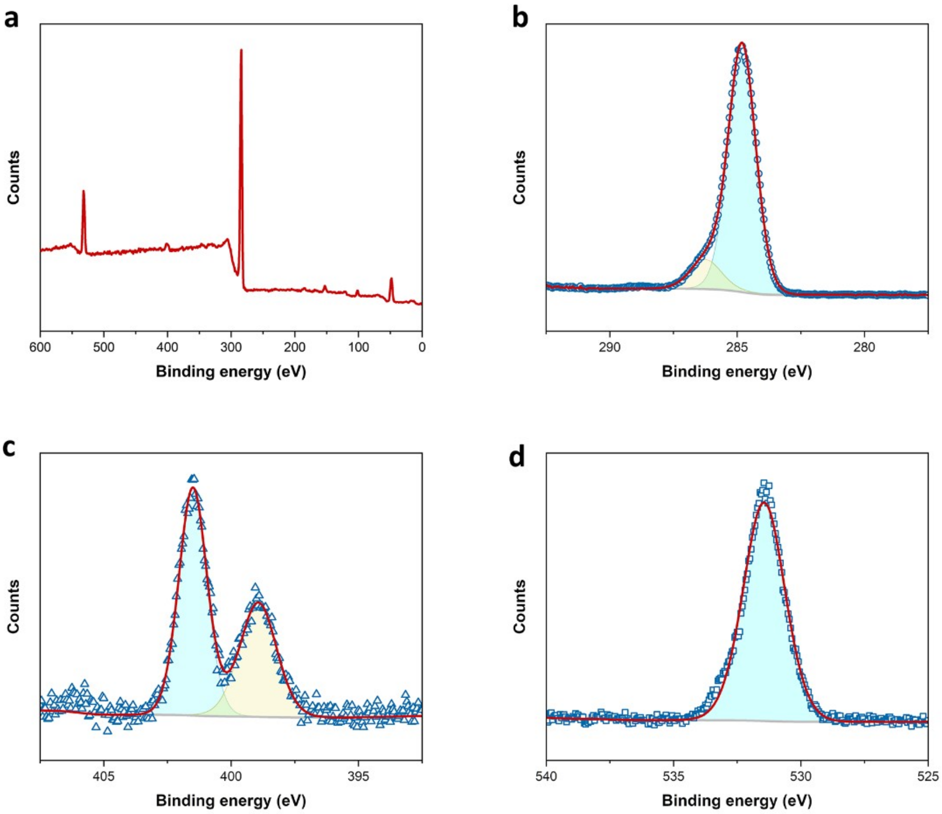

Fig. S19. XPS spectrum of UV-crosslinked VBQ2PPT. **a,** all-range survey; **b,** C 1s; **c,** N 1s; **d,** O 1s.

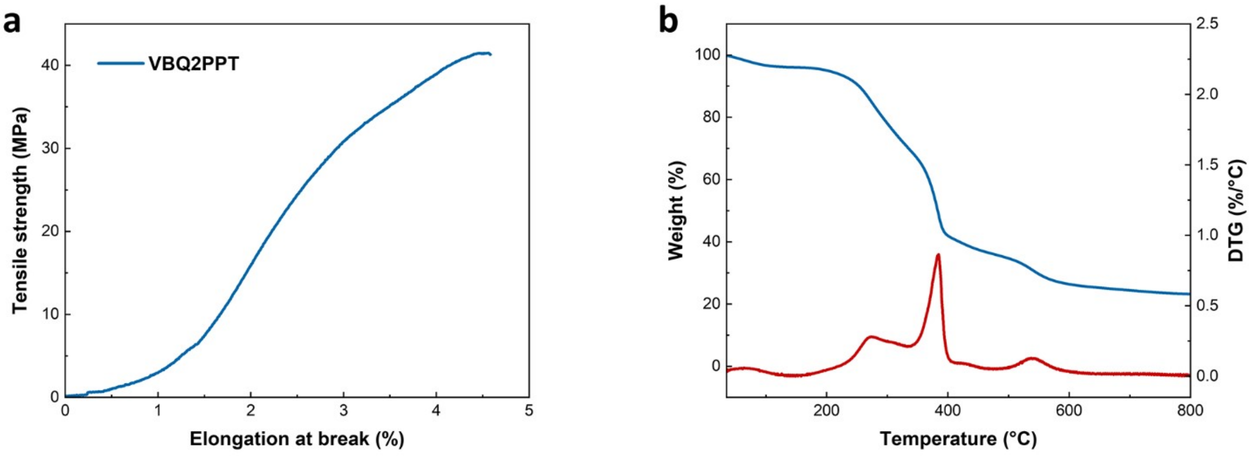

Fig. S20. a, Dimensional stability of VBQ2PPT membrane; **b,** TG and differential TG curves of VBQ2PPT membrane at nitrogen atmosphere and the heating rate of 10 °C min^{-1}.

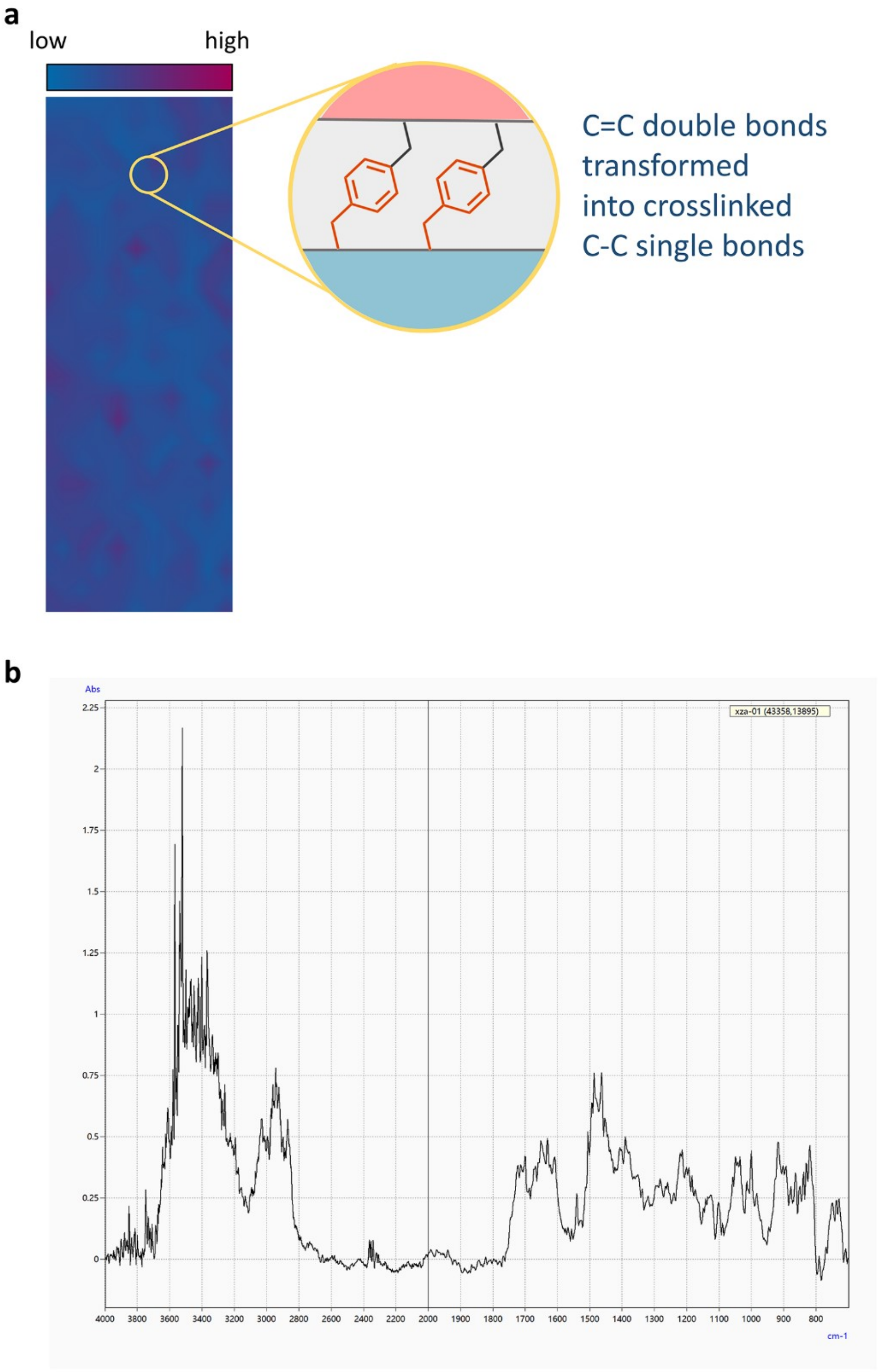

Fig. S21. a, FTIR-mapping of UV crosslinked VBQ2PPT. the color distribution reveals relative strength of C=C signals; **b,** local FTIR spectrum of UV crosslinked VBQ2PPT from 4000 to 600 cm^{-1}.

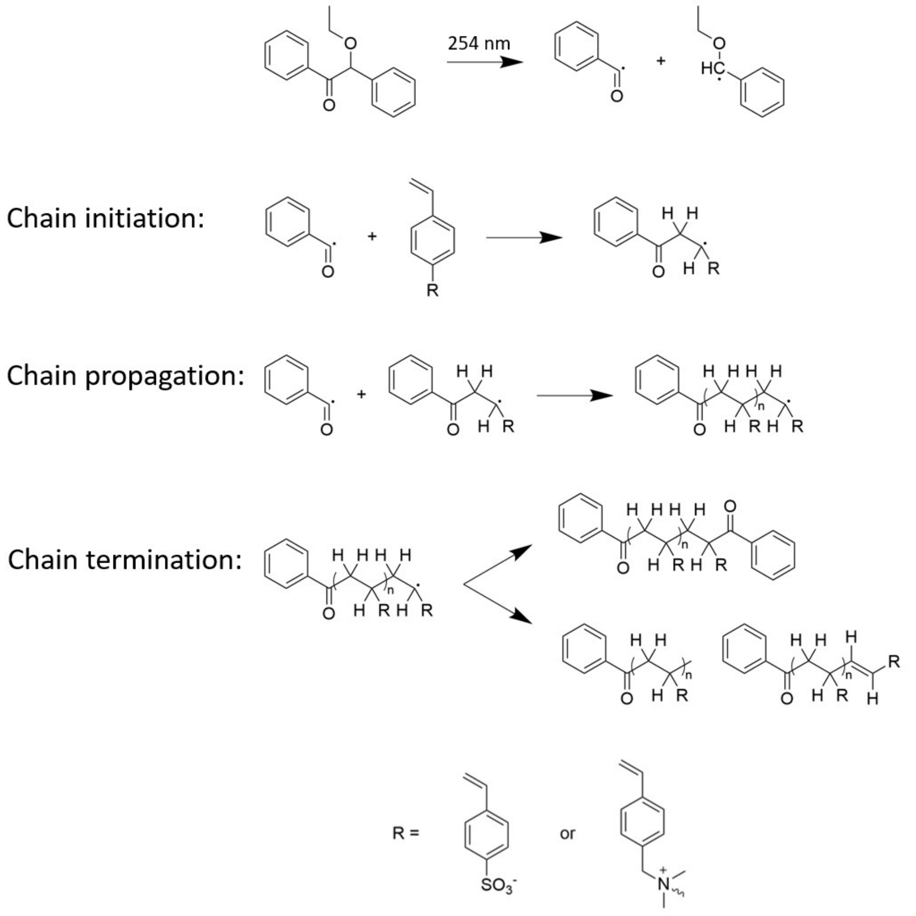

Fig. S22. Possible mechanism of CEL polymerization and chemical bond formation of AEL and CEL under 254 nm ultra-violet irradition and with benzoin ethyl ether as initiator.

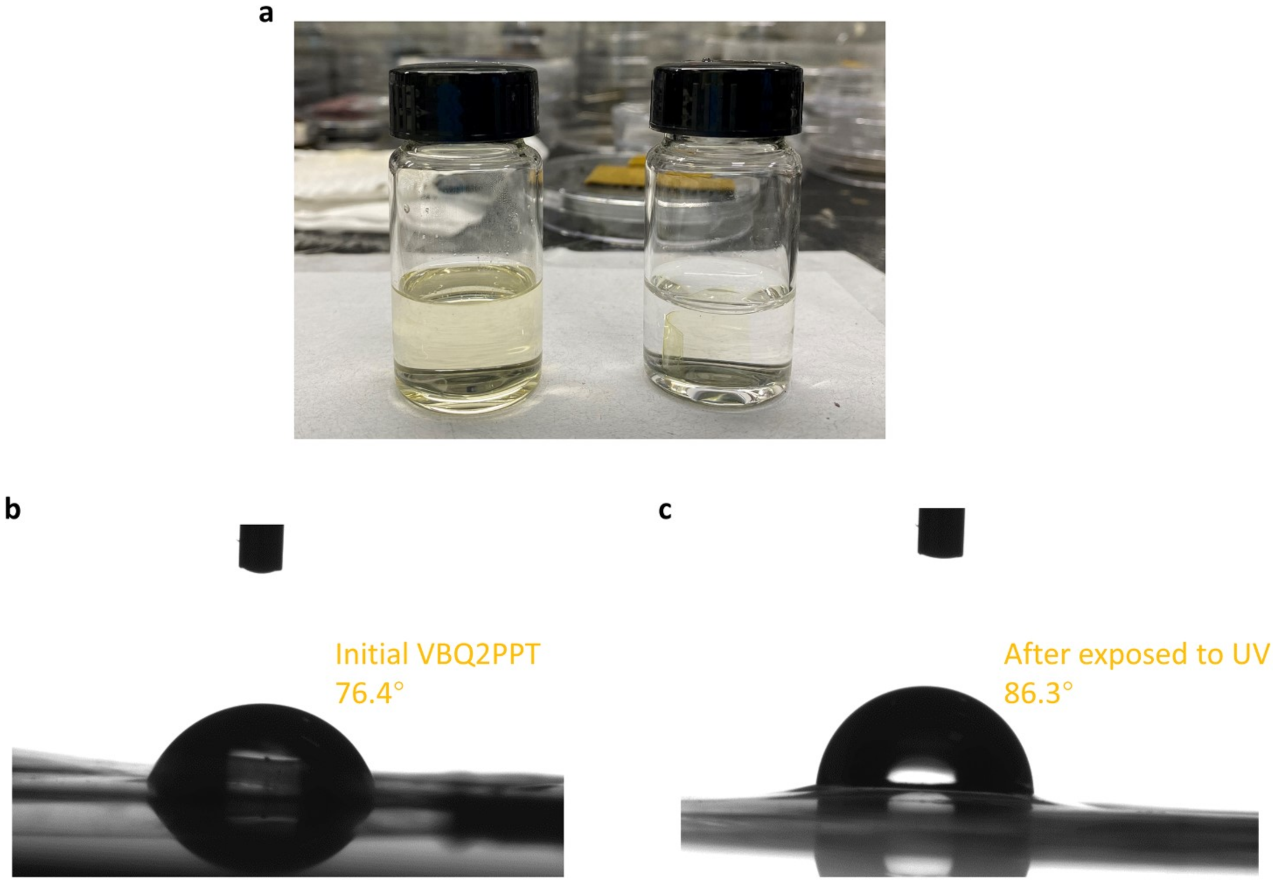

Fig. S23. a, the solubility test for VBQ2PPT in DMSO before (left) or after UV crosslinking for 1 hour. The water contacts angel for VBQ2PPT are presented in **b,** before and **c,** after UV treatment for 1 hour.

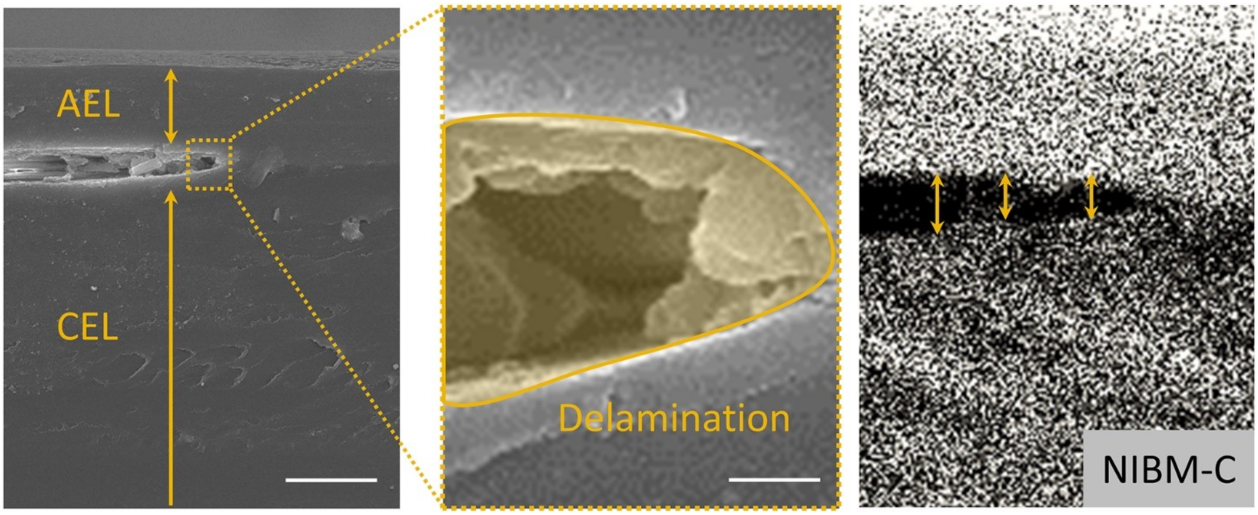

Fig. S24. The delaminated interface SEM image of NIBM after one cycle of drying-wetting. The scale bars are 30 μm (left) and 1 μm (right), respectively.

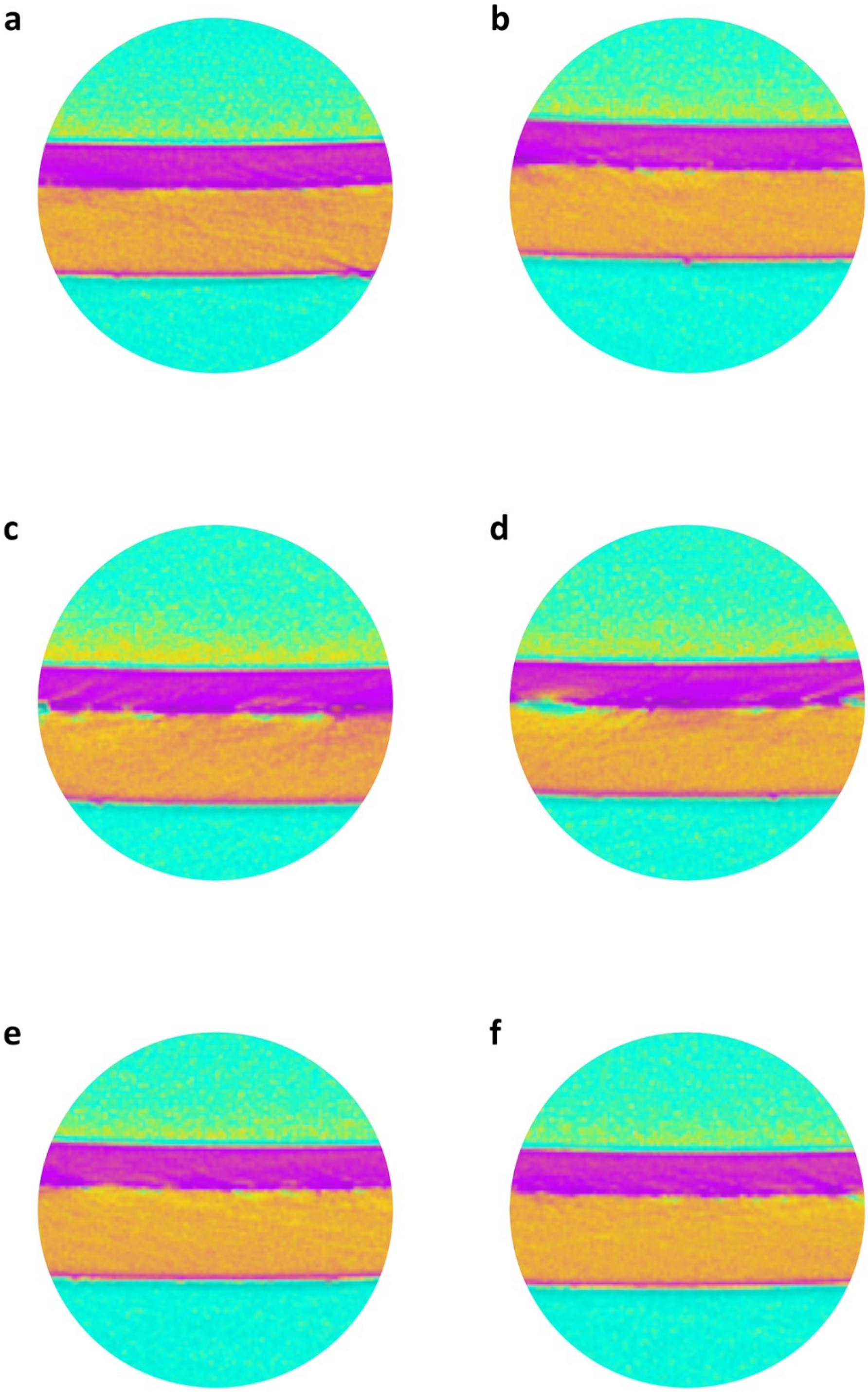

Fig. S25. Snapshots of 3D reconstruction projection of CIBM at various depth. **a,** 0 μm; **b,** 2 μm; **c,** 4 μm; **d,** 6 μm; **e,** 8 μm; **f,** 10 μm.

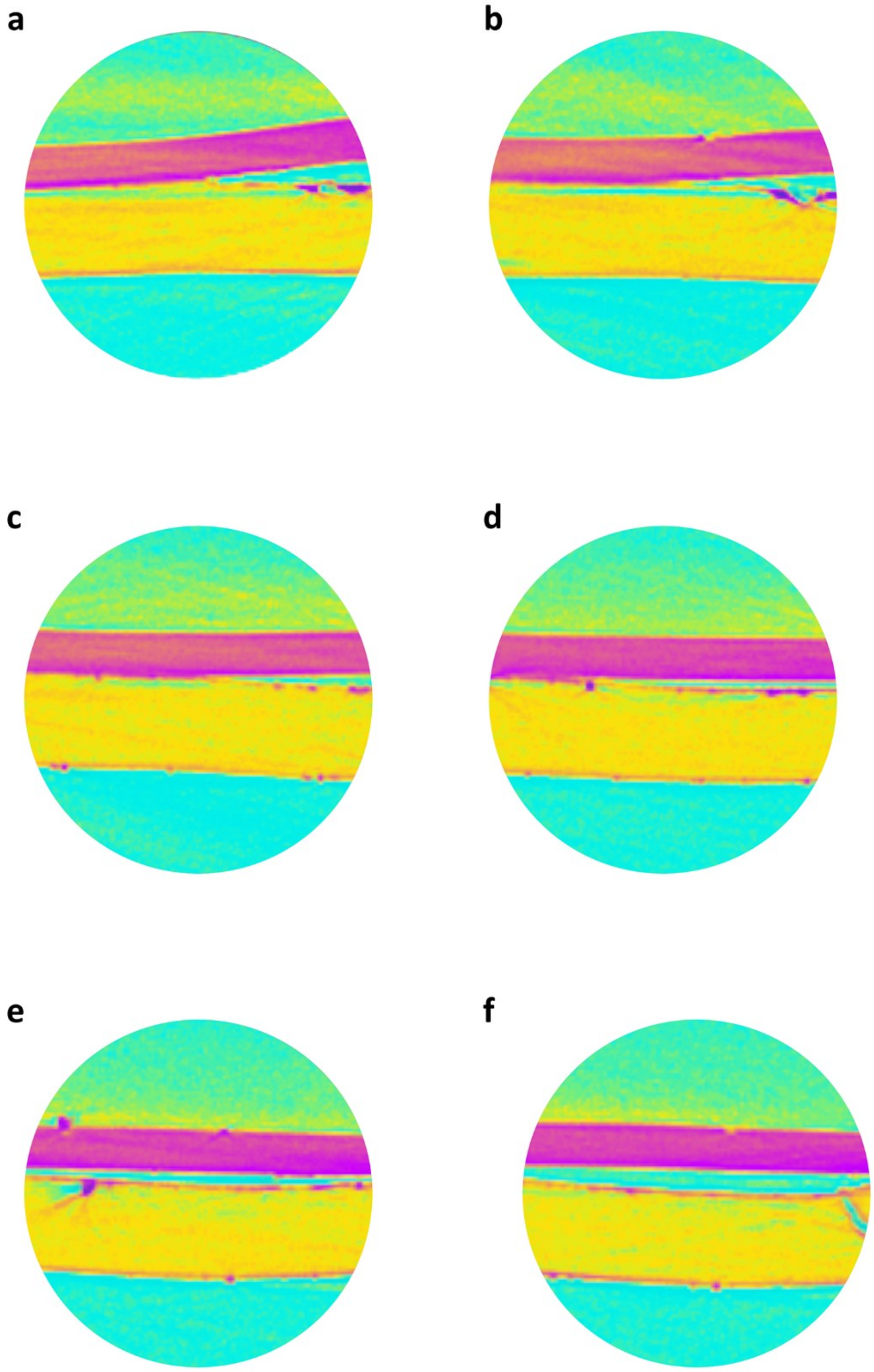

Fig. S26. Snapshots of 3D reconstruction projection of NIBM at various depth. **a,** 0 µm; **b,** 2 µm; **c,** 4 µm; **d,** 6 µm; **e,** 8 µm; **f,** 10 µm.

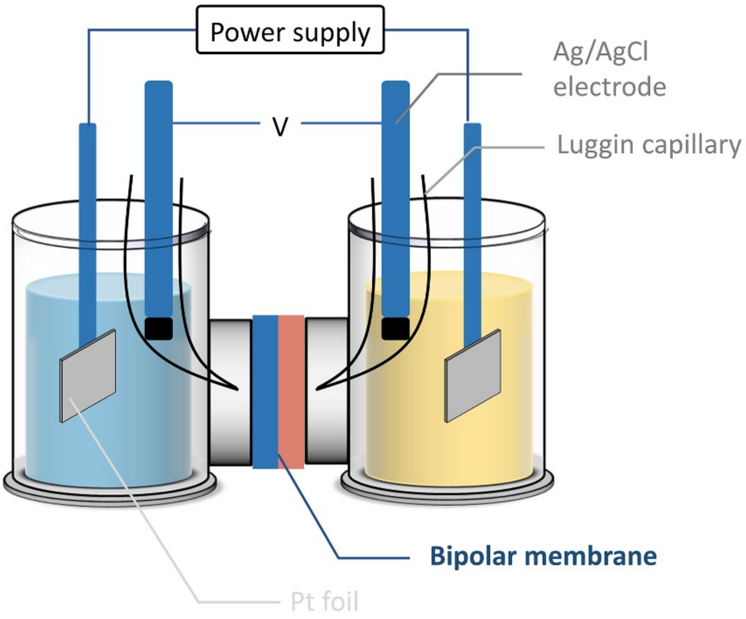

Fig. S27. Schematic illustration of four-electrode measurements setup for I-V relationship, long-term WD stability and EIS measurements

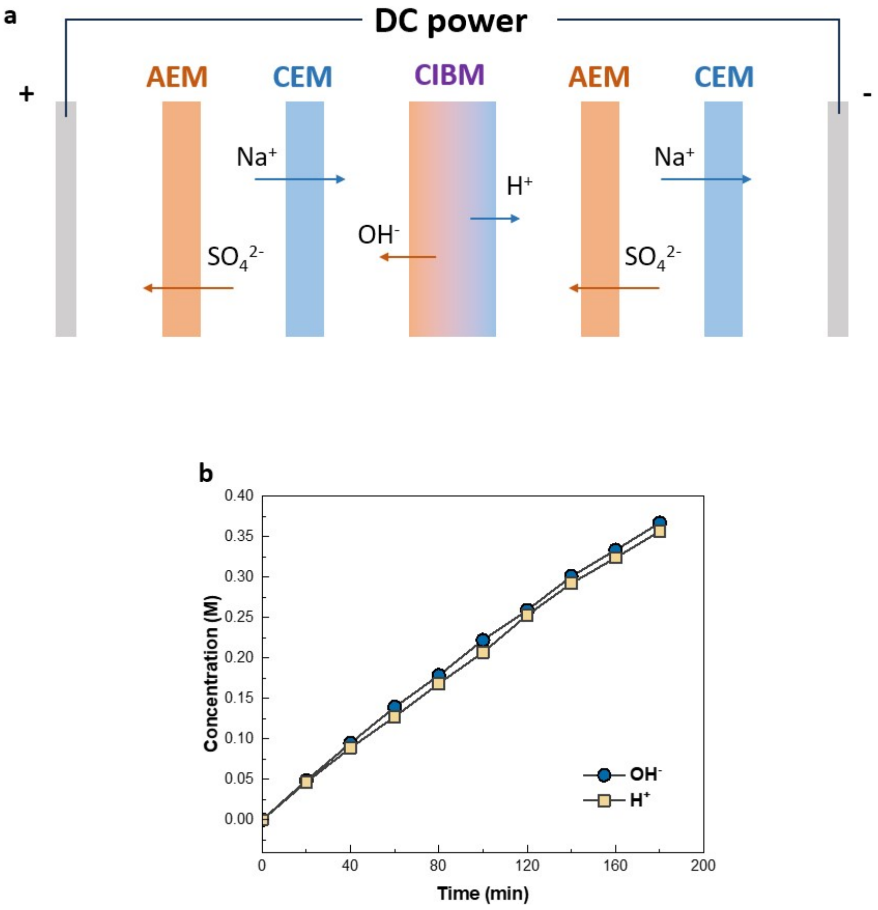

Fig. S28. a, The arrangement of BPM electrodialysis cell equipped with CIBM. The single layer AEM and CEM used in the experiment are piperION series and Nafion series, respectively. The active area of the setup is 1 cm^2. **b,** The concentrations of generated H_+ and OH_- from water splitting by CIBM interlayer.

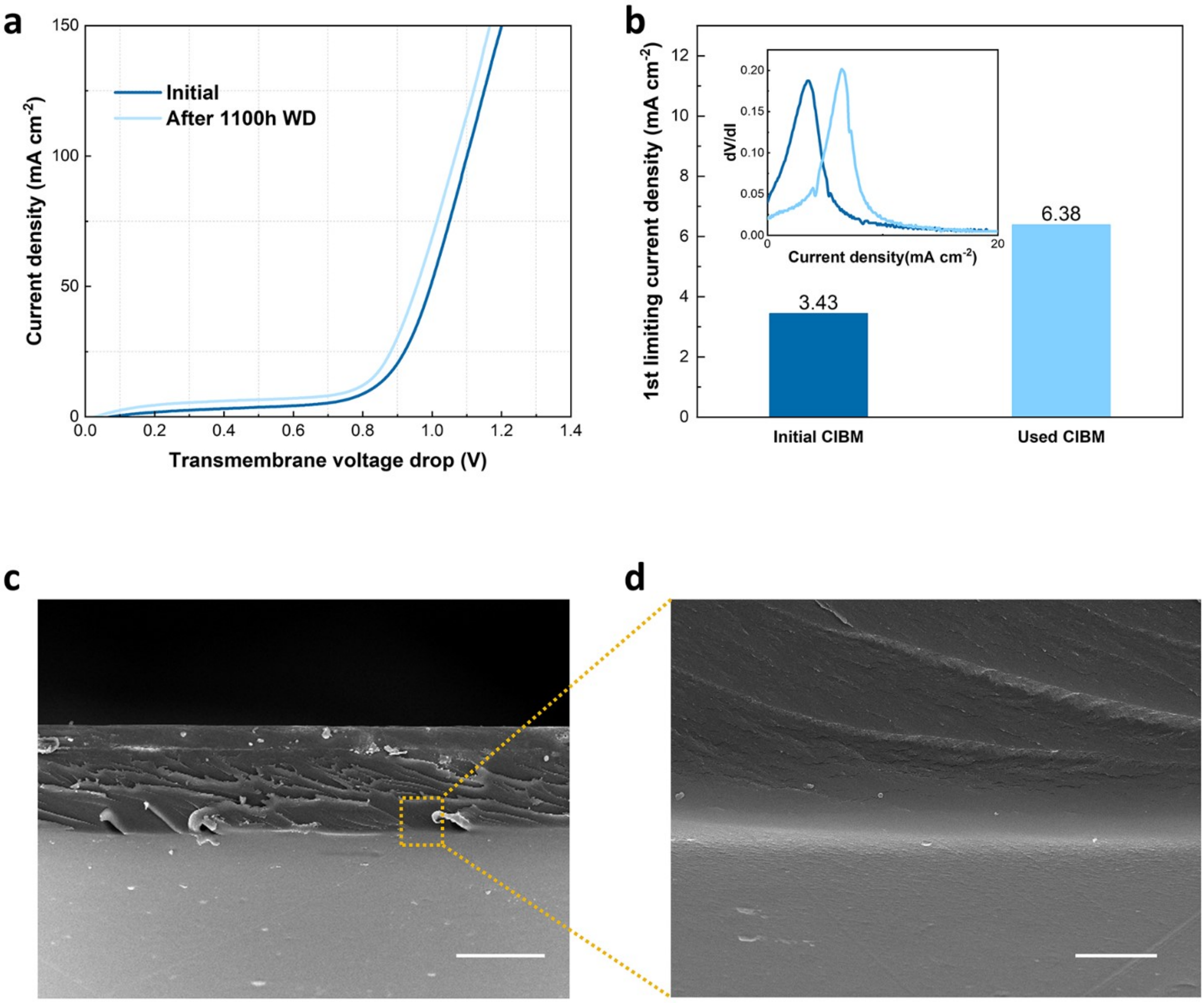

Fig. S29. Re-characterization of CIBM after stability test. **a,** IV curve before and after test; **b,** 1st limiting current density before and after test; **c, d,** interfacial structure of CIBM before and after test. The scale bars for **c,** and **d,** are 30 μm and 3 μm, respectively.

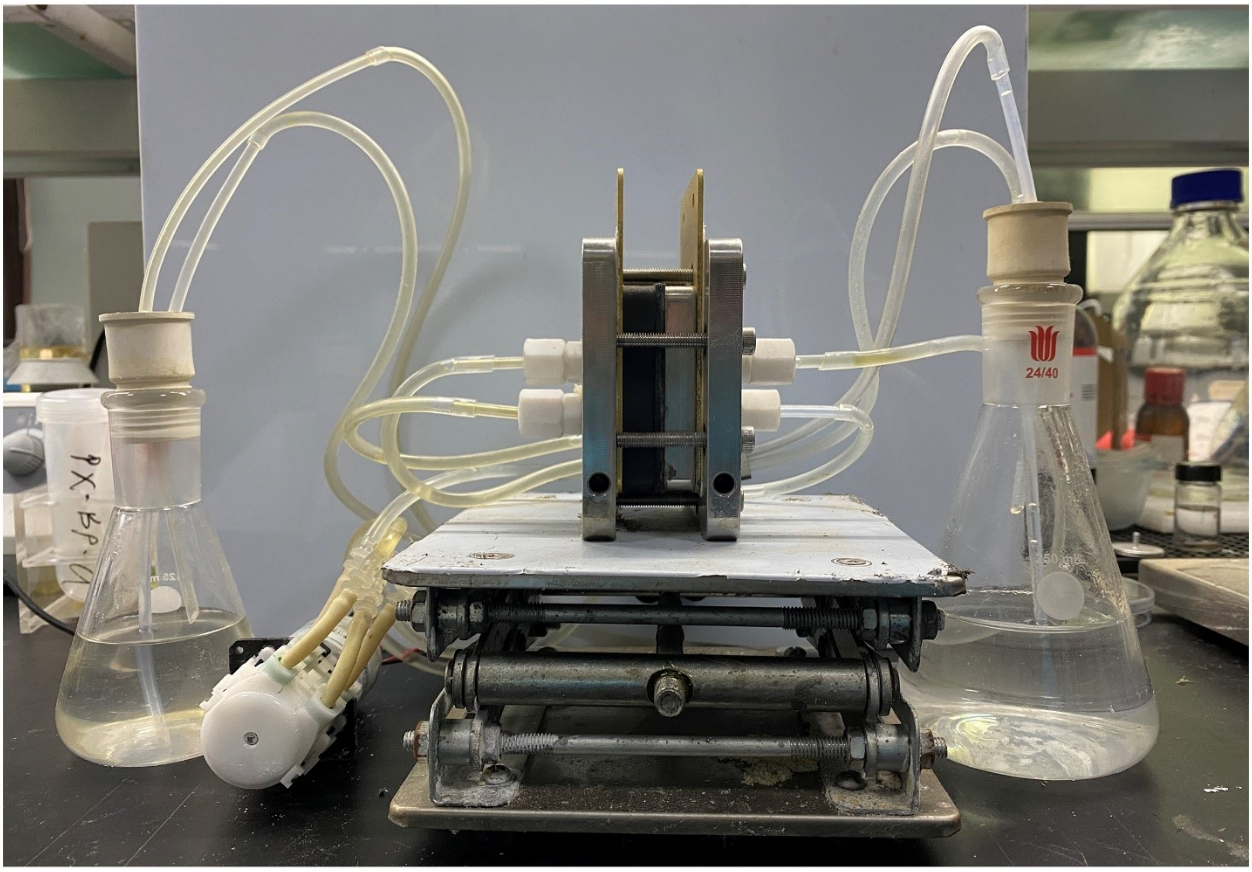

Fig. S30. Photography description of continuous NH_3 electrosynthesis flow cell system. The electrolytes were 1 M KOH/1 M KNO_3 (or 0.1 M KOH/1 M KNO_3^- for low concentration test) in cathode tank and is 1 M KOH in anode tank before startup, respectively.

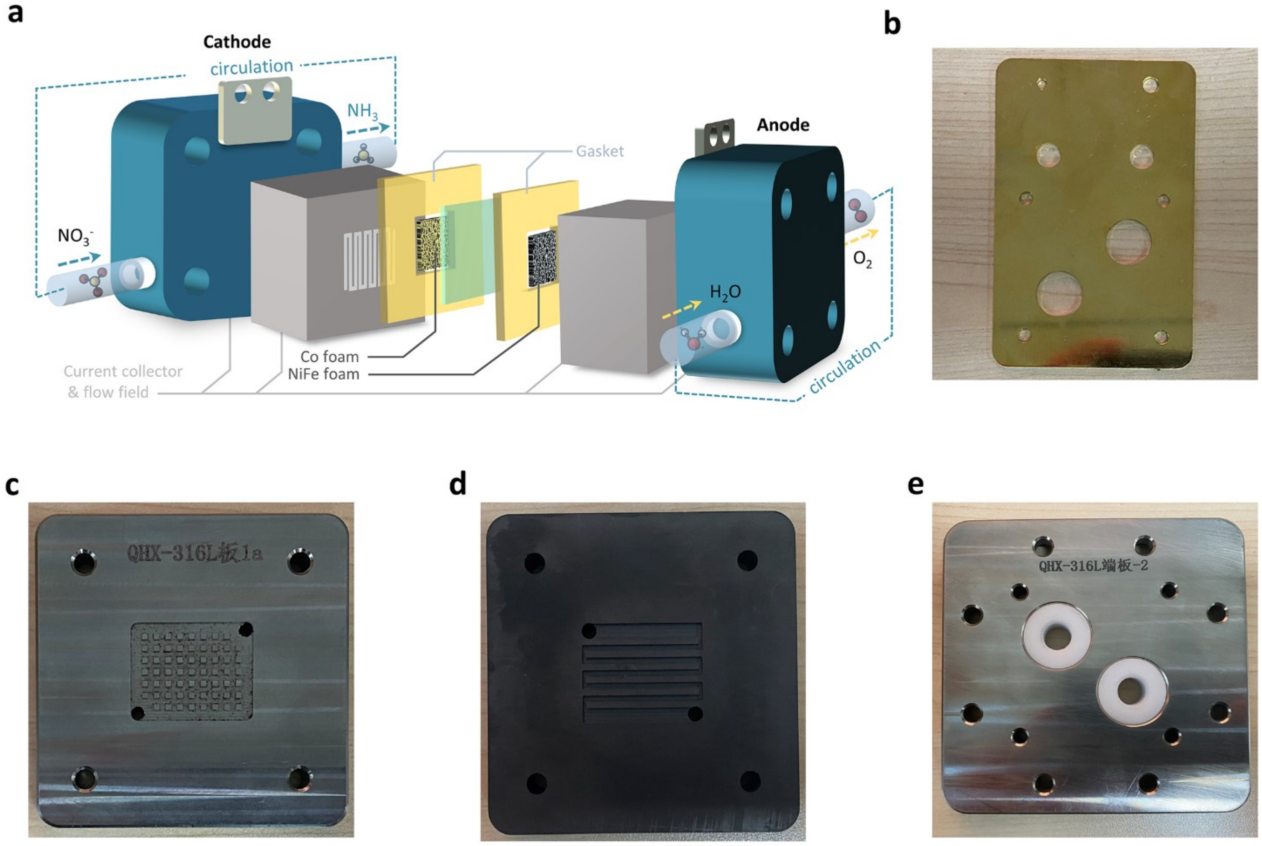

Fig. S31. **a,** systematic illustration of bipolar membrane flow cell. **b,** Photography description of continuous NH_3 electrosynthesis flow cell internal components: **b,** two current collectors (cooper plates overgild); **c,** anode flow (316L steel) with lattice channel and **d,** cathode flow (graphite) with snake channel; **e,** two endplates.

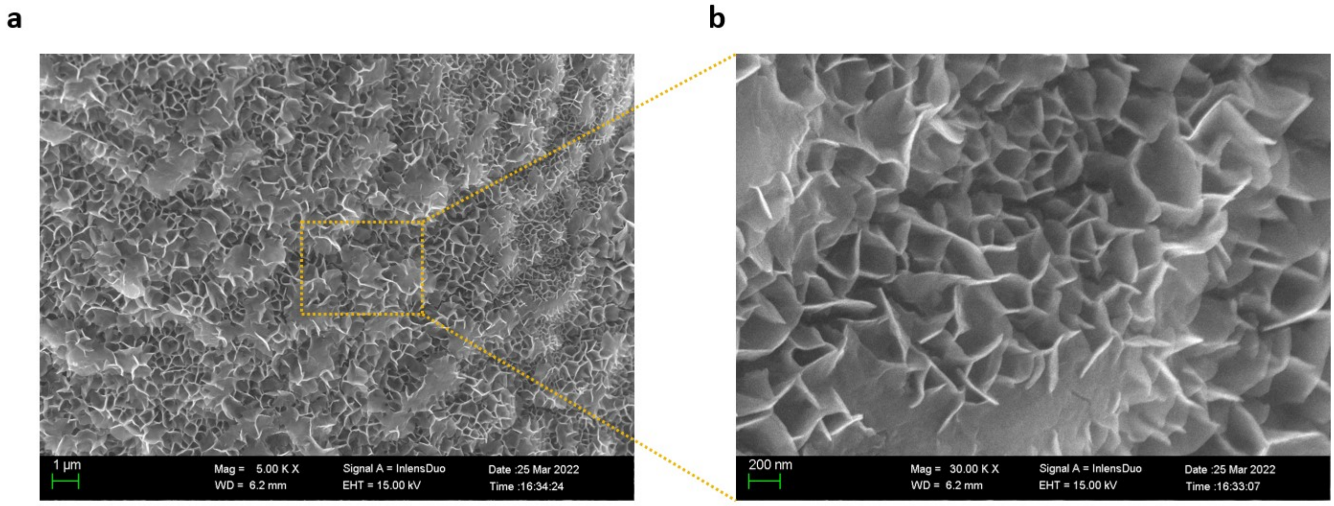

Fig. S32. SEM image with different magnification of NiFe nanoarray catalyst for oxygen evolution reaction at anode.

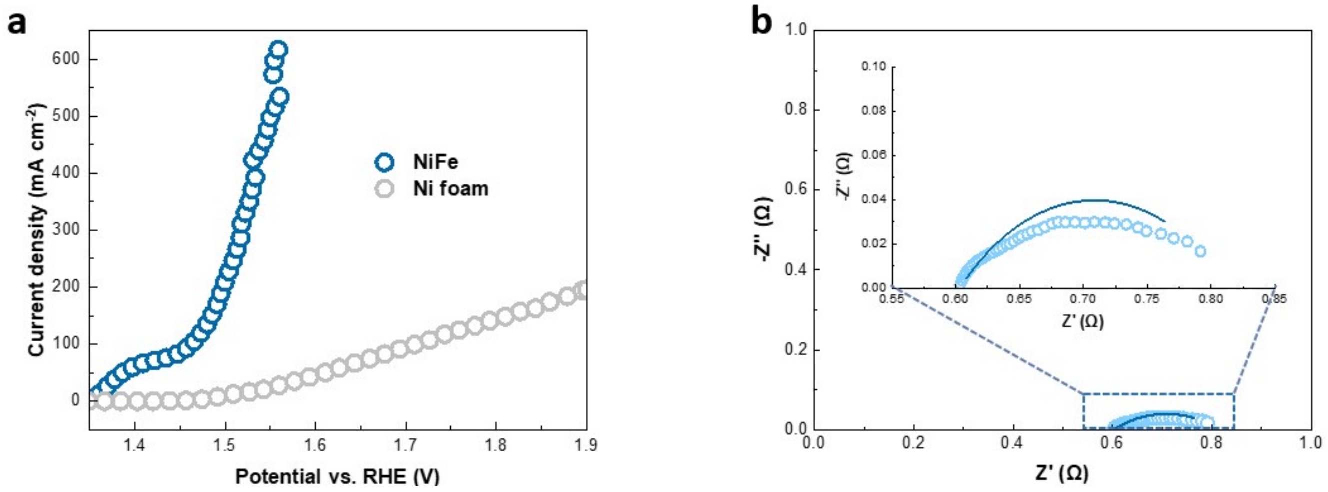

Fig. S33. Electrochemical measurements of NiFe anode for OER in 1 M KOH. **a,** I-V polarization curves of NiFe nanoarray and bare Ni foam at a scan rate of 5 mV s^{-1} with IR correction. **b,** EIS measurements at an oxygen evolution current density of ~10 mA cm^{-2}.

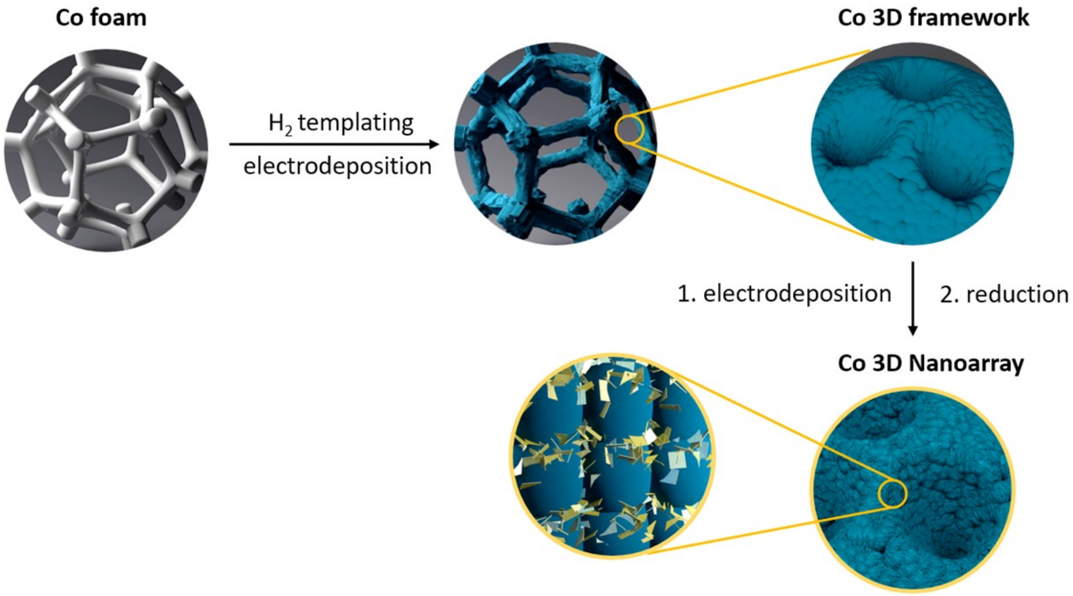

Fig. S34. Schematic showing the fabrication of Co nanoarray catalyst for NO_3^-RR

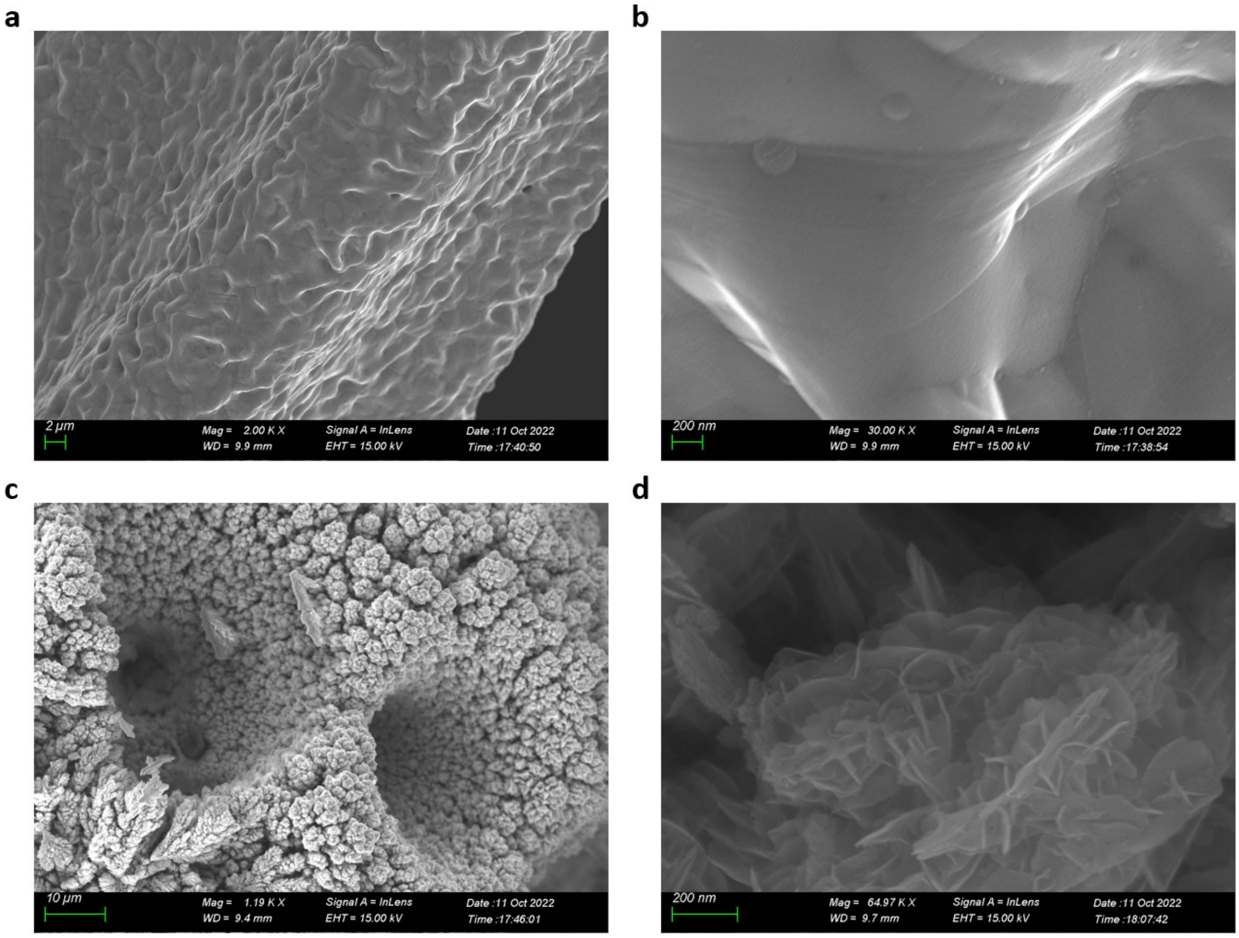

Fig. S35. SEM image with different magnification of **a, & b,** bare Co foam and **c, & d,** Co 3D nanoarray with multilayer structure.

Note: We found that the key factor to realize a high yield NH_3 producing with a low nitrate concentration is to enhance the ultilization of NO_3^- at high current density, which need us to construct bulky catalytic sites and promote mass transfer function. As proved in our recent research work, the self-standing nitrate reduction catalyst we adopted in the NH_3 flow cell possess a multi-layer structure, which can obviously intensify the mass transfer of NO_3^-. The porous of micrometers constructed by bubbling template method can offer a three-dimentional framework (Fig. S33c), which can boost effective surface area of nitrate reduction and help NO_3^- to reach the inner sites. Co nanosheets were further constructed on the 3D framework (Fig. S33d), through which catalytic sites with high activity were established. According to the research work, the electrocemical active surface area (ECSA) of Co 3D nanoarray was boosted to 43 folds to the bare Co foam (Fig. S33a, b)

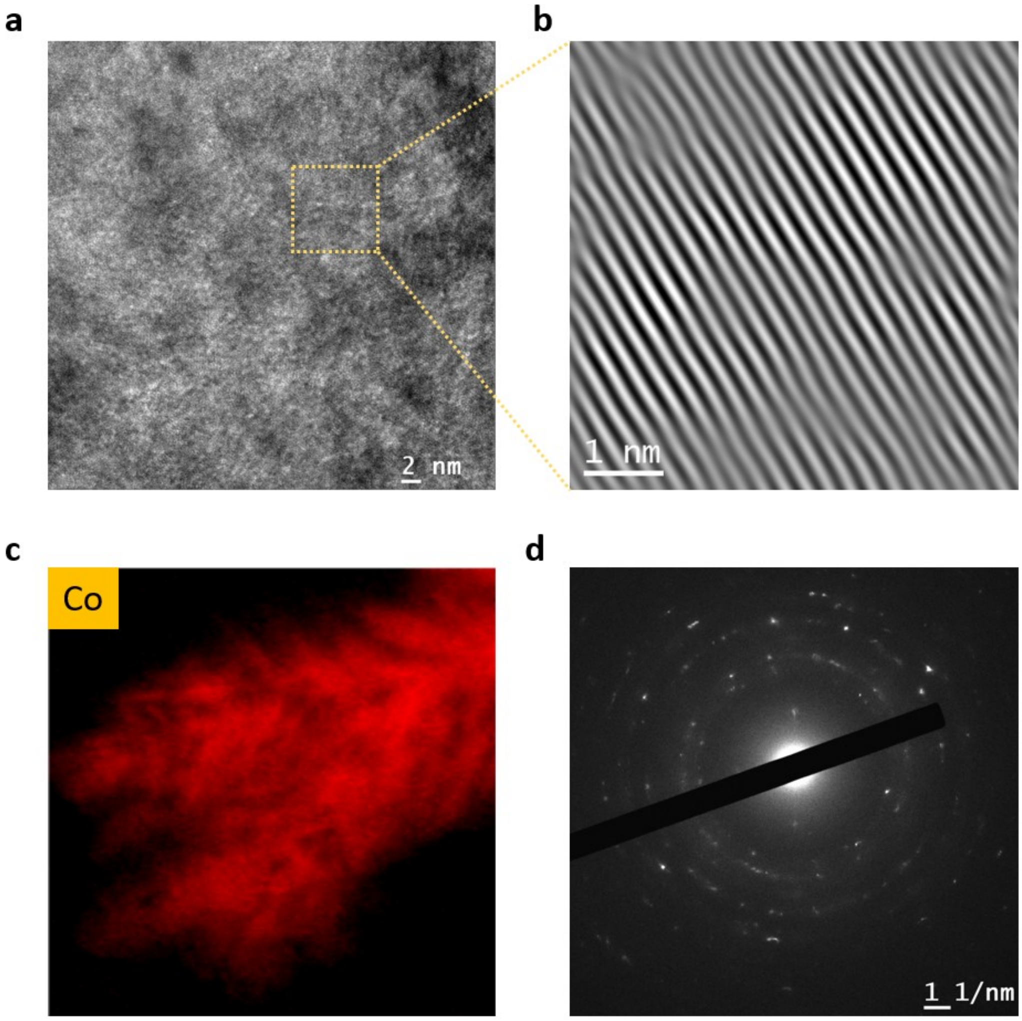

Fig. S36. a, and **b,** HRTEM image of nanosheets ultrasonificated from Co 3D nanoarray (the selected area magnified image of **b,** was obtained by a Fourier transform processing); **c,** EDX-mapping of nanosheets; **d,** SAED pattern of synthesised catalyst.

Note: As shown in the Fig. S34c, the catalyst we constructed is composed of Co element, which has been proved with high nitrate reduction performance before. The Fig. S34b and S34d revealed an obvious lattice distance of ~2 nm, according to (1 1 1) of Co^0. Other lattice spacing value, e.g. 2.46 nm, could be resulted by partially oxidized from Co^0 to CoO_x on its surface.

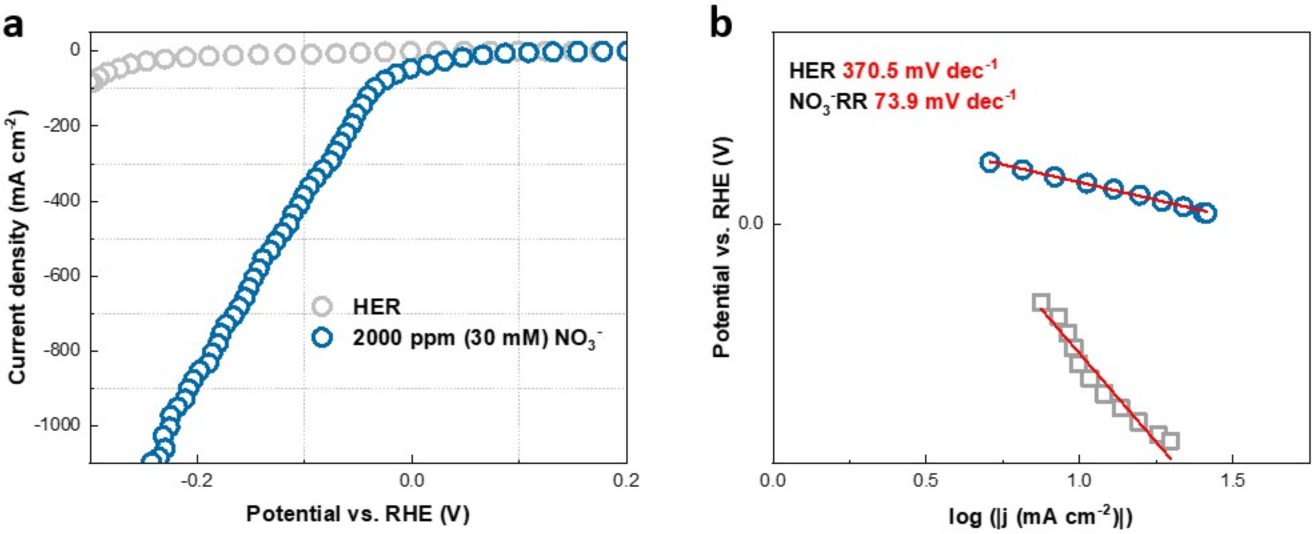

Fig. S37. Electrochemical measurements of Co 3D nanoarray with 1 M KOH. **a,** I-V polarization curve at a scan rate of 5 mV s^{-1} with (nitrate reduction) and without (HER) 2000 ppm NO_3^-. **b,** Co 3D nanoarray Tafel plots of nitrate reduction with 2000 ppm NO_3^- or HER process.

Note: As shown in the Fig. S35a, the current was boosted with a nitrate of a low concentration existed, indicating a high activity of Co 3D nanoarray as cathode catalyst. This can partly be attributed to the intrinsic activity difference of the material for NO_3^-RR and HER, as indicated by the Tafel plots in Fig. S35b.

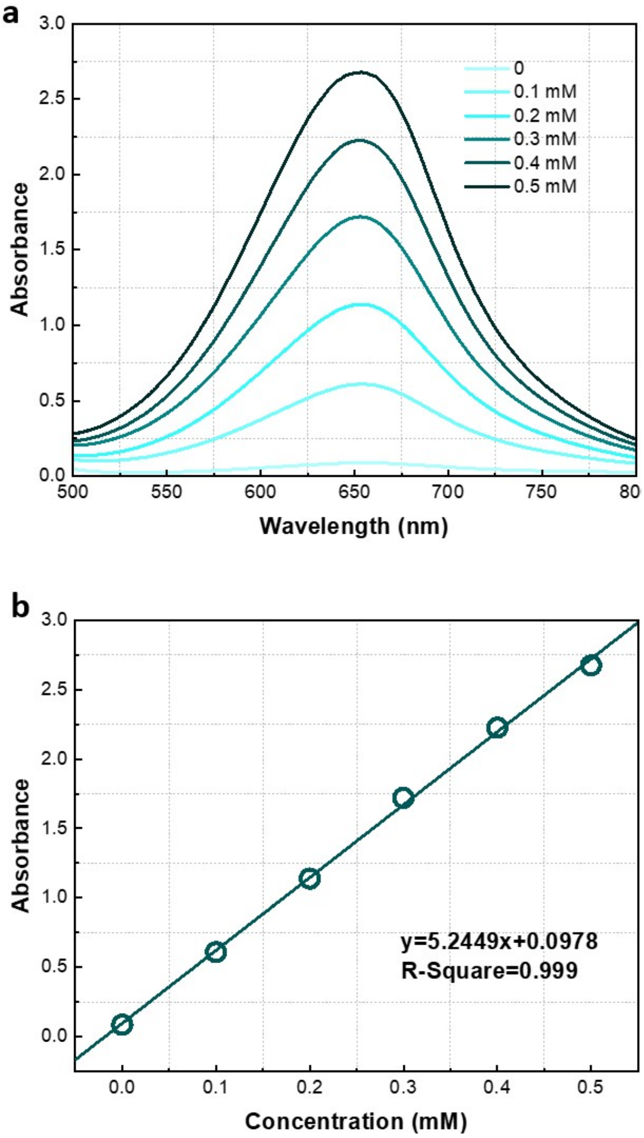

Fig. S38. a, UV-vis curve of 0, 0.1 mM, 0.2 mM, 0.3 mM, 0.4 mM, 0.5 mM NH_3 in 1 M KOH from 500 nm to 800 nm. **b,** standard calibration line of NH_3 in 1 M KOH.

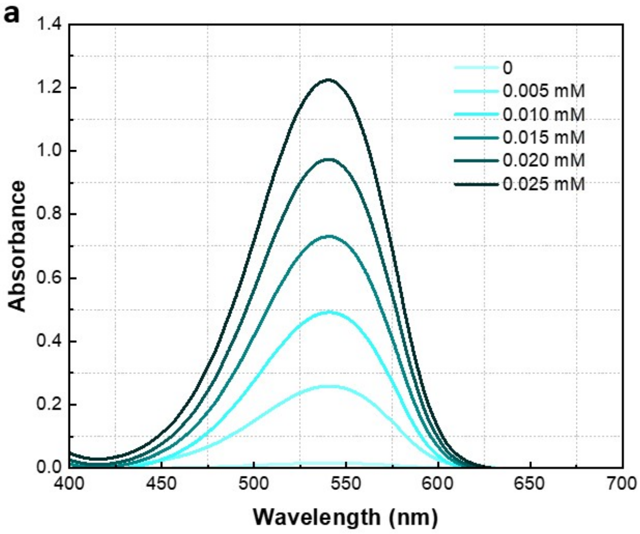

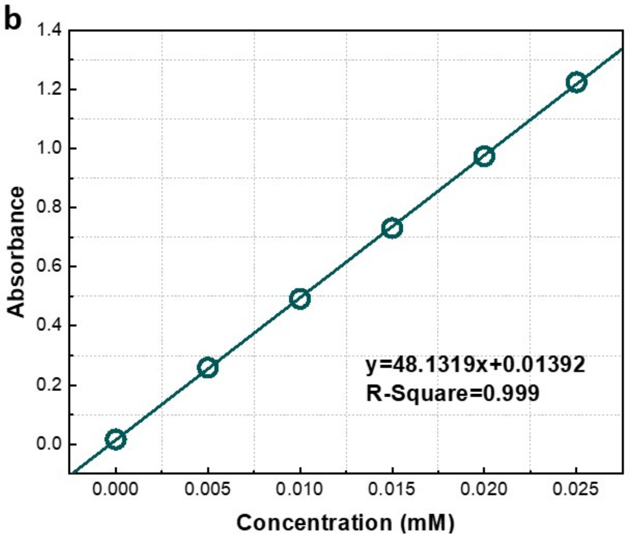

Fig. S39. a, UV-vis curve of 0, 0.5*10^{-5} M, 1.0*10^{-5} M, 1.5*10^{-5} M, 2.0*10^{-5} M, 2.5*10^{-5} M KNO_2 in neutral pH from 400 to 800 nm. **b,** standard calibration line of KNO_2 in neutral pH.

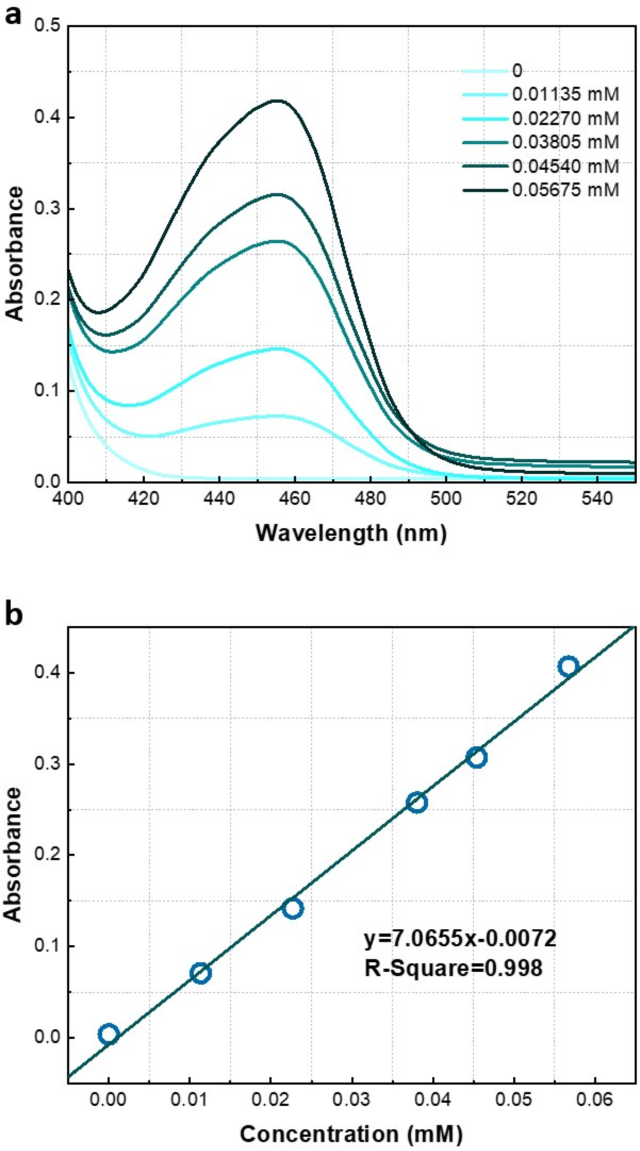

Fig. S40. a, UV-vis curve of 0, 1.135*10^{-5} M, 2.270*10^{-5} M, 3.805*10^{-5} M, 4.540*10^{-5} M, 5.675*10^{-5} M N_2H_4 in pH=3 from 400 to 550 nm. **b,** standard calibration line of N_2H_4 in pH=3.

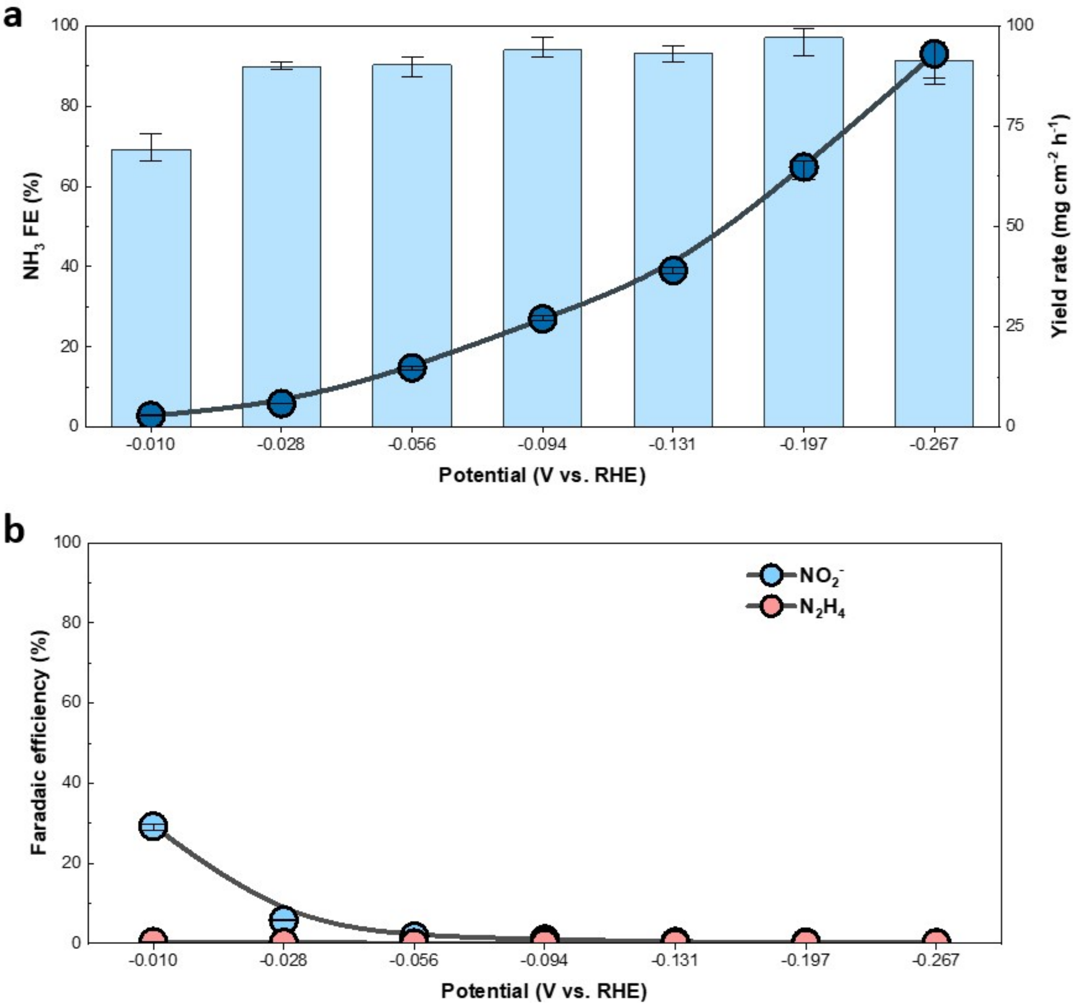

Fig. S41. a, NH_3 faradaic efficiency (bars, left Y axis) and accordant NH_3 yield rate (scatter-line, right Y axis) of synthesized Co 3D nanoarray catalyst with 2000 ppm KNO_3; **b,** Side products NO_2^- and N_2H_4 faradaic efficiency vs. potential of Co 3D nanoarray catalysts with 2000 ppm KNO_3.

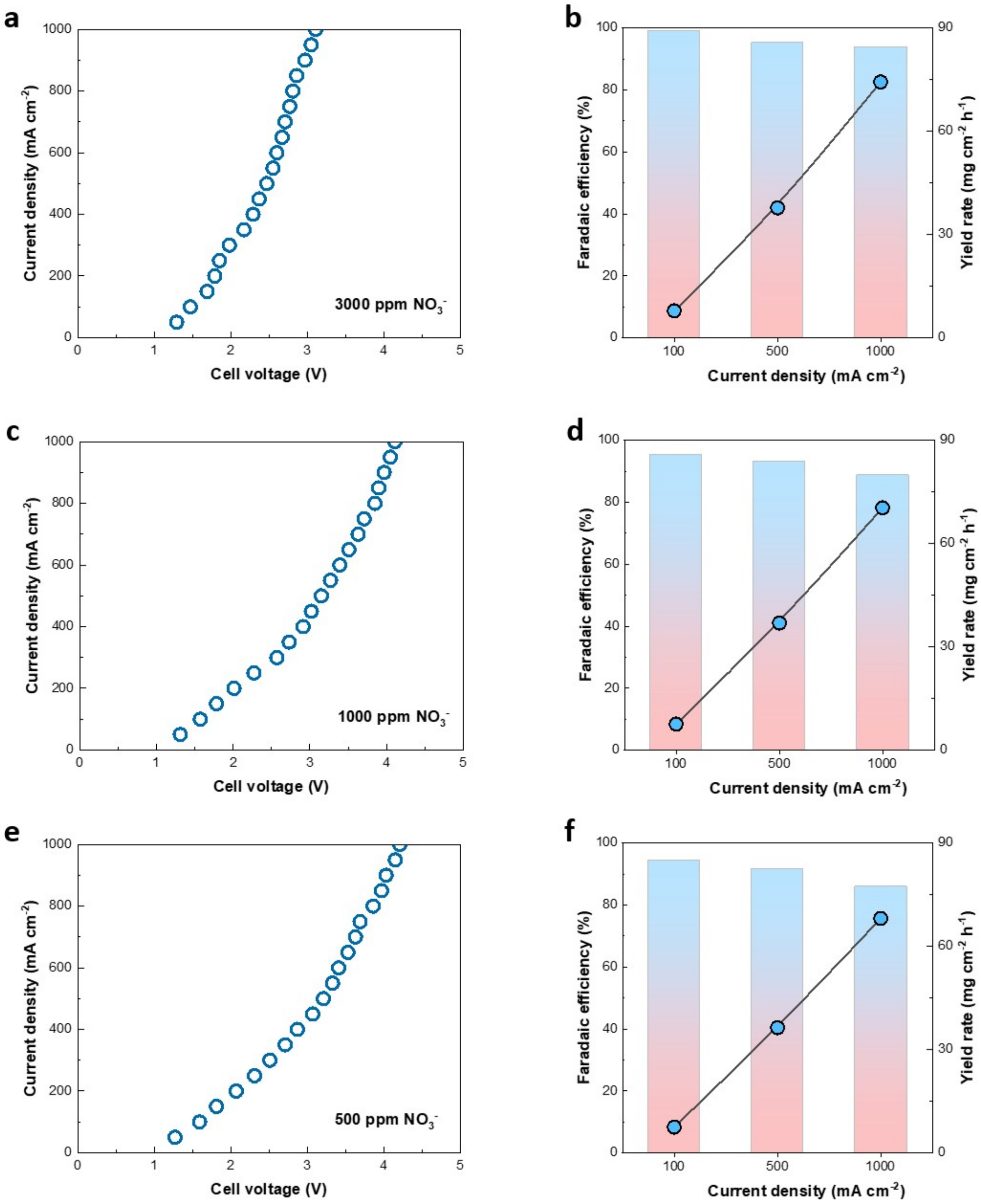

Fig. S42. Polarization curves, Faradaic efficiencies and NH_3 yield rate at varied current density of CIBM NH_3 electrosynthesis cell with nitrate concentrations of a,b, 3000 ppm or c,d, 1000 ppm or e,f, 500 ppm.

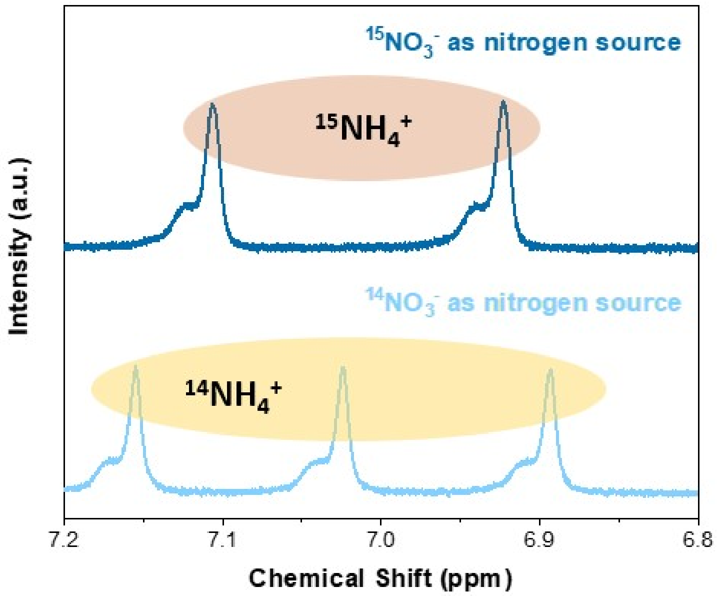

Fig. S43. Isotope labelling method ^{1}H NMR evidence of the product determination.

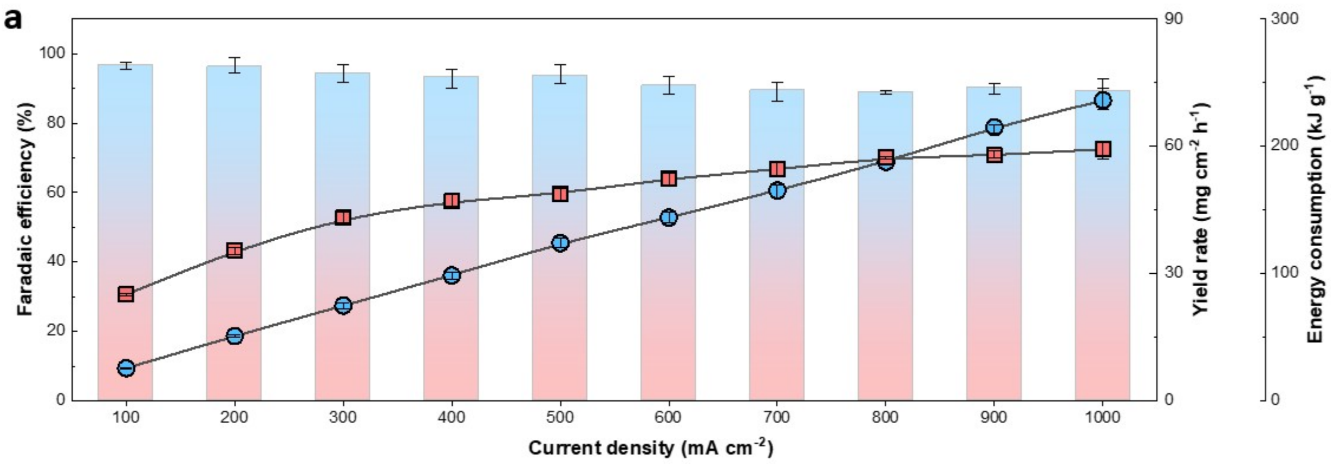

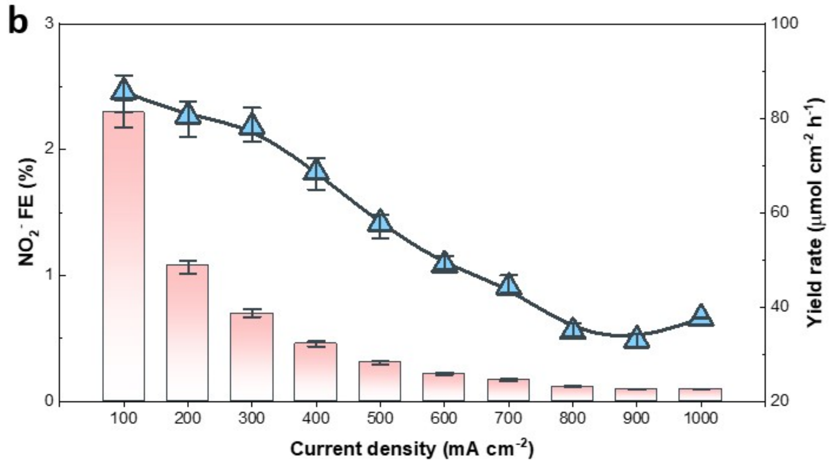

Fig. S44. a, NH_3 Faradaic efficiencies (bars, left X axis), yield rates (circular scatter-line, 1st right Y axis) and energy consumptions (rectangular scatter-line, 2nd right Y axis) of NH_3 electrosynthesis system equipped with CIBM using 2000 ppm KNO_3. **b,** Side products NO_2^- FE (bars, left Y axis) and yield rates (scatter-line, right Y axis) of CIBM alkaline NH_3 electrosynthesis systems with 2000 ppm KNO_3. Each experiment was repeated for three times.

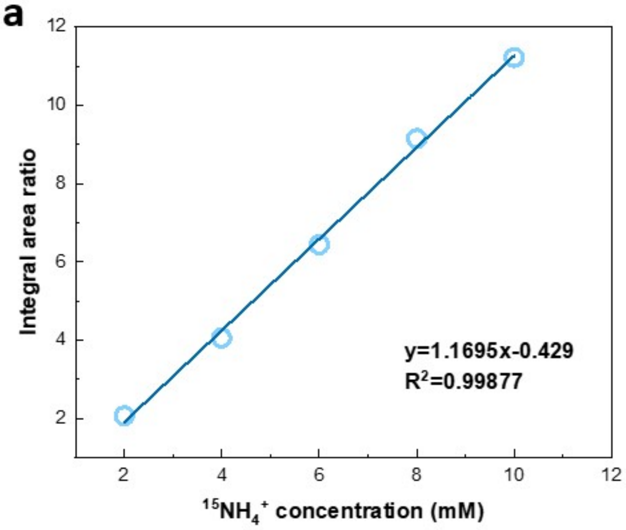

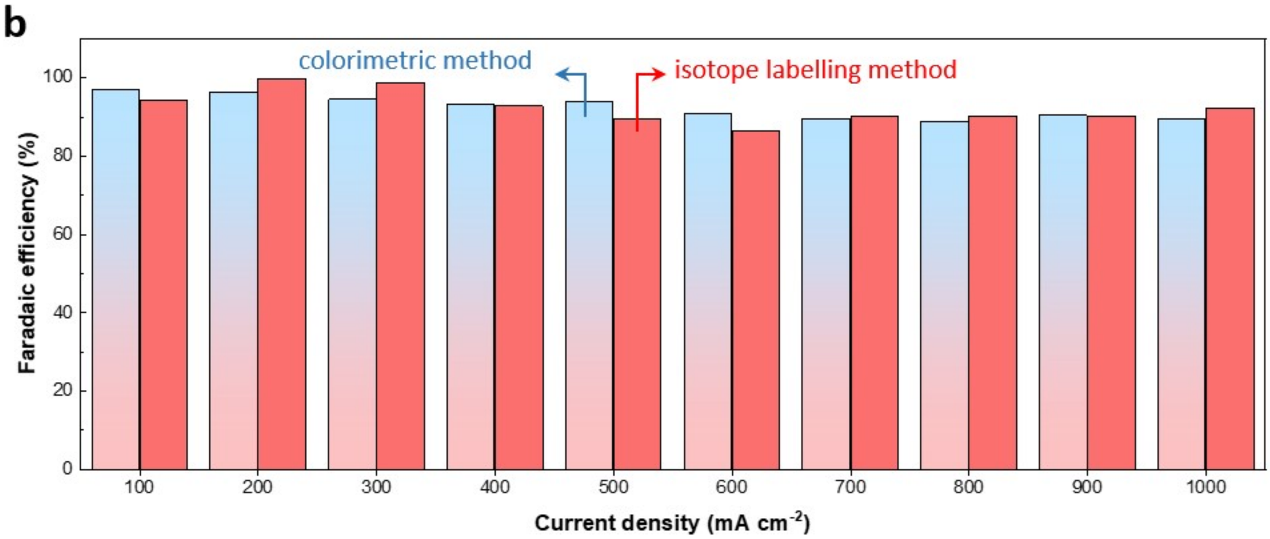

Fig. S45. N-15 isotope labelling experiments for NH_3 determination. **a,** calibration line of $^{15}NH_4^+$ concentration. **b,** the comparation of Faradaic efficiency between colorimetric method and isotope labelling method using $^{15}NO_3^-$ as merely nitrogen source.

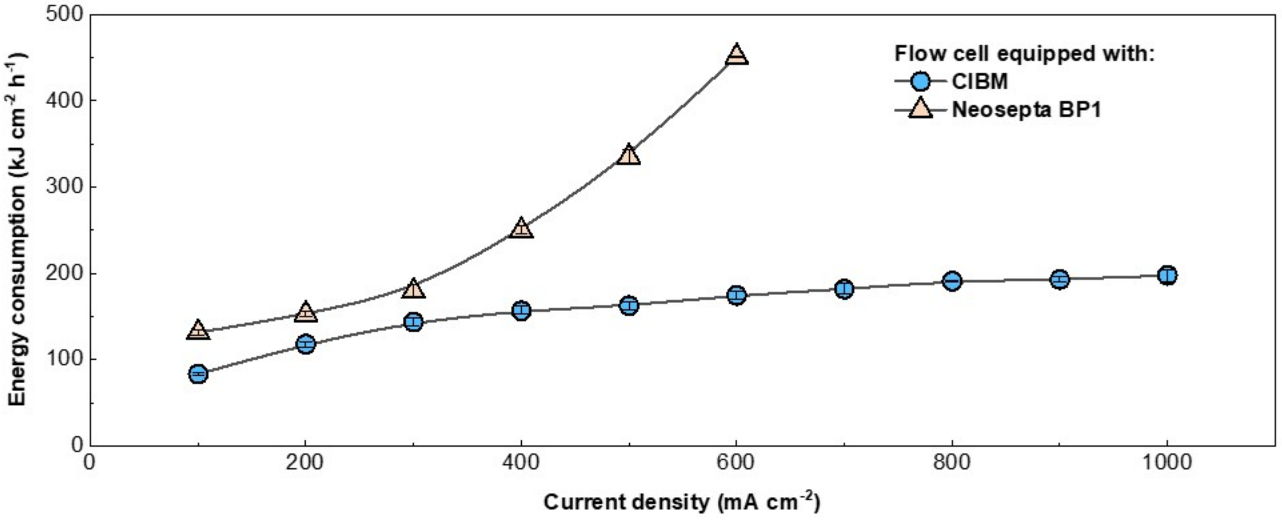

Fig. S46. The comparasion of energy consumption for producing NH_3 of equal mass by the established bipolar membrane NH_3 flow system equipped with CIBM or Commercial Neosepta BP1.

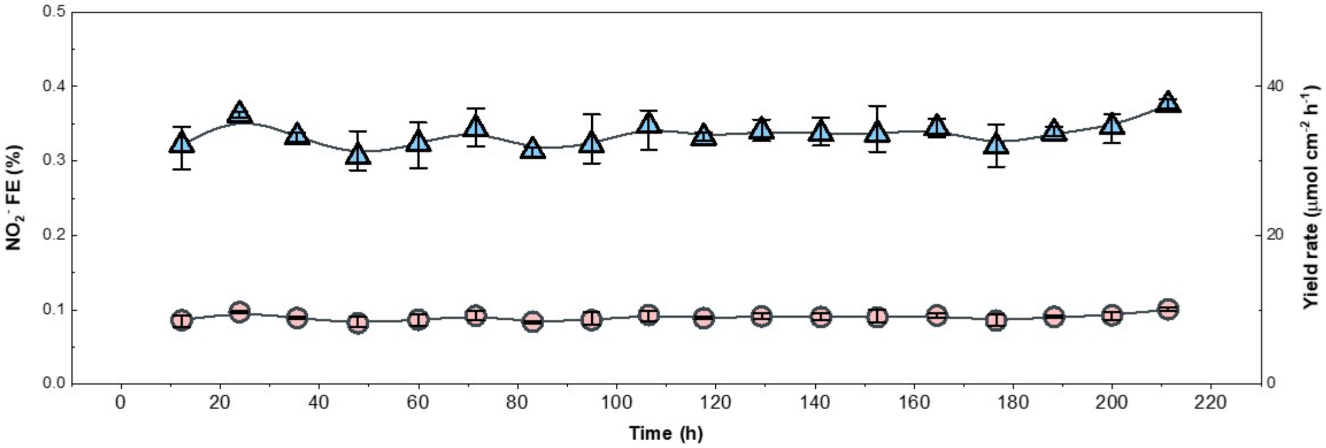

Fig. S47. a, Side products NO_2^- FE (bars, left Y axis) and yield rates (scatter-line, right Y axis) of CIBM alkaline NH_3 electrosynthesis systems with 2000 ppm KNO_3; **b,** produced NO_2^- recording during stability measurements. The NO_2^- FE and yield rates are represented by circular (left Y axis) and triangle (right Y axis) scatter-lines, respectively.

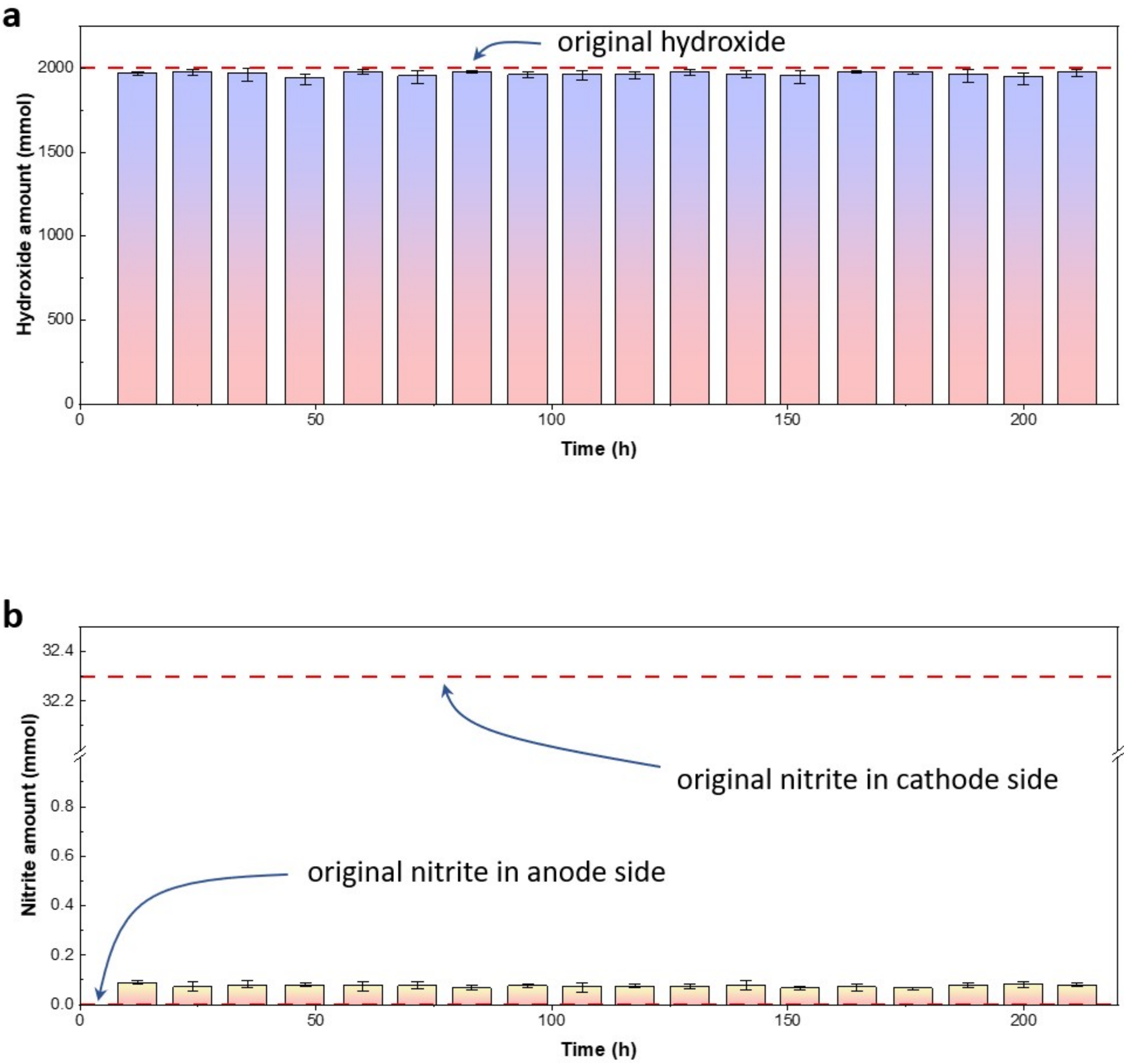

Fig. S48. ionic concentration maintanance during NH_3 electrosynthesis with the established bipolar membrane flow cell. **a,** hydroxide amount of anode side vs. operation time; **b,** nitrate amount of anode side vs. operation time.

Note: The ionic balance of the alkaline nitrate reduction to ammonia process could only be maintained by the bipolar membrane for a long period of operation, as stated in the **Supporting Note 3** and our recent research work. Either a single layer of cation exchange membrane or anion exchange membrane will lead to a severe ionic crossover of both sides. However, the imperfection of bipolar membrane will also lead to a slight ionic leakage, so we detected the concentrations of ions in anolyte to prove the feasibility of CIBM for this process. Because a H_2O migration can happen after long-term working and canses volumn change, we here take amounts of ions instead of concentrations as indicators.

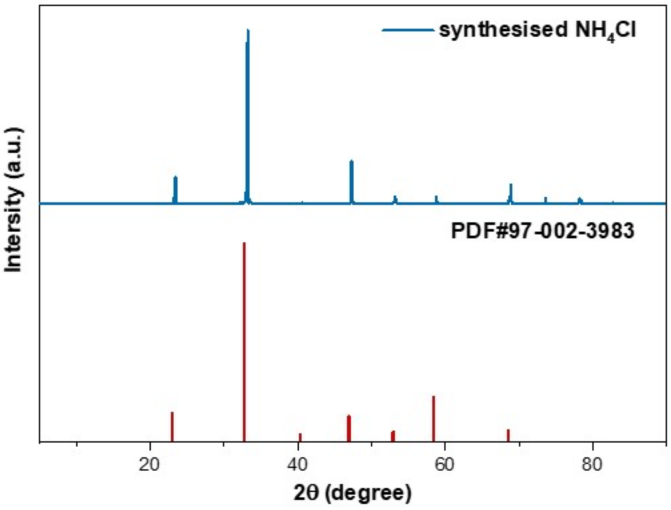

Fig. S49. XRD pattern of collecte NH_4Cl that acidified from the synthesised NH_3.

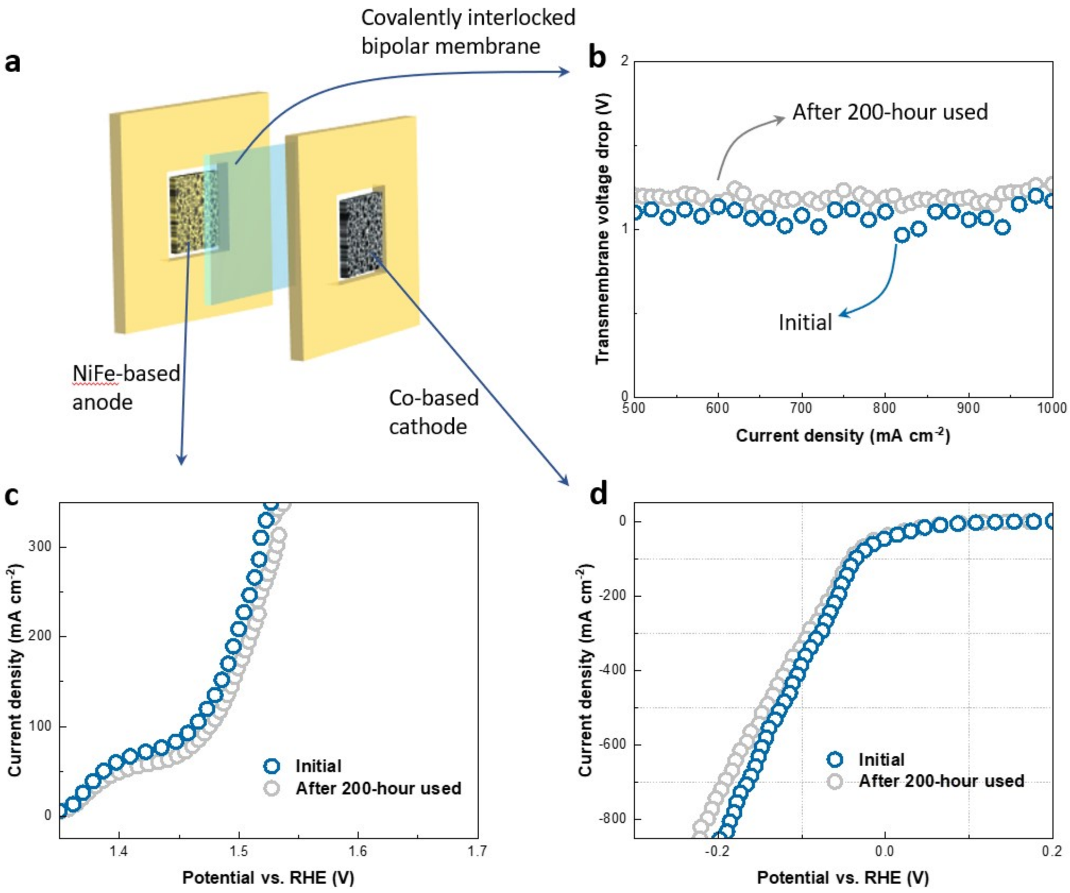

Fig. S50. a, schematic illustration of three key materials applied in the NH_3 synthesis flow cell. The performance maintenance of CIBM as separator, NiFe as OER catalyst and Co 3D nanoarray as NO_3^-RR catalyst, indicated by I-V change before and after 200-hour working, are showed in **b, c,** and **d,** respectively.

Note: It can be found that both the performance of the bipolar membrane and catalytic materials for cathode and anode revealed only a slightly decline after long-term stability test with high voltage applied. However, the fading of catalytic electrodes and separator didn't influence the overall performance of NH_3 electrosynthesis (FE or energy consumption) to a large extent in the 200-hour operation duration, indicating that the stability of materials should not be the limiting factor taking responsibility to the systematic efficiency at current stage. Nevertheless, both anode and cathode that can endure high voltage and alkaline system might be necessary to be explored further to achieve a more reliable and practical industrial NH_3 electrosynthesis.

Supporting comparation data (Table S1 and S2)

Table S1. Comparation of commercial or recently reported bipolar membranes based on points of WD efficiency (transmembrane voltage drops at 100 mA cm^{-2}, U100), ionic selectivity (1st limiting current density) and stability.

Bipolar membrane	**1st limiting current density /mA cm^{-2}**	**U100/V**	**Stability /hours**	**Publication year**	**ref.**
CIBM	**3.43**	**1.1**	**1100**	**This work**	
Neosepta BP1	3.47	1.27	<140	commercial	
Fumatech	7.1	1.394	-	commercial	
SBM-NC2.0	5	1.4	12	2022	10
SBM-D1.0	1.22	2.4	12	2022	10
HBM-SG10	2.4	4.3	-	2022	11
SCBM	6	1.1	140	2021	12
PIL-BPM	10	1.87	16	2021	13
BPM-E3	9	4	-	2021	14
Co-electrospun 3D bpm	5	1	14	2020	15
Fe(III)@PEI-	25	1.8	12	2020	16

based BPM					
junction1 BPM	7	1.1	-	2019	17
4GO-BPM	3	1.45	12	2018	1
BPM-PGO/QGO	8.75	>6	10 cycles	2018	18
LBL film	3	>1.6	-	2017	19
BPM-3D	5.9	0.95	-	2017	20
BPM-2D	5.5	1.2	-	2017	20
EBPM-2	10.5	2.4	-	2017	21
BPM-LYS	10.2	5.4	>2	2017	22
MIL 101-BPM	19	4.2	6	2017	23
Cu_2O/BPM	17	6	1	2016	24
GO-BPM	0.5	2.2	24	2015	25
BiOCl/BPM (irradiation)	7	5.2	-	2015	26
BiOCl/BPM (no irradiation)	7	6	-	2015	26
I-BiOCl BPM (irradiation)	9	5.1	-	2015	26
LBL interface	10	2.1		2013	27

& intermediate BPM					
LBL interface BPM	8	3.3		2013	[27]
Intermediate BPM	7	3.9	3	2013	[27]
PVA-CMC/nano-ZnO-CeO$_2$-CS BPM	10	5.6	-	2012	[28]
PVA-CMC/nano-CeO$_2$-CS BPM	10	5.9	-	2012	[28]
BPM-ZrOH	0.424	9	-	2012	[29]
BPM-SiOH	0.5	10	-	2012	[29]
BPM-TiOH	0.46	12	-	2012	[29]
BPM-3400	0.53	3.5	8	2011	[30]
BPM-2000	0.48	3.6	8	2011	[30]
mSA/CuTAPc-CS BPM	18	1.8	-	2010	[31]

Table S2. Comparation of 8e$^-$ NH_3 electrosynthesis systems reported in recent years based on membrane choice, catalyst species, NH_3 Faradaic efficiency, Max. current density, NH_3 yield rate and stability.

Catalyst	**NH_3 Faradaic efficiency /%**	**Max. current density /mA cm^{-2}**	**NH_3 yield rate /mg cm^{-2} h^{-1}**	**Stability /hours[a]**	**Publication year**	**Ref.**
Co nanoarray	**89.4**	**1000**	**70.9**	**220**	**This work**	
Ru-CuNW	95.6	963	76.512	110	2022	32
Fe_3O_4	91.5	150	12.263	8 cycles	2022	33
CoO@NCNT/GP	93.8	125	9.041	12	2022	34
GaInSn	100	12.8	2.335	10	2022	35
Co_xCu_{1-x}	95	176	-	6	2022	36
FOSP-Cu-X	93.91	-	0.1014	6 cycles	2022	37
i-$Cu_5Ru_1O_x$	95.3	~100	8.228	10	2022	38
Cu based	84.36	20	2.17	10 cycles	2022	39
Fe single atom catalyst	86	60.7	4.812	10 hours	2021	40
Pd	35	4.25	0.337	4	2021	41

Fe-PPy SAC	100	34.6	2.75	10 cycles	2021	[42]
fluorine doped carbon	20	10	-	10	2021	[43]
Ru-based	94	10	-	8	2021	[44]
$ZnCo_2O_4$	95.4	12	2.1	5	2021	[45]
nano-Ag	89.6	194.31	2.89	4 cycles	2021	[46]
Ni_2P	89.1	10	0.952	5	2021	[47]
$NiCu/MnO_2$	97.40	8	-	24	2021	[48]
Cu-PTCDA	85.9	5.49	0.435	40	2020	[49]
Cu/Cu_2O NWAs	95.8	52.5	7.136	6 cycles	2020	[50]
TiO_2-x	85	9.65	0.765	8 cycles	2020	[51]
Ti	82	22	1.744	8	2020	[52]
Ru nanoclusters	100	251	19.89	100	2020	[53]
Cu50Ni50 alloy	99.1	90	7.136	12	2020	[54]

[a] For some cases in previous reported data, the stability tests were conducted in batched mode, during which the electrolytes were refreshed for tens of minutes. By this means, every time the electrolytes were renewed was recorded as one cycle.

Supplement notes for Table S2:

In Table S2, we summarized the experimental data from most of the literature on nitrate reduction synthesis of ammonia published in the past three years. We mainly focused on the statistics of Faraday efficiency, maximum current density, ammonia yield and stability for different technologies, and discussed their advantages and disadvantages. In terms of catalysts, we noticed that researchers mainly used non-precious metal catalysts, including Co, Cu, Fe and other elements, which meet the requirements of batch preparation. However, in order to further improve the catalytic performance, some researchers doped a small amount of Ru element or used Pd metal catalyst in the catalyst and achieved significant results. From the perspective of current density, the Co catalyst (Co nanoarray) with multilevel structure used in this work can achieve ampere-level nitrate reduction due to its large specific surface area. In comparison, the maximum electrolysis current that most of the reported catalysts can achieve is only a few hundred or even a few tens of milliamperes. In the process of nitrate reduction with lower concentration, Co nanoarray can achieve 89.4% Faraday efficiency. Although many reported catalysts have exceeded this value, the test current is one order of magnitude lower. Only Ru-CuNW catalyst can be comparable to it, but the preparation of this catalyst cannot be separated from precious metal elements. In terms of stability, Co nanoarray combined with bipolar membrane flow cell can achieve the longest stability so far, which is 220 hours; most of the other data are tested in intermittent H-cell, which has shorter stability compared with it. Therefore, Co nanoarray has certain advantages in comprehensive catalytic performance, and it is also reasonable to use it in bipolar membrane reactor.

Supporting discussions (Note 1 to 4, containing Scheme S7 and Figures S47 to S48 and Table S3 to S5)

Note 1. One-dimensional modelling of BM interface to mimic the delamination of AEL/CEL and discussion of numerical simulation.

As shown in Fig. S8., a one-dimensional model was built to describe the WD process at interface of BM. 7 parts were altogether included in the model, referring to a cathode, an anode, two diffusion boundary layers, a cation exchange membrane layer, an anion exchange membrane layer and a low "average IEC" region. Among them, the thicknesses of both membrane layers are 50 μm, while they were set with different charge density to mimic real situation (AEL-2.8 mmol cm^{-3}; CEL-0.9 mmol cm^{-3}).

Based on the consideration that the delamination or ballooning of BM can generate an uneven "charge vacancy" region, where is filled with electrolytes instead of polymer. Thus produced H^+/ or OH^- generated by WD can suffer from higher transportation barrier to move and reach membrane layer without the help of fixed functional groups. To describe this phenomenon in our modelling process in a simple way, a low "average IEC" region with the thickness of 0.1 μm was set between cation and anion exchange layers. By this means, the delamination of membrane layers is averaged to different position, and the concentration of fixed charge here is obviously lower than main region of membrane layer. Moreover, a series of model with different value of low "average IEC" region was set to describe BM with different degree of delamination. According to the above consideration, the lower IEC value this region possesses, the more severe delamination occurred.

A Numerical simulation is easy to proceed according to the established modelling. The operation was set to perform in neutral (0.5 M Na_2SO_4) in a reverse bias (1 V, 2 V) of bipolar membrane, when WD happened at the interfacial region and H^+ and OH^- can be generated. As previous reported, Poisson's equation and the Nernst-Planck equation can be induced to describe the potential distribution and ionic transport[55, 56]. Moreover, Onsager's weak electrolyte theory tells us WD kinetics can be affected by electric field[57, 58]. All parameters and initial conditions referred for simulations are listed in the table S3 as followed[59]:

Table S3. Referred parameters for numerical simulation to describe delamination at bipolar membrane interface.

Parameter	**Value**	**Description**
L_mem	0.0499[mm]	Membrane thickness
L_low	0.0001[mm]	Low IEC region thickness
L_sdl	0.01[mm]	Diffusion boundary
c0	0.5[kmol/m^3]	Initial concentration
delta_phil	0[V]	Initial cell voltage
c_fixCEM	0.9[kmol/m^3]	CEM Membrane fix charge
Kw_0	10.64e-14[M^2]	Water dissociation constant at zero field
T	25[degC]	Temperature
A	0.5[K^2*m/V]	Wien effect coefficient (by Onsager relation)
eps_r	78	permitivity
D_H	9.312e-5[cm^2/s]	Diffusivity
D_OH	5.26e-5[cm^2/s]	Diffusivity
kw_r	5e11[M^-1*s^-1]	Backward rate constant water dissociation
c_fixAEM	2.8[kmol/m^3]	AEM Membrane fix charge
D_Na	1.334e-5[cm^2/s]	Diffusivity
D_SO4	1.065e-5[cm^2/s]	Diffusivity

ε	0.05	electrolyte volume fraction
Low-IEC	attenuation coefficient * c_fixCEM/ c_fixAEM	IEC of low IEC region

All equations used for numerical simulations are listed and were programmed and solved with COMSOL v 5.6:

$b = max(A * abs(E)/eps\_r/T^2,eps)$

Where b is Help variable,

$E =- d(phil,x)$

Where E is Electric field,

$w = Kw\_0 * max(besselj(1,(2 * sqrt(2 * b) * i))/(i * sqrt(max(b,eps))),1) * sqrt(1/2)$

Where Kw, using Bessel function from Onsager relation:

$kw_f = Kw * kw\_r$

Where kw_f is Forward rate constant,

$rw = kw\_f - kw\_r * max(cOH,eps^2) * max(cH,eps^2)$

Where rw is Reaction rate, water autoprotolysis.

Discussion for numerical simulation results.

As shown in Fig. 1a and Fig. S9-S10, the concentration profile of both H^+ and OH^- reveals distinct difference between the BM with or without low “average IEC” region, no matter for near the interface or for the whole bulk layer. This phenomenon demonstrates that the delamination will obviously hamper ionic moving and decrease overall interfacial WD kinetics. Moreover, a lower value of IEC at interface can further decrease the ionic concentrations (from 0.875 to 0.250 of bulk IEC value) and even negligible H^+ or OH^- can be generated when reached 0.250, indicating that the performance decay of BMs in real application can be reasonably ascribe to the membrane layer blistering. This decay is usually enlarged versus the operation duration, during which delamination become more severe, in accordance with the lower average IEC value at the membrane interface. Meanwhile, a higher of applied voltage (form 1 V to 2 V) in reverse bias mode can to some extent alleviate the performance decay for the BM with same delamination. This result indirectly proved that the sluggish WD kinetics is caused by the hindered ionic motion, because the mass transportation is driven by electric field and a higher diving force can promote this process. To be note that, the WD constant rate at all situations was set to be same for approximate identical WD catalysts applied.

On the other hand, the concentration profile of Na^+ and SO_4^{2-} were also derived as the inert ions existed in the electrolyte. As shown in Fig. S11-S12, the cations and anions distribution also of original or blistered BMs also reveals discrepancy. As a normal situation, the concentration of these “inert” ions near the interface is lower compared to the region far from the interface at relatively large WD current density, because the ions will be “depleted” under reverse electric force and gather at the interface of membrane and electrolyte. However, a low ability of delaminated BM to transfer charged ions results a relative higher concentration of Na^+ and SO_4^{2-} near the interface. Similarly, a higher driving force of 2 V also decrease this effect, while can hardly avoid under severe delamination situations.

Note 2. Explanation of EIS measurements for describing the interfacial transportation kinetics of CIBM and NIBM

As shown in inset of Fig. 2g, an equivalent circuit containing 3 main part was adopted to describe the overall mass transfer process of BMs, including an ohmic resistance (R_{Ω}), an ionic transportation resistance (R_{CT}) parallel to a constant phase element (CPE). These individual parameters can be derived from the fitting results of the Nyquist plot[1, 2, 60]. Among them, R_{Ω} describes the rate ions moving in the membrane, which can be derived from the high frequency region. R_{CT} and another parameter depletion layer thickness can be obtained from the medium frequency region, and these two parameters can describe mass transfer behavior of BM interlayer in details. Even though there were divergence according to previously reported works, most equation deducing revealed similar conclusions: i) R_{CT} can be influenced by the WD reaction rate, but mainly decided by complexity for ions to achieve membrane layers and the integrity of interface when WD catalyst of same species and similar amount are adopted. ii) depletion layer thickness is based on an electric double layer theory of BM interface to describe a non-ionic region caused by ions outwardly travelling, and a thinner thickness represents for a higher rate of ions to replenish the "depleted" region. To be note that there sometimes be a Gerischer impedance to describe the WD reaction rate, and it is determined by low frequency region of EIS. Nevertheless, such intrinsic catalytic performance is decided by the WD catalysts and is omitted in this work.

Specifically, the calculation method for depletion layer thickness is based on the equations (11-12):

$$C = R_{CT}^{\frac{1-n}{n}} Q^{\frac{1}{n}} \#(11)$$

$$d = \frac{\varepsilon_0 \varepsilon_r A}{C} \#(12)$$

Where Q and n are the pseudo-capacitance and CPE order, respectively; ε_0 and ε_r are respectively the vacuum electric permittivity and the dielectric constant in the reaction layer (80 was taken for pure water), and C and A are the capacitance and active membrane area. Other parameters calculated from the EIS Nyquist plot fitting results showed in Table S4 below:

Table S4. Fitting results derived from EIS measurements of CIBM and NIBM.

	Chi-Squared`	R_{CT}/Ω	n	Q	C/μF cm^2	δ/nm	Rs/Ω
CIBM	0.0107	3.51	0.97	1.40×10^{-5}	1.07×10^{-5}	6.59	3.72
NIBM	0.0082	21.54	0.83	5.77×10^{-6}	1.09×10^{-6}	65.07	1.20

To be mentioned, all the parameters were obtained from the EIS measurements at 20 mA cm^{-2}, which was absolutely over 1st limiting current density and the WD was happening.

Note 3. Necessity of using bipolar membranes to realize continuous NH_3 electrosynthesis via $8e^-$ NO_3^-RR process and advantage of adopting a flow cell as a proof-of-concept for this process.

i) The best environment for NH_3 electrosynthesis is an alkaline electrolyte, for several reasons below: firstly, an alkaline pH is kinetically advantageous for an oxygen evolution reaction (OER) at the anode side compared to an acidic environment, and non-noble catalysts can be used under this circumstance. Secondly, an alkaline environment can suppress hydrogen evolution reaction (HER, as a kind of side reaction) for the cathode side, thus faradaic efficiency can be promoted. Consequently, an alkaline electrolyte should be adopted (e.g., 1M OH^-) for NH_3 producing.

ii) Based on the above cognition, the bipolar membrane is the only choice to realize a continuous NH_3 electrosynthesis in alkaline systems. We know that an ion exchange membrane is necessary to be adopted to realize separating of anode and cathode side, so that produced NH_3 will be restricted at cathode, avoiding being re-oxidized to N_2.

As shown in Scheme S7, even though most reported works adopted cation exchange membranes (CEM) (e.g., Nafion series), a long-term electrolysis can hardly be maintained under this situation. When an CEM is applied, metal ions (Na^+ or K^+) will play as charge carriers to across the membrane; however, these alkali metal ions cannot be consumed or replenished after a period of operation, and severe unbalance of ionic species can bring about a reverse potential, which is also time dependent. It means a higher transmembrane voltage will be consumed to maintain a constant electrolysis current though every part of the materials (membrane or electrode) keeps stable. Thus, a steady-state electrolysis system can hardly be achieved by using CEM, which is not appropriate for industrial application.

On the other hand, an anion exchange membrane (AEL) is also tried to be applied for NH_3 electrosynthesis. Unfortunately, existed AELs does not possess the function of separating monovalent ions of NO_3^- and OH^-, so when OH^- is moving as charging carrier, NO_3^- will also crossover the membrane, causing severe reagent leakage.

The solution put forwarded here is to adopt a BM to separate the anode and cathode electrolytes. Due to the Donnan exclusion, neither anions nor cations can cross the whole layer of BM when a voltage is applied, thus crossover or ionic unbalance can be solved. When an electrolytic potential is applied, WD can happen at the interface with

H^+/OH^- moving outwardly, and they can act as charge carriers. By this means, a long-term and practical NH_3 electrosynthesis form nitrate can be realized. The reactions that referred in the process are listed as followed:

Cathode: $NO_3^- + 8e^- + 6H_2O \rightarrow NH_3 + 9OH^-$

Anode: $8OH^- - 8e^- \rightarrow 4H_2O + 2O_2$

Bipolar membrane interlayer: $H_2O \rightarrow H^+$ (neutralized) + OH^-

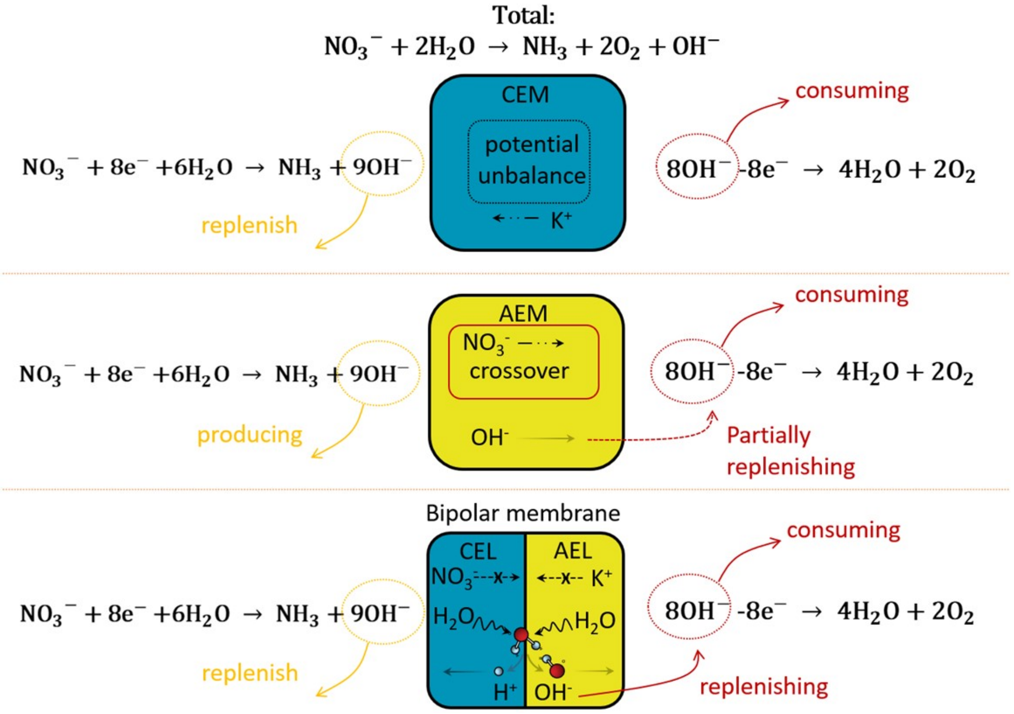

Scheme S7. illustration of necessity for adopting bipolar membranes in NH_3 electrosynthesis process.

iii) Even though most previous works are completed in an H-cell with three-electrodes measurements, we adopted a flow cell setup for NH_3 electrosynthesis process. According to other kinds of energy conversion devices, e.g., water electrolysis, CO_2 reduction or fuel cells, a flow cell can to a great extent low the distance between the membrane and the electrodes, thus resistance of electrolytes can be minimized. Besides, we find most efforts have been put on the catalytic materials for NO_3^-RR, while an extremely high performance has been achieved for many times. Therefore, the developments of NO_3^-RR drive NH_3 electrosynthesis into next stage and we focus on the overall energy consumption and operation stability of the whole system instead of merely cathodic overpotential in this work.

To be note that there are two possible side reactions happening at the cathode simultaneously during NH_3 producing as followed[40, 49]:

$$NO_3^- + 2e^- + H_2O \rightarrow 2NO_2^- + 2OH^-$$

$$2NO_3^- + 14e^- + 10H_2O \rightarrow N_2H_4 + 16OH^-$$

The amount of side products (NO_2^- or N_2H_4) were also detected with the samples of catholytes after electrolysis according to the experimental methods.

Note 4. Techno-economic analysis of bipolar membrane fabrication and nitrate reduction to ammonia process by using CIBM as the separator.

In this part, we conducted the techno-economic analysis of the proposed process in two steps, including a cost analysis and evaluation of CIBM fabrication followed by a net present value of ammonia electrosynthesis process. An extra sensitivity analysis is also included to help to Fig. out the key factors that influence the cost value.

i) The calculation of MBM fabrication cost and comparation with commercial bipolar membranes.

Table S5. Chemical prices referred in the bipolar membrane fabrication process. The prices of product can be searched on https://www.alibaba.com.

Name of chemicals	Usage amount (UA, kg/m^2 MBM)	Price (P, \$ kg-1)
p-Terphenyl	0.018	219.7
1-Methyl-4-piperidone	0.006	77.0
Trifluoromethanesulfonic acid	0.16	68.6
Trifluoroacetic acid	0.016	29.9
Dichloromethane	0.08	14.4
1,6-Dibromohexane	0.015	14.5
Potassium iodide	0.018	33.8
4-(Chloromethyl)styrene	0.002	303.5
Dimethylamine	0.015	4.5

Sodium 4-vinylbenzenesulfonate	0.011	18.9
Tetrabutylphosphonium bromide	0.018	161.3

The cost of chemicals and consumable items for producing MBM is:

$$COST_{MBM} = \sum UA \times P = \$21.63\ m^{-2}$$

According to the data from DONGYUECHEM Co., the extra consumption of chemicals takes up 10-15% of the theoretical value. Here we set 15% for further calculation. Moreover, the total utilities and staff salary payment takes up 300-400% of consumable items. Here we set 400% as an example:

$$Total\ COST_{MBM} = 150\% \times COST_{MBM} \times 500\% = \$162.22\ m^{-2}$$

Table S6. The costs comparison of MBM and other commercial bipolar membranes. The data can be obtained from fuelcellstore.com or https://www.alibaba.com.

Name	CIBM	Fumasep FBM	TRJBM	Xion-BPM	Neosepta BP1
Price (\$ m^{-2})	162.22	4733.3	2182.8	49671.1	1350

According to the data, CIBM enjoys large advantage of its low cost as compared with other commercial bipolar membranes designed for electrodialysis or electrochemical devices.

ii) The techno-economic analysis of bipolar membrane NH_3 electrosynthesis process.

a) Analysis of flow rate

If the Faradaic efficiency could be maintained at 90% and the operation current was kept steady at 1000 mA cm^{-2}, we can obtain the volume percent of NH_3 in the exiting electrolyte when set the flow rate in the electrolyzer as 0.1 mL/min:

$$Exit\ concentration\ NH_3 = \frac{900\ mA}{8e^- \times 96485\ C/mol} \times \frac{60\ s}{min\frac{17\ g}{mol}\frac{mL}{0.617\ g}\frac{0.1\ mL}{min}}$$

Note: The simplify the calculation process, the circulation mode was replaced by a single stream with slow flow rate.

Assuming a production rate of 0.01% of worldwide NH_3 consumption with this method, which equals to ~100000 kg/day, the partial current can be obtained:

$$100000\ kg/day \times \frac{1\ day}{86400\ s} \times 1000\ g/kg \times \frac{1\ mol}{17\ g} \times 8\ e^- \times 96485\ c/mol = 52551742\ A$$

So, total current need to be applied is:

$$Total\ current = \frac{52551742\ A}{0.9} = 58390824\ A$$

The active area for achieving total current can be calculated as:

$$Total\ area = \frac{58390824\ A}{1\ A/cm^2} \times \frac{m^2}{10^4\ m^2} = 5839\ m^2$$

The total power consumption is:

$$Total\ power = VI = 3.89\ V \times 58390824\ A \times \frac{W}{1000000\ MW} = 227\ MW$$

The mole of NO_3^- needed is:

$$NO_3{}^-\ amount = 52551742\ A \times \frac{1}{8e^- \times 96485\ C/mol} \times \frac{86400\ s}{1\ day} = 5882353\ mol/day$$

Assuming the industrial effluent contains 2000 ppm (30 mM) nitrate, and an 80% single pass conversion was set as goal. The effluent inlet flow is:

$$effluent\ inlet\ flow = 5882353\ mol/day \times \frac{1\ day}{24\ h} \div 80\% \div 30\ mol/m^3 = 10212\ m^3/h$$

The anode electrolytes could be circulated at a same flow rate for OER:

$$OER\ inlet\ flow = effluent\ inlet\ flow = 10212\ m^3/h$$

b) Analysis of capital costs

The stack cost could be evaluated as \$ 100/kW. Taking the consideration that the setup is going to be operated at 1 A/cm^2 and 3.89 V. Hence, the cost per area for the NH_3 flow cell is:

$$per\ area\ cost = \frac{\$\ 100}{kW} \times \frac{1\ A}{cm^2} \times 3.89 \times \frac{10000\ cm^2}{m^2} \times \frac{kW}{1000\ W} = \$\ 3890\ /m^2$$

As a result, the total cost for NH_3 flow system could be obtained:

$$total\ \cos t\ of\ flow\ system = \$5839\ m^2 \times 3890 \frac{\$}{m^2} = \$22.7\ million$$

From the DOE analysis, the balance of plant capital cost is 35% of the total cost, which can be calculated as followed:

$$BoP\ cost = \$22.7\ million\ \times 0.35/0.65 = \$12.2\ million$$

c) Analysis of operating costs

The electricity cost is able to be evaluated based on the power requirement and when taking the price of electricity as \$0.025 /kWh:

$$electricity\ cost = 227\ MW \times \frac{10^3\ kW}{MW} \times 24\ h \times \$0.025\ /kWh = \$136200\ /day$$

The maintenance cost is assumed as 2.0% of capital cost per year:

$$maintainence\ cost = \frac{\$22.7\ million\ /year \times 0.020}{350\ days/year} = \$1297\ /day$$

The nitrate concentration used in our experiments (2000 ppm) is not very high compared to some typical wastewater sources, such as agricultural runoff, industrial effluents, and municipal sewage, so pretreatment cost of nitrate substrate is neglected. we assume that the absorption method is used to separate ammonia. According to the literature, when activated carbon is used as an adsorbent, the regeneration efficiency is 80%, and the cost per kilogram of ammonia is about 0.07 $.

Because the original goal of NO_3^-RR is to reduce nitrate contamination, the cost of industrial effluent is neglected. The water solution at OER side is in circulating mode and only consume a relatively low amount, which is also neglected.

The yearly profit is given by the product income minus the sum of operation costs:

$$yearly\ profit$$

$$= (\frac{100000\ kg}{day} \times \$1.645\ /kg - \$136200\ /day - \$1297\ /day - 100000kg/day$$

$$= \$7.00\ million\ /year$$

d) Analysis of net present value (NPV)

Assuming an ideal situation for the stack to be maintained, the NH_3 stack is designed for a 5-year of working. The NPV is roughly estimated using the yearly profit value as cash flows per year, and the nominal interest rate is 5%. According to the NPV calculation equation:

$$NPV(5) = \sum_{n=1}^{5} \$7.00\ million \times (\frac{1}{1.05^n}) - \$22.7\ million - \$12.2\ million = \$ - 4.59\ million$$

$$NPV(10) = \sum_{n=1}^{10} \$7.00\ million \times \left(\frac{1}{1.05^n}\right) - \$22.7\ million - \$12.2\ million = \$19.15\ million$$

All the parameters and results were settled in Table S7 as followed:

Table S7. Parameters and results referred in the techno-economic analysis.

Name of parameter	Value
Per area cost	\$3890 /m^2
Total cost of flow system	\$22.7 million
BoP cost	\$12.2 million
Electricity cost	\$136200 /day
Maintenance cost	\$1279 /day

e) Several sensitivity analysis

The electricity cost could also be influenced by the current density during operation as shown in Fig. S47:

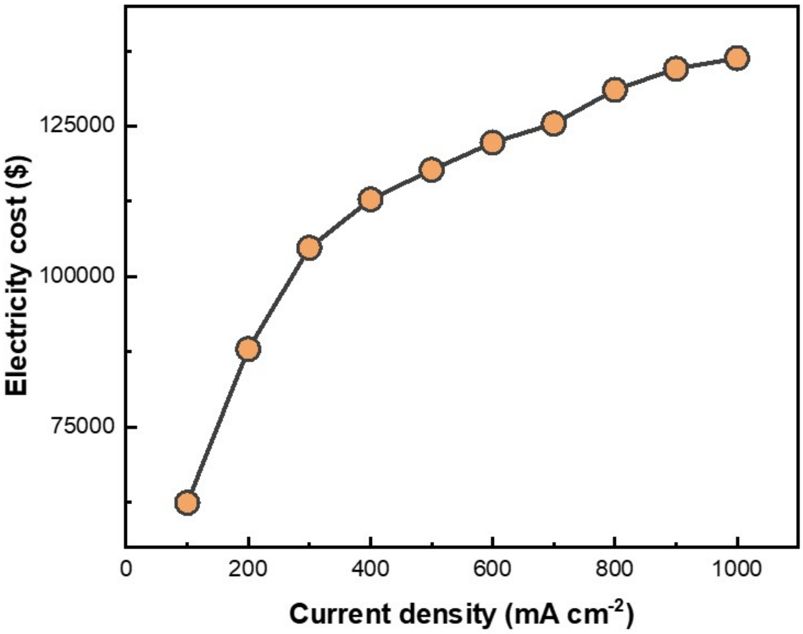

Fig. S47. The relationship between electricity cost and current density at operation.

On the other side, the price of electricity could directly influence the electricity and finally decide the yearly profit as shown in Fig. S48.

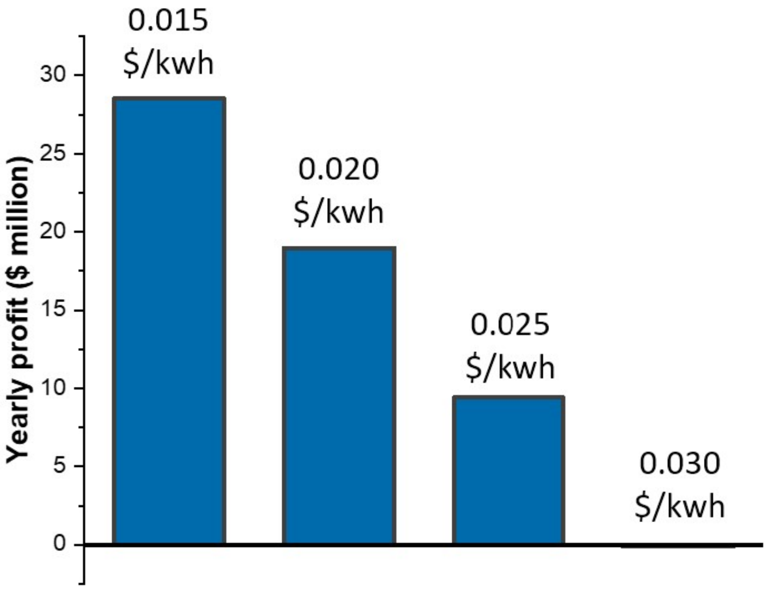

Fig. S48. The relationship between yearly profit and electricity cost.

As demonstrated in the sensitivity analysis, several factors can to a great extent influence the result of technological economy when taking the NH_3 electrosynthesis process as a practical project. Because the capital cost and electricity consumption can be decided by the operation current density and voltage, a lower current can bring more acceptable cost in the analysis. Nevertheless, more active area of the system is required if the same NH_3 production should be promised. As a result, to design better materials (membranes and catalysts) for achieving lower cell voltage is of significance. On the other hand, yearly profit could be obviously affected by the price of electricity. As we know that this price is highly fluctuant according to time and policies, it is going to be further decline in the future with the development of renewable energy harvesting and storage technologies and might lead to the profit lifting in the next few years. Last but not least, the NPV could be influenced a lot versus the life span of the bipolar membrane NH_3 flow system. This value only becomes positive when operating more than 5 years, which also indicated the importance of durability of the devices.

Reference

1. Z. Yan, L. Zhu, Y. C. Li, R. J. Wycisk, P. N. Pintauro, M. A. Hickner and T. E. Mallouk, *Energy & Environmental Science*, 2018, **11**, 2235-2245.
2. B. S. Kim, S. C. Park, D.-H. Kim, G. H. Moon, J. G. Oh, J. Jang, M.-S. Kang, K. B. Yoon and Y. S. Kang, *Small*, 2020, **16**, 2002641.
3. P. Wang, Y. Lin, Q. Xu, Z. Xu, L. Wan, Y. Xia and B. Wang, *ACS Applied Energy Materials*, 2021, **4**, 9022-9031.
4. L. C. Green, D. A. Wagner, J. Glogowski, P. L. Skipper, J. S. Wishnok and S. R. Tannenbaum, *Analytical Biochemistry*, 1982, **126**, 131-138.
5. G. W. Watt and J. D. Chrisp, *Analytical Chemistry*, 1952, **24**, 2006-2008.
6. H. Peng, Q. Li, M. Hu, L. Xiao, J. Lu and L. Zhuang, *Journal of Power Sources*, 2018, **390**, 165-167.
7. J. Wang, Y. Zhao, B. P. Setzler, S. Rojas-Carbonell, C. Ben Yehuda, A. Amel, M. Page, L. Wang, K. Hu, L. Shi, S. Gottesfeld, B. Xu and Y. Yan, *Nature Energy*, 2019, **4**, 392-398.
8. X. Liang, M. A. Shehzad, Y. Zhu, L. Wang, X. Ge, J. Zhang, Z. Yang, L. Wu, J. R. Varcoe and T. Xu, *Chemistry of Materials*, 2019, **31**, 7812-7820.
9. S. Li, C. Lian, G. Yue, J. Zhang, D. Qiu and F. Mo, *The Journal of Organic Chemistry*, 2022, **87**, 4291-4297.
10. B. Eswaraswamy, A. Suhag, P. Goel, P. Mandal and S. Chattopadhyay, *Separation and Purification Technology*, 2022, **295**, 121257.
11. B. Eswaraswamy, P. Goel, P. Mandal, A. Chandra and S. Chattopadhyay, *Polymers for Advanced Technologies*, 2022, **33**, 353-367.
12. M. A. Shehzad, A. Yasmin, X. Ge, Z. Ge, K. Zhang, X. Liang, J. Zhang, G. Li, X. Xiao, B. Jiang, L. Wu and T. Xu, *Nature Communications*, 2021, **12**, 9.
13. G. Li, M. A. Shehzad, Z. Ge, H. Wang, A. Yasmin, X. Yang, X. Ge, L. Wu and T. Xu, *Separation and Purification Technology*, 2021, **275**, 119167.

14. E. Al-Dhubhani, H. Swart, Z. Borneman, K. Nijmeijer, M. Tedesco, J. W. Post and M. Saakes, *ACS Applied Energy Materials*, 2021, **4**, 3724-3736.
15. Y. Chen, J. A. Wrubel, W. E. Klein, S. Kabir, W. A. Smith, K. C. Neyerlin and T. G. Deutsch, *ACS Applied Polymer Materials*, 2020, **2**, 4559-4569.
16. Z. Ge, M. A. Shehzad, L. Ge, Y. Zhu, H. Wang, G. Li, J. Zhang, X. Ge, L. Wu and T. Xu, *ACS Applied Energy Materials*, 2020, **3**, 5765-5773.
17. A. Hohenadel, D. Powers, R. Wycisk, M. Adamski, P. Pintauro and S. Holdcroft, *ACS Applied Energy Materials*, 2019, **2**, 6817-6824.
18. M. Manohar, A. K. Das and V. K. Shahi, *Industrial & Engineering Chemistry Research*, 2018, **57**, 1129-1136.
19. M. B. McDonald, M. S. Freund and P. T. Hammond, *ChemSusChem*, 2017, **10**, 4599-4609.
20. C. Shen, R. Wycisk and P. N. Pintauro, *Energy & Environmental Science*, 2017, **10**, 1435-1442.
21. J. Pan, L. Hou, Q. Wang, Y. He, L. Wu, A. N. Mondal and T. Xu, *Materials Chemistry and Physics*, 2017, **186**, 484-491.
22. M. Manohar, G. Shukla, R. P. Pandey and V. K. Shahi, *Journal of Industrial and Engineering Chemistry*, 2017, **47**, 141-149.
23. Q. Wang, B. Wu, C. Jiang, Y. Wang and T. Xu, *Journal of Membrane Science*, 2017, **524**, 370-376.
24. X. Liu, X. Jian, H. Yang, X. Song and Z. Liang, *New Journal of Chemistry*, 2016, **40**, 3075-3079.
25. M. B. McDonald, J. P. Bruce, K. McEleney and M. S. Freund, *ChemSusChem*, 2015, **8**, 2645-2654.
26. X. Liu, H. Yang, H. Dai, X. Mao and Z. Liang, *Green Chemistry*, 2015, **17**, 199-203.
27. S. Abdu, K. Sricharoen, J. E. Wong, E. S. Muljadi, T. Melin and M. Wessling, *ACS Applied Materials & Interfaces*, 2013, **5**, 10445-10455.
28. T.-j. Zhou, Y.-y. Hu, R.-y. Chen, X. Zheng, X. Chen, Z. Chen and J.-q. Zhong, *Applied Surface Science*, 2012, **258**, 4023-4027.
29. A. M. Rajesh, T. Chakrabarty, S. Prakash and V. K. Shahi, *Electrochimica Acta*, 2012, **66**, 325-331.

30. A. M. Rajesh, M. Kumar and V. K. Shahi, *Journal of Membrane Science*, 2011, **372**, 249-257.

31. R.-Y. Chen, Z. Chen, X. Zheng, X. Chen and S.-Y. Wu, *Journal of Membrane Science*, 2010, **355**, 1-6.

32. F.-Y. Chen, Z.-Y. Wu, S. Gupta, D. J. Rivera, S. V. Lambeets, S. Pecaut, J. Y. T. Kim, P. Zhu, Y. Z. Finfrock, D. M. Meira, G. King, G. Gao, W. Xu, D. A. Cullen, H. Zhou, Y. Han, D. E. Perea, C. L. Muhich and H. Wang, *Nature Nanotechnology*, 2022, DOI: 10.1038/s41565-022-01121-4.

33. X. Fan, L. Xie, J. Liang, Y. Ren, L. Zhang, L. Yue, T. Li, Y. Luo, N. Li, B. Tang, Y. Liu, S. Gao, A. A. Alshehri, Q. Liu, Q. Kong and X. Sun, *Nano Research*, 2022, **15**, 3050-3055.

34. Q. Chen, J. Liang, L. Yue, Y. Luo, Q. Liu, N. Li, A. A. Alshehri, T. Li, H. Guo and X. Sun, *Chemical Communications*, 2022, **58**, 5901-5904.

35. J. Crawford, H. Yin, A. Du and A. P. O'Mullane, *Angewandte Chemie International Edition*, 2022, **61**, e202201604.

36. T. H. Jeon, Z.-Y. Wu, F.-Y. Chen, W. Choi, P. J. J. Alvarez and H. Wang, *The Journal of Physical Chemistry C*, 2022, **126**, 6982-6989.

37. Y. Zhao, Y. Liu, Z. Zhang, Z. Mo, C. Wang and S. Gao, *Nano Energy*, 2022, **97**, 107124.

38. J. Cai, S. Qin, M. A. Akram, X. Hou, P. Jin, F. Wang, B. Zhu, X. Li and L. Feng, *Journal of Materials Chemistry A*, 2022, **10**, 12669-12678.

39. W. Fu, Z. Hu, Y. Zheng, P. Su, Q. Zhang, Y. Jiao and M. Zhou, *Chemical Engineering Journal*, 2022, **433**, 133680.

40. Z.-Y. Wu, M. Karamad, X. Yong, Q. Huang, D. A. Cullen, P. Zhu, C. Xia, Q. Xiao, M. Shakouri, F.-Y. Chen, J. Y. Kim, Y. Xia, K. Heck, Y. Hu, M. S. Wong, Q. Li, I. Gates, S. Siahrostami and H. Wang, *Nature Communications*, 2021, **12**, 2870.

41. J. Lim, C.-Y. Liu, J. Park, Y.-H. Liu, T. P. Senftle, S. W. Lee and M. C. Hatzell, *ACS Catalysis*, 2021, **11**, 7568-7577.

42. P. Li, Z. Jin, Z. Fang and G. Yu, *Energy & Environmental Science*, 2021, **14**, 3522-3531.

43. Y. Li, S. Xiao, X. Li, C. Chang, M. Xie, J. Xu and Z. Yang, *Materials Today Physics*, 2021, **19**, 100431.

44. S. Bunea, K. Clemens and A. Urakawa, *ChemSusChem*, 2022, **15**, e202102180.

45. P. Huang, T. Fan, X. Ma, J. Zhang, Y. Zhang, Z. Chen and X. Yi, *ChemSusChem*, 2022, **15**, e202102049.

46. Z. Liu, C. Wang, C. Chen, C. Li and C. Guo, *Electrochemistry Communications*, 2021, **131**, 107121.

47. Q. Yao, J. Chen, S. Xiao, Y. Zhang and X. Zhou, *ACS Applied Materials & Interfaces*, 2021, **13**, 30458-30467.

48. K. Nagita, Y. Yuhara, K. Fujii, Y. Katayama and M. Nakayama, *ACS Applied Materials & Interfaces*, 2021, **13**, 28098-28107.

49. G.-F. Chen, Y. Yuan, H. Jiang, S.-Y. Ren, L.-X. Ding, L. Ma, T. Wu, J. Lu and H. Wang, *Nature Energy*, 2020, **5**, 605-613.

50. Y. Wang, W. Zhou, R. Jia, Y. Yu and B. Zhang, *Angewandte Chemie International Edition*, 2020, **59**, 5350-5354.

51. R. Jia, Y. Wang, C. Wang, Y. Ling, Y. Yu and B. Zhang, *ACS Catalysis*, 2020, **10**, 3533-3540.

52. J. M. McEnaney, S. J. Blair, A. C. Nielander, J. A. Schwalbe, D. M. Koshy, M. Cargnello and T. F. Jaramillo, *ACS Sustainable Chemistry & Engineering*, 2020, **8**, 2672-2681.

53. J. Li, G. Zhan, J. Yang, F. Quan, C. Mao, Y. Liu, B. Wang, F. Lei, L. Li, A. W. M. Chan, L. Xu, Y. Shi, Y. Du, W. Hao, P. K. Wong, J. Wang, S.-X. Dou, L. Zhang and J. C. Yu, *Journal of the American Chemical Society*, 2020, **142**, 7036-7046.

54. Y. Wang, A. Xu, Z. Wang, L. Huang, J. Li, F. Li, J. Wicks, M. Luo, D.-H. Nam, C.-S. Tan, Y. Ding, J. Wu, Y. Lum, C.-T. Dinh, D. Sinton, G. Zheng and E. H. Sargent, *Journal of the American Chemical Society*, 2020, **142**, 5702-5708.

55. T. Sokalski and A. Lewenstam, *Electrochemistry Communications*, 2001, **3**, 107-112.

56. T. Sokalski, P. Lingenfelter and A. Lewenstam, *The Journal of Physical Chemistry B*, 2003, **107**, 2443-2452.

57. L. Onsager, *The Journal of Chemical Physics*, 1934, **2**, 599-615.

58. M. E. Tuckerman, D. Marx and M. Parrinello, *Nature*, 2002, **417**, 925-929.

59. D. V. Golubenko and A. B. Yaroslavtsev, *Journal of Membrane Science*, 2021, **635**, 119466.

60. M. A. Blommaert, D. A. Vermaas, B. Izelaar, B. in ’t Veen and W. A. Smith, *Journal of Materials Chemistry A*, 2019, **7**, 19060-19069.